UC Berkeley
UC Berkeley Electronic Theses and Dissertations

Title
Studies of Frustration and Disorder via Electrical Manipulations

Permalink
https://escholarship.org/uc/item/9092p4wt

Author
Haley, Shannon Claire

Publication Date
2023

Peer reviewed|Thesis/dissertation

Studies of Frustration and Disorder via Electrical Manipulations

by

Shannon C. Haley

A dissertation submitted in partial satisfaction of the

requirements for the degree of

Doctor of Philosophy

in

Physics

in the

Graduate Division

of the

University of California, Berkeley

Committee in charge:

Professor James Analytis, Chair
Professor Joel Moore
Professor Sayeef Salahuddin

Fall 2022

Studies of Frustration and Disorder via Electrical Manipulations

Abstract

Studies of Frustration and Disorder via Electrical Manipulations

by

Shannon C. Haley

Doctor of Philosophy in Physics

University of California, Berkeley

Professor James Analytis, Chair

This dissertation primarily explores the nature and consequences of frustration and disorder in the intercalated transition metal dichalcogenide Fe_xNbS_2. This exploration is done mainly through the unconventional measurement of resistivity changes in response to brief electrical stimuli. These measurements uncover surprising details of the system, which are otherwise very difficult to observe, and they are an end in and of themselves, establishing a promising path towards low-energy antiferromagnetic spintronics. This work also includes measurements in high magnetic fields which elucidate the phase diagram and microscopic interactions in this system, more conventional measurements which supplement our understanding, and studies of close relatives of Fe_xNbS_2 with an eye towards their potential applications and the insights they can allow into their sister compounds.

Dedicated to my family, who taught me the joy of curiosity, the satisfaction of hard work, and the importance of keeping your feet solidly planted while your eyes marvel at the sky.

Contents

List of Figures

List of Tables

Acknowledgments

The past five and a half years have been very long, and they have been very short. The people I've met have curiously been mostly quite tall, although some have been very short as well. To everyone, thank you.

Thank you especially to my advisor, **James**. Thank you for your mentorship, for encouraging and challenging me to grow, for keeping me focused on the big picture, and for being an excellent guide in the exotic and at-times-frightening land of novel quantum materials. Above all, though, thank you for your joyful approach to science and your dogged belief in people.

And thank you everyone I've gotten to know and work with in the Analytis Group. It is really a remarkable thing to get to work with so many great scientists who are also truly fantastic people. Thank you **Eran** for being my second mentor, and for always being open to talking shop. I remain amazed by the seemingly endless energy you have for experiments, and by the easy and good-natured demeanor you maintain while you must be completely exhausted. It was an absolute pleasure to get to work with and learn from you, especially when we broke a quartz rod in one of the magnets at Tallahassee and they had to use a crane to turn the whole thing upside down. Thank you **Vikram** for suggesting I check out your group when I told you that I wanted to pivot to hard condensed matter, and for your friendship and support all throughout grad school. Thank you **Nikola** for being the person I could ask stupid questions when I first joined the group (and frankly to this day), for somehow making it through however many months of quarantine together, and for consistently helping me through the times I didn't want to get through. And most importantly, thanks for teaching me the feasibility of mostly just eating raw vegetables.

Thank you **Valéria** for keeping me on my toes by being a frighteningly fast learner, for bringing your fresh and sharp perspective to science and non-science matters, and for being my dancing buddy. I look forward to seeing the amazing things that you will do. Thank you **Josue** for making so many long FIB sessions not just manageable but enjoyable, for reminding me of life's simple joys, and for ensuring that I can graduate with a clean conscience, knowing that the future of our lab's FIB-based experiments is in good hands. And thank you for showing me that I'm stronger than I thought, even if I never managed to deadlift 135lbs. Thank you **Koh** for being the little brother I always wanted, and for making sure that I didn't become too jaded before graduating, and **Jon** for almost laughing at my jokes. Thank you **Yuanqi** for being my (and everyone's) favorite supervillain, for taking care of so much in the lab, and for letting me in on your always nuanced and thoughtful thoughts.

Thank you **Sylvia, Robert, Ella, and Ian** for welcoming me into the group, and for being wonderful people to look up to as I learned the ropes. And thank you **Ryan, Luke, and Hossein** for likewise being great role models and fantastic people to work with as I have

been wrapping things up. Thank you **Caolan and Spencer** for teaching me how to grow crystals, and thank you **Gerardo and Qingyang** for asking questions that made me see things in a new light. And thank you **Susana and Meera**, for all of the long days at LBL, for tolerating the many iterations of our three-person journal club, and for the privilege of seeing you both grow as people and scientists.

Beyond our group, there are many collaborators who have made the works described in this dissertation possible, and who have taught me much while being lovely people to work with. Thank you **John Singleton**, for sharing your expertise and for putting so much into making our high field experiments successful. Thank you **Sophie Weber and Tessa Cookmeyer**, for your thoughtful contributions and calculations that made the experiments make sense, and for generally being very wonderful people. And thank you **Shan Wu**, for your neutron scattering measurements that really shone the ultimate light on the fascinating system we've been studying. Thank you as well for sharing your knowledge with me, and for being both an inspiring and a fun person to work with.

Some amount of these past years has been spent outside of the lab, and I owe a great debt of gratitude to the people who have made that time especially memorable and meaningful as well. Thank you to **my family** for your love, support, and many sanity checks. Thank you **Julia** and **Alex** for being a constant source of stability and for opening your home to me when I needed a place to stay. Thank you **Valerie** for all of the phone calls and long trips between Berkeley and San Jose. Thank you **Francisco** for a million podcast recommendations, and for reminding me to think deeply about the world and to laugh about it as well. Thank you **Olive** for the late night chats, the bad puns, the good puns, the swing dancing, and the board games. And thank you above all for being my friend, truly through thick and through thin.

Thank you **Greg, Aash, Eric, and Nathaniel**, for the many chaotic evenings we spent transporting refreshments and hosting socials as YFNBP (and only losing the key to the closet one time!). Thanks to the members of **Hyperfine**, with whom I spent many evenings forgetting my woes by chasing a circle through the sky. Thanks to the members of **Compass** and **Lindy on Sproul**, and to my **DnD** group. And thank you, in no particular order, to: **Tessa**, **Hannah**, **Hadar**, and **Ed**. **Caesar**, **Vincent**, and **Jackie**. **Donny** and **Kayla**. **Winnie** and **Nathaniel**.

This also would not have been possible without the guidance of my undergraduate advisor, **Alexandra Zidovska**. Thank you, Prof. Zidovska, for believing in me, for pushing me to be and do better than I thought I could, and for suggesting that I apply to graduate school. In Prof. Zidovska's lab, I got the chance to work with two truly remarkable then-graduate students – thank you **Christina** and **Fang** for guiding my early forays into science, and for serving as examples of bright, capable, and kind scientists. And thank you as well to the people I met in undergrad who have continued to be hugely important parts of

my life: **George**, my long-time pen-pal and constant confidant, and **Hillary**, my one-time mentee and now-very-much mentor-and-friend.

And finally, thank you **Jon Deasy**, for keeping our group running smoothly, always being so kind and thoughtful, and helping me through more than one moral quandary. Thank you **Carlos Bustamante**, for keeping the labs running smoothly and for being a bright spot on any day we cross paths. And thank you **Joelle Miles**, for keeping the department running smoothly, for being the first person to welcome me to Berkeley, for your unbelievable wealth of knowledge and patience, and for always responding to my panicked emails.

Over the course of my PhD studies, I have not only been challenged and given the chance to grow in ways familiar and new, I have felt accepted and supported to an extent that I didn't know to hope for. It is difficult not to be overwhelmed by how truly, remarkably lucky I have been. Thank you again, and see you nerds soon.

Chapter 1

Introduction and Background

"... j'avais été précédé dans cette voie, au XIIème siècle, par Pierre de Maricourt, auteur en 1269 du premier traité sérieux sur les aimants...

"... la liaison Université-Industrie dont on parle becaucoup aujourd'hui est en réalité très ancienne puisque la lettre de Pierre de Maricourt se préoccupait principalement des applications du magnétisme aux boussoles et aux compas de marine, pour la navigation."

– Louis Néel

The interplay between frustration and disorder is something that is perhaps familiar to many. The aspiration of the present work is to explore these things in the context of a magnetic system. The system in question behaves strangely; it remembers things it should not remember, and knows things it should not know. It is exactly this unusual behavior that has allowed us to delve deeply into the underlying physics of this system from an altogether new perspective, and it is exactly this unusual behavior that has inspired us to do so. At the heart of this work is the interplay not just of phenomena and of different orders, but of fundamental and applied physics. They inspire, enable, and enrich each other at every juncture.

1.1 Magnetism

To start off, the system in question is magnetic. The kind of magnetism that is most prominent in the general consciousness is ferromagnetism – named for iron, its most common example. In a typical ferromagnet, localized unpaired electrons predominantly prefer to align their spins with those of their neighbors. It is also possible for electrons to prefer to anti-align with their neighbors, which is known as antiferromagnetism. Either preference can be represented as an energetic term in the Hamiltonian proportional to the dot products of the spins:

$$H = -\sum_{ij} J_{ij} \vec{S}_i \cdot \vec{S}_j \tag{1.1}$$

where J_{ij}, the exchange constant, is the strength of the interaction and its sign determines whether the interaction is ferromagnetic or antiferromagnetic.

In order to understand the origin of this interaction and the factors determining its sign and strength, consider the joint wavefunction of two electrons. It must be antisymmetric under exchange of those electrons, because they are fermions. The wavefunction can be written as follows:

$$\Psi = \frac{1}{\sqrt{2}}(\psi_a(\vec{x}_1)\psi_b(\vec{x}_2) \pm \psi_a(\vec{x}_2)\psi_b(\vec{x}_1))\chi \tag{1.2}$$

where $\vec{x}_1$ and $\vec{x}_2$ are the positions of the two electrons, ψ_a and ψ_b are their spatial wavefunctions, and χ is the spin component of the joint wavefunction. Note that when the two terms are added, the spatial wavefunction is symmetric under exchange, and when they are subtracted it is antisymmetric.

If the antisymmetric spatial case is more energetically favorable, the spin component must be symmetric so that the wavefunction as a whole will be antisymmetric. The spins will then prefer to align with one another. This is often the case when the electrons are on the same atom due to the Coulomb interaction, leading to Hund's rule which maximizes spin on a single atom. Likewise, if a spatially symmetric state is favorable then an anti-aligned spin configuration will be preferred. The strength of this preference will in either case be determined by the difference between the energies of the spatial states.

Direct exchange refers to the situation where neighboring atoms have unpaired electrons which predominantly interact via direct overlap of their orbitals. A state with anti-aligned spins, known as an antiferromagnetic state, tends to be preferred in the case of direct exchange because a spatially symmetric joint wavefunction (bonding orbital) has lower kinetic energy than a spatially antisymmetric joint wavefunction (antibonding orbital).

Superexchange refers to the situation where unpaired electrons on two atoms are coupled not via direct overlap of their orbitals, but via mutual overlap of another atom's orbitals. This sort of interaction can in principle lead to ferromagnetism or to antiferromagnetism, although in practice the latter is more common. For example, consider two atoms with a single unpaired electron each, mutually overlapping with a filled orbital on a third atom. The kinetic energy of the system is minimized when the electrons are delocalized over the 3-atom complex, and this is allowed only when they have opposite spins to one another.

Conduction electrons can also serve as an intermediary for magnetic exchange between localized electrons, referred to as the Ruderman-Kittel-Kasuya-Yosida interaction or RKKY. First, consider the response of an electron gas to a nonuniform magnetic field which can be broken into components of the form

$$H(\vec{r}) = H_{\vec{q}}\cos(\vec{q}\cdot\vec{r}) \tag{1.3}$$

By perturbing the plane waves that comprise the electron gas, one can derive the resulting magnetization from a single perturbed wavefunction with wavevector k:

$$M(\vec{r}) \propto H_q \cos(\vec{q}\cdot\vec{r})\left(\frac{1}{(\vec{k}+\vec{q})^2 - k^2} + \frac{1}{(\vec{k}-\vec{q})^2 - k^2}\right) \tag{1.4}$$

Summing over k weighted by the density of states $g(\vec{k})$, the full magnetization is:

$$M(\vec{r}) \propto k_F H_q \cos(\vec{q} \cdot \vec{r}) \left(1 + \frac{4k_F^2 - q^2}{4k_F q} \log|\frac{q + 2k_F}{q - 2k_F}| \right) \tag{1.5}$$

where k_F is the Fermi wave-vector. The wave-vector dependent magnetic susceptibility, then, is:

$$\chi_q \propto k_F \left(1 + \frac{4k_F^2 - q^2}{4k_F q} \log|\frac{q + 2k_F}{q - 2k_F}| \right) \tag{1.6}$$

A local magnetic moment can be considered a point-like perturbation to the magnetic field:

$$\vec{H}(\vec{r}) = \delta(\vec{r})\vec{H} \tag{1.7}$$

and the susceptibility will vary over space as a result in this way:

$$\chi(\vec{r}) = \frac{1}{(2\pi)^3} \int d^3\vec{q} \chi_q e^{i\vec{q}\cdot\vec{r}} \tag{1.8}$$

which finally gives

$$\chi(\vec{r}) \propto k_F^3 \frac{-2k_F r \cos(2k_F r) + \sin(2k_F r)}{(2k_F r)^4} \tag{1.9}$$

This is the susceptibility when considering a spherical Fermi surface, and treating the local moment as a point-like perturbation to the magnetic field. In the case of long-distance interactions (much larger than k_F^{-1}) and with these same assumptions, the exchange constant has the following relationship to the distance r between atoms:

$$J_{RKKY}(\vec{r}) \propto \frac{\cos(2k_F r)}{r^3} \tag{1.10}$$

These calculations can be found in more detail in Reference [5]. Note that the exchange constant calculated in this way is oscillatory and decays as a function of distance. RKKY can be ferromagnetic or antiferromagnetic, and is spatially dependent. RKKY and superexchange are thought to be the primary sources of magnetism for the materials discussed in this thesis.

In terms of experimental signatures, the most straightforward measurement of ferromagnetism and antiferromagnetism is magnetization or magnetic susceptibility. See Figure 1.1. Under a small applied magnetic field (generally on the order of $100 - 1000$Oe), a ferromagnet has dramatically increasing magnetization with decreasing temperature below its transition temperature, and an antiferromagnet has decreasing magnetization with decreasing temperature below its transition temperature. Above the transition temperature, denoted T_N or the Néel temperature for an antiferromagnet and T_C or the Curie temperature for a ferromagnet, paramagnetic behavior proportional to $1/(T - T_{C/N})$ should be observed.
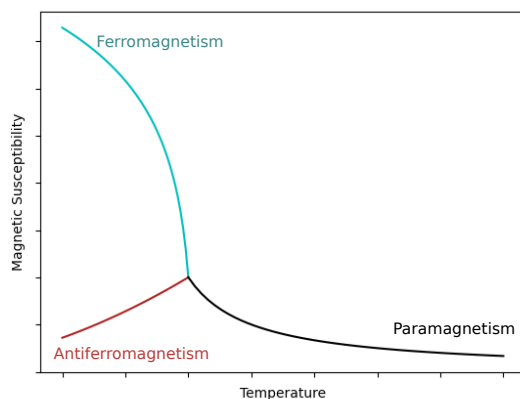
Figure 1.1: Schematic of magnetic susceptibility as a function of temperature in the cases of antiferromagnetic and ferromagnetic interactions.
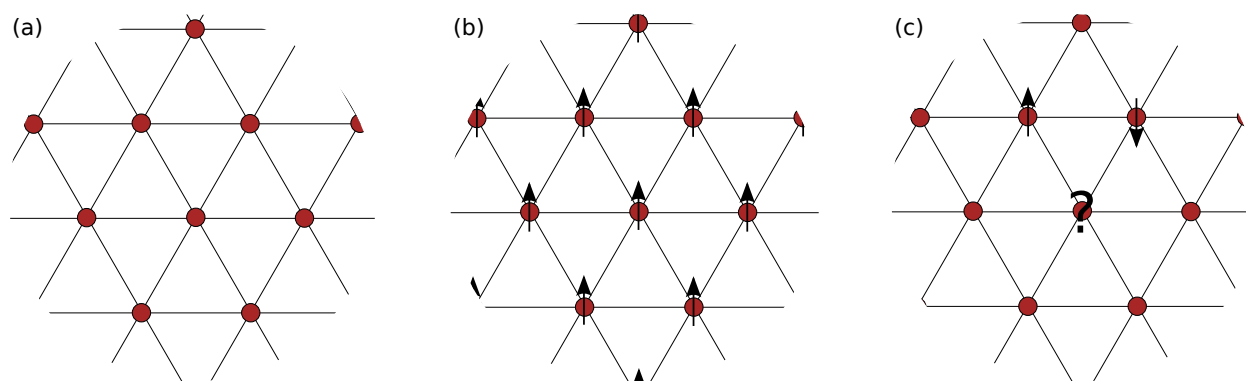
Figure 1.2: (a) Schematic of triangular lattice of ions. (b) Triangular lattice of ions, ferromagnetically ordered. (c) Illustration of geometric frustration in a triangular lattice of ions with antiferromagnetic exchange.

1.2 Frustrated Magnetism

While the consequences of ferromagnetism are easier to observe and to incorporate into applications, antiferromagnets are plentiful in nature and – as discussed above – in fact more commonly arise from some of the mechanisms mediating exchange. Abundant also is the diversity of states that follow from antiferromagnetic exchange interactions, especially in frustrated systems.

Take, for example, a set of magnetic ions on a triangular lattice, as illustrated in Figure 1.2

(a). While ferromagnetic exchange can be satisfied in a straightforward way, with mutual alignment of the spins (Figure 1.2 (b)), antiferromagnetic exchange cannot be fully satisfied. See Figure 1.2 (c) – when two neighboring spins are anti-aligned, there is no orientation that their mutual neighbors can take which allows them to benefit energetically from interactions with both anti-aligned spins. This is an example of what is known as geometric frustration. Treated simply, a triangular-lattice antiferromagnet is frustrated to the point that it should never order; with infinite degenerate lowest-energy states, the system should not choose a particular state even down to zero temperature. This is contrary to what is generally observed, however. In nature, triangular-lattice antiferromagnets order all the time, and the search for a system with magnetic exchange interactions that truly doesn't order down to low temperature is an active area of study.

So why do these systems order, when their Hamiltonian suggests that they should not? Some small alterations can be made to the Hamiltonian to make it more closely resemble common physical systems. For example, the lattice can be distorted, manifesting in an exchange constant that varies depending on the bond direction. This modification leads to a reduction in the degeneracy of the ground state. Ordering can be understood without changing the Hamiltonian at all, however, by expanding the treatment of the problem to consider thermal or quantum fluctuations (or both). These additional considerations lead to a choice of ground state based on their excitation spectra. In other words, the states are distinguished and order is attained because the shape of the energy landscape surrounding the accidentally degenerate ground states differ.

While frustrated magnets do order, the state that is chosen is often sensitively dependent on the parameters of the system, and in principle there are still many degenerate or nearly-degenerate states. This scenario is particular true for Fe_xNbS_2, the system that will be the basis of this thesis.

1.3   Magnetism and disorder

Moving away from an ideal system can – and in this work, does – mean the introduction of disorder. A spin glass is a disordered magnet, in which the exchange constants take on random values. Assuming these random values follow a Gaussian distribution allows a calculation of the free energy, which yields a phase with zero net magnetization that is trapped, upon cooling, in a subset of its possible lowest-energy states. This inability of the spin glass to visit all of its other degenerate equilibrium states is known as non-ergodicity. Consequences of disorder will be discussed more in Chapter 3, including the coexistence of a spin glass with antiferromagnetic order and some experimental signatures of spin glasses.

1.4   Spintronics

The dynamics of spins under an applied stimulus is an area of great practical interest, with applications including the development or further development of magnetic random access memory, frequency-tunable microwave sources, detectors, short-range communications within and between chips, and racetrack memory [6]. There are several ways to approach these problems, and several approximations that can make them more tractable. Domain wall motion can often be usefully treated by considering only uniform translations and rotations [6]. When considering bulk magnetization dynamics, it is often productive to describe the system in terms of spin waves. Alternatively, one can sometimes treat the system as though its magnetization does not vary spatially, i.e., under the macrospin approximation; this is a useful toy model, but it has significant limitations when considering real systems [6]. More exact are micromagnetic models, which approximate magnetic systems as continuous, with relevant lengthscales longer than interatomic distances.

Spin Orbit Torque

The precession around and gradual alignment with an effective magnetic field is described by the Landau-Lifshitz-Gilbert equation:

$$\frac{d\vec{M}}{dt} = -\gamma_0 \vec{M} \times \vec{H}_{\text{eff}} + \frac{\alpha}{M_s}\vec{M} \times \frac{d\vec{M}}{dt} \tag{1.11}$$

where γ_0 is the gyromagnetic ratio, and α is the damping parameter [6]. The first term is responsible for precession and the second for damping.

In many spintronic systems, torque is exerted on local moments at an interface where spin current is injected, or an interface with a material that has a spin accumulation on its surface [7]. In the system discussed in this dissertation, the relevant torque arises from a current-induced spin polarization of the conduction electrons, which exerts a spin orbit torque on local magnetic moments [7]. This spin polarization arises from the inverse spin-galvanic effect, and is dependent on the crystal symmetry in ways that will be discussed in more detail in Section 4.2. The effects on the local moments are derived in Reference [7] by calculating the spin polarization from a given applied electric field (the response tensor χ_a) and considering it in conjunction with the Hamiltonian of an example square lattice antiferromagnet (AFM):

$$H = \sum_{\langle ij \rangle} J_{dd}\hat{M}_i \cdot \hat{M}_j + H^{tb} + \sum_i J_{sd}\hat{S}_i \cdot \hat{M}_i + H_R \tag{1.12}$$

where $\hat{S}_i$ is the direction of the conduction electron spin polarization at lattice site i, $\hat{M}_i$ and $\hat{M}_j$ are the magnetic moment directions on lattice sites i and j, the subscripts of J indicate the orbitals of the electrons whose exchange J describes (with J_{dd} describing the exchange between d-orbital electrons and J_{sd} between d-orbital electrons and conduction s electrons),

H_{tb} describes nearest-neighbor hoppings, and H_R the Rashba spin-orbit coupling [7]. The torque on sublattice a is:

$$\vec{T}_a = \vec{M}_a \times \vec{B}_a \tag{1.13}$$

where $\vec{B}_a$, the effective field from the spin-polarized conduction electrons acting on sublattice a, is:

$$\vec{B}_a = -J_{sd}\frac{\delta\vec{S}_a}{M_a} = -\frac{J_{sd}}{M_a}\chi_a\vec{E} \tag{1.14}$$

and $\delta\vec{S}_a$ is the spin polarization induced by the applied current. The response tensor χ_a contains components that are even in magnetization and components that are odd in magnetization. Note that in cases where there are two collinear AFM sublattices of opposite magnetization, the even terms are shared between sublattices, while the odd terms are equal in magnitude but opposite in sign between sublattices. Reference [7] details a very thorough treatment of this problem, which outlines specific results for different symmetry groups and includes extensive numerical calculations for specific band structures. Notably, for one system of experimental interest Mn_2Au, that work finds that there is a staggered spin polarization with the form $\hat{L} \times (\hat{z} \times \hat{E})$, where $\hat{L}$ is the direction of the Néel vector, the difference between the sublattice magnetizations. More broadly, it finds that there are possible current-induced spin densities proportional to $\hat{z} \times \hat{E}$ and to $\hat{L} \times (\hat{z} \times \hat{E})$, with the presence of these terms depending on the symmetry of the crystal and with magnitudes depending on the exchange coupling parameter and band broadening. The torque experienced as a result of the spin polarized current has the form:

$$\vec{T}_a \approx \vec{M}_a \times \delta\vec{S}_a + \vec{M}_a \times (\vec{M}_a \times \delta\vec{S}_a) \tag{1.15}$$

for the a sublattice. The first term, which leads to precession around the spin polarization direction, is called field-like, while the second term, which leads to alignment away from the spin polarization, is called antidamping-like [8]. This is the treatment that initially motivated the experiments described in Chapter 4, although our analysis of the system eventually broadened, as is discussed in that chapter and in Chapters 5 and 6.

Anisotropic magnetoresistance

Anisotropic magnetoresistance (AMR) in a ferromagnet is the occurrence of resistivity that depends on the angle between the current and magnetization of a material. More broadly, AMR is an even function of magnetization, and so depends only on the angle between the current and spin axis; this angle-dependence therefore exists in antiferromagnets as well [9]. It can be described by a combination of crystalline and non-crystalline components, which do and do not depend additionally on the angle of the magnetization with respect to the crystal axes, respectively [9]. The non-crystalline component is most relevant to our measurements, because they do not indicate a dependence on the crystal axes. While AMR has been observed in various magnetic systems for more than a hundred years, it is much more difficult

to model than it is to measure; in short, however, it follows from spin-orbit coupling causing the scattering of the conduction electrons off of local moments to be spin-dependent [9].

1.5 Intercalated Transition Metal Dichalcogenides

Transition metal dichalcogenides (TMDs) are a class of van der Waals layered materials, commonly studied for their quasi-2D properties. They can be semiconductors or metals, depending on their exact composition and stacking, and can host charge density waves as well as superconductivity. They are not generally magnetic. They can take on magnetic properties, however, via the inclusion of certain transition metal ions between their layers. This process is referred to as intercalation, and the resulting materials are referred to as intercalated TMDs. A very solid foundation of work has been conducted on niobium disulfide intercalated with manganese, iron, cobalt, and nickel [4, 10, 11]. The most commonly studied intercalant-to-niobium ratios are 1/3 and 1/4. This dissertation will primarily focus on materials with ratios close to 1/3, which are generally denoted in the form $M_{1/3}NbS_2$ rather than MNb_3S_6 because of the extensive body of work that exists on the parent compound NbS_2. This is reflected in Table 1.1, which lists the magnetic order types and transition temperatures reported in References [4, 10, 11]. More recent work on $Cr_{1/3}NbS_2$ has found it to be a chiral helimagnet, possessing a magnetic phase characterized by easy-plane ferromagnetism between spins in the same plane, and ferromagnetism with a small canting from the DM interaction between planes [12]. A magnetic system which is easy-plane has spins which prefer to point within a specific plane of the crystal– this is as opposed to an easy-axis system, whose spins prefer to point along a specific crystallographic axis. Notably, the magnetism in these compounds varies significantly with substitutions of similar elements, and with very little difference in the crystal or electronic structure. Due to this, to the relatively large distances between atoms, and to transport anomalies at the magnetic transitions indicative of coupling between the conduction electrons and local moments, it is thought that RKKY is one of the dominant mechanism mediating magnetism in intercalated NbS_2 [4]. Inconsistencies with RKKY alone, however – most notably, different kinds of magnetic order associated with intercalates with the same valence – suggest that superexchange also contributes to the magnetic exchange in this system [4].

1.6 Thesis overview

This dissertation discusses the study of Fe_xNbS_2, through resistance switching and more conventional measurements, and presents conclusions regarding the interplay of frustration, disorder, and strain based on those measurements. There is also a brief overview of the beginnings of similar studies conducted on related systems, as well as a discussion of promising future directions in this realm.

	Cr	Mn	Fe	Co	Ni
Order	$FM_\perp$	$FM_\perp$	$AFM_\parallel$	AFM	AFM
T (K)	115	40	45	25	90

Table 1.1: Proposed values for $M_{1/3}NbS_2$, with M = Mn, Fe, Co, Ni, of magnetic order type and transition temperature from Reference [4]. FM and AFM indicate ferromagnetism and antiferromagnetism, respectively. $\parallel$ and $\perp$ indicate a preference to align with the c axis or to lie in the ab plane, respectively.

- **Chapter 1** introduced and gave cursory backgrounds on magnetism, frustration, disorder, antiferromagnetic spintronics, and intercalated transition metal dichalcogenides. More detail on these concepts is given in relevant chapters where necessary.

- **Chapter 2** details the synthesis recipes for the primary materials discussed in later chapters. It also provides some considerations for growing this class of materials more generally, and discusses growths of promising related materials that have yet to be achieved.

- **Chapter 3** examines the relationship between the antiferromagnetic order and disorder-driven spin glass in Fe_xNbS_2, particularly in the context of exchange bias. This includes characterizations of samples with different amounts of iron content, measurements of memory effects, and magnetization measurements up to 35T.

- **Chapter 4** describes the switching response of Fe_xNbS_2 under varying conditions, including its dependence on disorder as determined by x.

- **Chapter 5** examines the microscopic interactions in Fe_xNbS_2, primarily via measurements in high magnetic field, motivated by peculiarities in the switching response described in Chapter 4. This chapter also ends with a brief description of the antiferromagnetic order determined by neutron scattering measurements.

- **Chapter 6** details the surprising finding of long-distance transmission of spin information during switching stimuli, as well as strain measurements and their implications regarding the switching behavior in Fe_xNbS_2.

- **Chapter 7** summarizes more recent findings in TaS_2 and Co_xNbS_2, two materials related to Fe_xNbS_2. This chapter details the switching response found in TaS_2, as well as preliminary findings in Co_xNbS_2 and their potential implications.

- **Chapter 8** discusses promising future directions in the study of intercalated TMDs and in the use of switching measurements as a probe of difficult-to-measure orders.

Chapter 2

Synthesis

"The beauty of crystals lies in the planeness of their faces."
– Alfred Edwin Howard Tutton

2.1   Introduction

While Fe_xNbS_2 has been found in nature (See Reference [13]) this is generally not the most straightforward way to obtain it for study. Rather, the samples of Fe_xNbS_2 that have been measured in the present work have all been grown in the lab, which has the additional benefit of permitting studies of the compound with varying amounts of iron content. The related compounds discussed in this dissertation are also generally easier to grow than to find. This chapter discusses the recipes that were used to grow the samples analyzed in later chapters, and includes some discussion as well of in-progress efforts to grow related novel materials.

2.2   Iron- and cobalt- intercalated niobium disulfide

Single crystals of iron-intercalated niobium disulfide were grown via chemical vapor transport (CVT). First, stoichiometric quantities of iron, niobium, and sulfur were combined to form a precursor for the CVT growth. The mixture was sealed in an alumina crucible placed inside a quartz tube on top of quartz wool (See the diagram on the left of Figure 2.1), and brought to 400 degrees Celsius for 24 hours, then held at 950 degrees Celsius for 5 days. The intermediate step at 400 degrees Celsius served to allow the sulfur to start to react with the other constituent elements before boiling, significantly decreasing the chances of the quartz tube breaking during the growth process. Packing the tube with quartz wool under the crucible was also found to decrease the rate of breakage, as was the inclusion of 200 Torr of argon. After cooling to room temperature, the mixture was ground with a mortar and pestle and put through the same thermal cycle again to improve homogeneity. A homogenous and loosely flowing black powder resulted from this step. Between 0.2g and 0.4g of the powder
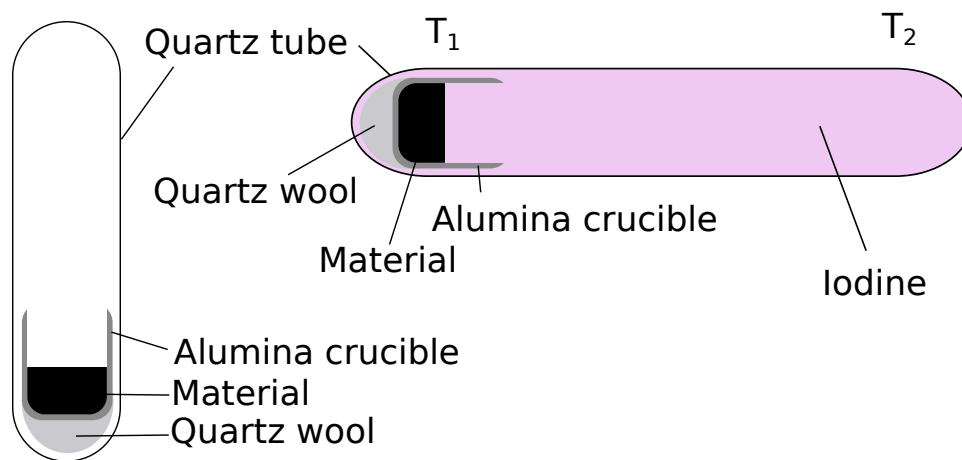
Figure 2.1: Left, assembly for single-temperature precursor synthesis. Right, assembly for dual-temperature chemical vapor transport. For Fe_xNbS_2, $T_1 = 950°C$ and $T_2 = 800°C$.

was finally sealed under vacuum in a 10" quartz tube with an inner diameter of 14mm, along with about 0.1g of iodine. The powder was again in an alumina crucible, as shown in the diagram on the right of Figure 2.1. Decreasing the amount of iodine slightly, to between 0.09g and 0.095g, was found to increase the size of the crystals yielded. The quartz tube was placed in an MTI 2-zone furnace set to 950 degrees Celsius on the side of the tube with the precursor and iodine, and 800 degrees Celsius on the opposite side. After allowing this reaction to run for 5 to 10 days, the crystals were harvested.

These crystals were found to not perfectly reflect the stoichiometric amount of iron included in the initial precursor. Generally, slightly less iron was found in the crystals than was measured out for the growth. There did not appear to be a strong preference for an Fe:Nb ratio of 1:3.

Single crystals of cobalt-intercalated niobium disulfide were grown intially following an identical recipe. However, this alone yielded crystals which displayed a ferromagnetic transition at $120K$, suggesting the inclusion of CoS_2 impurities. Annealing the crystals for three days at 400 degrees Celsius did away with these impurities, leaving pure Co_xNbS_2 as confirmed with magnetization measurements. This step was done on crystals which had been left in air to allow the evaporation of any excess iodine before being resealed in vacuum; when the annealing step was incorporated directly into the end of the CVT program instead, the ultimate stoichiometries as measured with EDX were found to change from their previously ideal values.

2.3   Tantalum disulfide

While the primary challenge of growing intercalated TMDs lies in attaining the optimal amount of intercalant (including, in some cases, any intercalant at all), the primary challenge of growing pristine TMDs lies in attaining the desired structural phase. Pristine TMDs can form 2H, 1T, and 3R phases, among others, which differ structurally by their stacking patterns and can yield dramatically different physical properties.

To grow 1T-TaS_2, which is in principle less stable at room temperature than 2H-TaS_2, first a stoichiometric mixture of tantalum and sulfur were reacted together at 850 degrees Celcius for 5 days, stopping at 400 degrees Celcius for 24 hours in order to allow sulfur to react sufficiently below its boiling point. Between 0.2g and 0.4g of the resulting precursor was sealed under vacuum in a 10" quartz tube with an inner diameter of 14mm, along with about 0.1g of iodine. The powder was again in an alumina crucible, as shown in the diagram on the right of Figure 2.1. The end of the tube containing the precursor powder was brought to 850 degrees Celcius, and the other end to 750 degrees Celcius for one week. The tube was then pulled from the furnace while still at those high temperatures, and immediately plunged into ice water. Previous attempts to quench the growth instead in liquid nitrogen curiously resulted in mixed structural phases, while ice water resulted in a homogenous 1T structure.

2.4   Doubly-intercalated niobium disulfide

In order to explore disorder in Fe_xNbS_2 along a different axis – through the inclusion of a different magnetic ion, rather than through deficiencies or excesses of iron alone, some effort was put into growing NbS_2 jointly intercalated with iron and either cobalt or chromium. Attempts to double-intercalate niobium disulfide with both cobalt and iron yielded an overrepresentation of iron, compared to the ratio included in the initial precursor, and an underrepresentation of cobalt, compared to the same. Similarly, attempts to double-intercalate with chromium and iron found that iron intercalated much more easily than chromium, resulting in an overrepresentation of iron and an underrepresentation of chromium, despite the similarities in their individual growth recipes.

2.5   Intercalated tungsten diselenide

Transition metal-intercalated tungsten diselenide has been predicted, based on DFT calculations, to have room-temperature magnetic properties while being structurally very similar to iron-intercalated niobium disulfide [14]. For this reason, some effort was put into growing these materials.

Attempts to intercalate tungsten diselenide were ultimately unsuccessful; via flux growth and chemical vapor transport, with a variety of temperature profiles and number of pelletization steps, only the pristine TMD was yielded. Attempts to chemically intercalate the pristine

TMD as-grown were also unfruitful. Intercalation in this TMD seems to be energetically unfavorable, based on our observations.

Chapter 3

Exchange Bias

"Sure, you can quote me saying whatever you want."

– Nikola Maksimovic

Materials in this chapter were previously published in

- Eran Maniv, Ryan A. Murphy, Shannon C. Haley, et al., *Exchange bias due to coupling between coexisting antiferromagnetic and spin-glass orders*, Nature Physics **17**, 525-530 (2021).

3.1 Introduction

The complex interactions at play in Fe_xNbS_2 lend themselves to more than one potential application. Information storage via changes between resistance states is the application that the majority of this thesis centers around, but equally important is the presence of exchange bias. The focus of this chapter is an in-depth discussion of that phenomenon and its surprising characteristics in Fe_xNbS_2.

The study of exchange bias falls in one of the most active areas of research at the boundary of physics and engineering, the exploration of technologies that leverage correlated properties of quantum materials. It is a critical component to a variety of devices such as spin-valves, used extensively in high density magnetic storage, [15] and has potentially more exotic applications, such as voltage-mediated magnetic switching for logic devices. [16] Exchange bias manifests itself as a shift in the hysteresis loop of a magnetic system when cooled under an applied external field, [17] and is observed in a diverse array of systems. Despite decades of study of the prototypical exchange bias system, thin film ferromagnetic/antiferromagnetic (FM/AFM) heterostructures, a complete understanding of the mechanism behind exchange bias is lacking. Recent work has revealed that pinned uncompensated moments generated by defects at the FM/AFM interface play a dominant role in engendering exchange bias, as well as in determining its magnitude. [18–20] The microscopic nature of the pinned uncompensated moment interface, how it is pinned by the AFM order parameter, and the mechanism

by which this coupling drives exchange bias remains an outstanding challenge. Importantly, this interface may host its own "hidden" glassy order parameter, driven by spin frustration from disorder at the FM/AFM interface itself. Indeed, spin-glasses (SGs) alone may display exchange bias, and this in concert with studies on FM/SG interfaces have led to hypotheses suggesting that glassy dynamics are intertwined with exchange bias. [21–25]

Spin glasses (SG) are a phase of matter occurring in many strongly correlated systems, but differ from ordered ferro- or antiferromagnets in that their ground state is metastable, being one of many nearly degenerate states. [26, 27] Central to these systems is frustration, which emerges as a result of site disorder [28,29] or local competition between exchange interactions. [30] The frustration protects the ergodicity of the system until the SG transition is reached, at which point a metastable state is settled upon. Understanding the dynamic processes by which the glass traverses through this energetic landscape remains a major theoretical question in the statistical mechanics of solids. Theoretical challenges notwithstanding, the frozen state of the SG depends on its history, in particular the applied field in which it was cooled. This is the origin of its exchange bias: the magnetism of the frozen state is biased by the correlations of the SG. Typically this is very small, of the order of 0.01 T.

In this work, we leverage the highly field-responsive nature of the SG order parameter as a source of pinned uncompensated moment, and embed this within an anisotropic antiferromagnet. By isolating these phases in the absence of a nearby ferromagnet, we are explicitly able to study the exchange coupling between the AFM order parameter (defined as the stability of the sublattice magnetization) and the SG order parameter (defined as the breaking of ergodicity of fluctuating, disordered spins. [31]) Using the system Fe_xNbS_2 as an example, we show that when the uncompensated moments form a SG, there appear giant lateral shifts in the hysteresis loops. We find that the AFM order parameter biases the response of the SG, but only when both become long-time correlated. The origin of the exchange bias therefore lies in the convolution of two energy landscapes: the highly-degenerate landscape of the SG, biased by the sublattice phase space of the AFM. Further, our intercalation series allows us to tune the relative stability of both SG and AFM order parameters by changing the composition x, outlining novel design principles towards the development of new giant exchange bias phases.

Fe_xNbS_2 consists of triangular lattices of iron embedded between $2H\text{-}NbS_2$ layers. Single crystals were synthesized using conventional vapor transport techniques while varying concentrations of iron (see Appendix I for characterization of homogeneity and stoichiometry). This material manifests AFM hexagonal ordering [1,32,33] with the moment predominantly oriented along the c-axis. For intercalation values less than $x = \frac{1}{3}$, SG-like behavior has been observed in magnetization and heat capacity measurements. [34–36] Magnetization versus temperature measurements performed along the c-axis on Fe_xNbS_2 for under- ($x = 0.30$) and over- ($x = 0.35$) intercalated values are shown in Figure 3.1a,c. For $x \approx \frac{1}{3}$, corresponding to the fully packed $Fe_{1/3}NbS_2$ structure, we observe a sharp AFM transition with a Néel temperature of approximately 42 K (see Appendix I) as has been previously reported. [1,10,35,37,38] Above or below $x = \frac{1}{3}$, field cooled (FC) and zero field cooled (ZFC) curves begin to separate, indicating the presence of a frozen moment. The magnetization is

observed to relax with time on removal of the applied field for such compositions, characteristic of SG behavior (Figure 3.1b,d). [27] The temperature onset of long relaxation times arises from the formation of an uncompensated moment, observed when FC and ZFC curves separate significantly. This temperature is roughly where the SG freezes on the time scale of the measurement, and the ergodicity of the system is broken; the spin configuration of the uncompensated moment is long-time correlated. Further experiments corroborating the glass state are detailed in this chapter's appendix.

The disorder opens up a hysteresis loop whose center strongly depends on the cooling field. In Figure 3.2a,c, we illustrate the low temperature hysteresis loop for samples cooled in 7 T, and then field cycled across ±7 T ten times. This 'training' of the hysteresis loop is consistent with exchange bias, and shows that the loop center becomes pinned at large fields; approximately 3 T for $x = 0.30$, and 0.7 T for $x = 0.35$. [27, 39] In Figure 3.2b,d, we show enlargement of zero field cooled hysteresis loops, but with two different protocols for the field sweeps. For sweeps starting negative, $0 \to -7 \to +7 \to -7$, the loop center shifts to positive field; for sweeps starting positive, $0 \to +7 \to -7 \to +7$, the loop center moves to negative field. This spontaneous bias points to a history-dependent coupling scheme between the AFM and SG phases which is significantly more sensitive than in typical exchange bias systems.

Figure 3.3a,c show the temperature dependent evolution of H_{EB} (defined as the average of the zero magnetization-intercepts) and H_C (defined as the half width of the hysteresis loop at the average of the zero field-intercepts) which presents a non-trivial dependence. While the onset of H_C occurs at around the SG freezing temperature as expected, the bias H_{EB} onsets at a significantly lower temperature. The reason for this can be gleaned from measurements of nuclear magnetic resonance (NMR) spectra shown in Figure 3.4. The iron exchange field is studied via its effect on the ^{93}Nb lattice (with nuclear spin I = 9/2, $\gamma = 10.405$ MHz/T). In the paramagnetic state at temperatures $T > T_N$, the spectra exhibit a broad peak with quadrupolar splitting originating from two Nb unit cell sites. Below T_N the system splits into a double-peak structure around the paramagnetic center. This is a signature of AFM order, with the two peaks originating from the two sublattices where the local hyperfine field (approximately 1 T) adds to, and subtracts from, the externally applied magnetic field. [40] The peak structure onset significantly below T_N, suggesting it is only at these temperatures that the AFM order parameter is well formed. These lower temperatures correspond to the onset of H_{EB} seen in Figure 3.3a, a direct validation of the hypothesis that the exchange bias arises from the coexistence of the AFM order parameter with the SG. It is also notable that the peaks of dilute and excess intercalations are asymmetric (Figure 3.4a,c), in contrast to the stoichiometric case (Figure 3.4b), suggesting that coupling between the SG and AFM exerts an internal exchange field on the ^{93}Nb lattice: SG pinned uncompensated moments align with one AFM sublattice. This provides direct evidence for the existence of exchange coupling between the SG and the AFM order parameters.

Although the low field hysteresis loop is opened by the presence of disorder, the coupling to the antiferromagnetic order parameter means that it cannot close independently of the AFM. This motivates us to study the exchange bias at magnetic fields high enough to drive a metamagnetic transition in the AFM. [1] It has been recently shown that the AFM of the

stoichiometric compound undergoes a metamagnetic transition from stripe to an up-up-up-down phase at $H_{plat} \sim 17$ T, which is characterized by a plateau in the magnetization. [1] This same transition is observed at all compositions, albeit greatly broadened by disorder due to the deviation from $x = \frac{1}{3}$. As shown in Figure 3.5, hysteresis loops close only at fields that go well beyond the metamagnetic transition for any composition - the hysteretic response of the SG is coupled to the magnetic response of the AFM. Importantly, saturating the magnetization at these high fields also ensures that the sample is in the metamagnetic major loop. In conjunction with the spontaneous bias observed at both low and high fields (an effect incompatible with minor loops), these data show that the exchange bias observed cannot be attributed to minor loop effects. Low-field cooled loops are less easy to disentangle from minor loop phenomena, but their robust bias after multiple training loops is also inconsistent with minor loops (extended discussion in Appendix II).

In order to see the effects of the field-cooled history, we study H_{EB} and H_C when the system is cooled in a field H_{FS}, and then cycled across $\pm H_{FS}$. As shown in Figure 3.3d, H_C tends to increase with higher H_{FS} for all compositions, suggesting that the exchange anisotropy of the SG grows as the field in which it was cooled increases, as in typical glassy systems. H_{EB} however is more directly correlated with the response of the AFM order. The $x = 0.30$ sample's peak exchange bias exceeds $H_{EB} \approx 3$ T at relatively low fields, followed by a monotonic decrease at fields beyond H_{plat}, until no memory of magnetization history remains and $H_{EB} \to 0$ (Figure 3.3b). The $x = 0.31$ sample follows a similar trend but subsequently plateaus at high fields, suggesting a marginally more robust exchange bias (Figure 3.3b). For $x = 0.35$, H_{EB} shows a kink at the metamagnetic transition, but interestingly it saturates at high fields to around $H_{EB} \approx 1$T, substantially higher than the diluted systems (Figure 3.3b). For an exchange bias, this is orders of magnitude greater than observed in typical heterostructure or SG systems, [27] but actually much closer to many theoretically predicted values in the absence of disorder. [41] The large bias is housed within the uncompensated moments of the SG, pinned by the coexisting AFM.

Our data suggests that the bias can be understood by considering the interplay of energy landscapes between the SG and AFM, as well as their exchange coupling. In the Sherrington-Kirkpatrick model, each possible state in an ergodic landscape of possible spin configurations is roughly interchangeable when looked at through the lens of spatial spin fluctuations. Above the SG transition, the accessible states are energetically equivalent. Below the SG transition, this ergodicity is broken by the freezing of the random spin texture. [31] However, the other possible states are only weakly distinguished in energy, so that effects like exchange bias which rely on restricting the accessible phase space volume are generally small (of the order of 0.01T). In contrast, in an easy-axis AFM only one of two degenerate states is possible for a local spin, corresponding to distinct spin orientations. Indeed, experiments on the present system with an in-plane field $H//ab$, reveal significantly smaller H_{EB}, on the order of a typical SG exchange bias (see Appendix I), confirming that the phase space of in-plane configurations is unaffected by the coexisting AFM. However, our measurements of giant exchange bias in the interlayer direction suggest that the coexistence of an AFM biases the glassy landscape, strongly distinguishing the possible spin states in energy by leveraging

the sublattice broken symmetry of the AFM. This is the origin of the bias; in changing the landscape of the SG, the uncompensated moment becomes pinned by the coexisting texture of the AFM.

Our intercalation series further allows us to uniquely describe the roles that glassy disorder and AFM anisotropy play in exchange bias systems. A comparison of the relaxation dynamics indicates that the glass phase is more polarizable, thermally persistent, and relaxes more slowly as iron concentration decreases from over- to under-intercalated samples (Figure3.1b,d and Figure3.18). This trend follows the trend of the maximum amplitude of the exchange bias field: below the metamagnetic transition, the glassier samples are more responsive to their field history, resulting in a correspondingly larger exchange bias amplitude (Figure 3.3d). Above the metamagnetic transition, the relative stability of the AFM order parameter determines the robustness of the bias. In Figure 3.5 we show data from samples field-cooled at H_{FC}, but swept beyond $\pm H_{plat}$. This way, the effect of the field-cooled history of the SG can be separated from the effects of sweeping across the metamagnetic transition. As can be seen, in every case H_{EB} saturates at a single value at any field that exceeds H_{plat}, approaching 0 T, 0.3 T and 1 T for $x = 0.30$, 0.31 and 0.35 respectively (note, the figure shows examples of both 30 T and 35 T field sweeps, both greater than H_{plat}). These values are the same asymptotic values approached at high-field in Figure 3.3b, suggesting that the exchange bias of the SG depends on the ground state of the AFM.

The resilient, larger exchange bias that results from over-intercalation can be understood by considering its local structure. In the under intercalated samples, vacancies are introduced in the AFM lattice, whereas in the over intercalated sample the glass component instead sits on interstitial positions throughout the fully packed AFM structure. As the AFM component of the over-intercalated sample is fully intact, the anisotropy of the AFM and its ability to strongly bias the SG is retained even at high fields, resulting in a significantly larger exchange bias of approximately 1 T in comparison to the exchange bias plateau observed in the $x = 0.31$ system. NMR experiments support a more robust AFM in over-intercalated samples: the AFM order parameter appears at higher temperatures and with more intact fine structure than the under-intercalated sample. This is further evidenced by heat capacity profiles, as under-intercalated samples are featureless, while the over-intercalated sample displays a broad peak (further discussion in Appendix). The nature of the defects determines how easily they can be pinned, and therefore the maximum bias value to the SG, but the robustness of the AFM determines the degree of this pinning, and therefore whether the exchange bias can be maintained at high magnetic fields. This division of labor demonstrates a strategy unique to the literature, and broadly applicable in the design of new giant exchange bias phases.

Classic exchange bias is thought to be driven by a "hidden" disordered FM/AFM interface, where pinned uncompensated moments are localized and pinned by the AFM phase. [19] Here, we remove the spectator FM phase in a unique circumstance of intertwined SG/AFM phases. The present system does not rely on pinning at just a thin film interface, but throughout the entire volume of the sample, essentially creating a *macroscopic* model interface, which reveals critical insight about general exchange bias mechanisms: the cooperative

action of SG and AFM order compromises the ergodic landscape of the SG, forcing the uncompensated moment to be pinned to one sublattice. Importantly, the coexistence of SG and AFM phases has been established in multiple systems [42–45], and their interplay may have a direct connection to systems where disordered AFMs have been extensively studied in the context of the random-field Ising model. [46] In this case it is well established that random fields associated with disorder interact with the AFM lattice, directly influencing the avalanche of domain flips in applied magnetic fields. [47, 48] Random field models of exchange bias in bilayer systems, which build upon these foundations, indeed afford results that hew closely to experimental exchange bias data. [21, 41, 49] In this light, the intimate coupling between an uncompensated SG and a highly anisotropic AFM within a single crystal unsurprisingly results in exchange bias orders of magnitude larger than in bilayer systems. In principle, this mechanism also pertains to bilayer systems, and suggests a material design strategy that incorporates anisotropy and magnetic disorder as a path to larger bias materials with broader technological application.

3.2 Methods

Single crystals of Fe_xNbS_2 were synthesized using a chemical vapor transport technique. More details can be found in Chapter 2. In short, a polycrystalline precursor was prepared from iron, niobium, and sulfur in the ratio $x : 1 : 2$ (Fe:Nb:S). The resulting polycrystalline product was then placed in an evacuated quartz ampoule with iodine as a transport agent (2.2 mg/cm^3), and put in the hot end of a two zone MTI furnace with temperature set points of 800 and 950 for a period of 7 days. High quality hexagonal crystals with diameters of several millimeters were obtained. Low field magnetization measurements were performed using a Quantum Design MPMS-3 system with a maximum applied magnetic field of 7 T. High field magnetization measurements were performed at NHMFL using a Vibrating Sample Magnetometry system with a maximum applied magnetic field of 35 T. NMR measurements were performed using the spin-echo technique, in the Condensed Matter NMR lab at NHMFL, using a home-built NMR spectrometer with quadrature detection. Measurements were done using the Hahn pulse sequence. The NMR signal was calculated by summing up the area below the echo peak. The magnetic field was varied between 6 T and 10 T at various temperatures from 4.2 K to 100 K. The magnet was calibrated using a standard current-field calibration curve, which is routinely checked with a calibrated sample. Heat Capacity measurements were performed using a XENSOR AC-sensor in a Cryogen-free magnet system. Powder X-ray diffraction measurements were performed using a Rigaku Ultima-4 system with a Cu K-α radiation. Energy dispersive X-ray spectroscopy was performed with an Oxford Instruments X-MaxN 50 mm^2 system. To perform inductively coupled plasma optical emission spectroscopy, the samples were first digested in hot 65% nitric acid, which was subsequently treated with an excess of HF to ensure complete dissolution of niobium, and the solutions were subsequently diluted to appropriate concentrations. A Perkin Elmer Optima 7000 DV ICP-OES was used to perform inductively coupled plasma optical emission

spectroscopy.

3.3   Appendix I: Additional Measurements

This section provides a number of additional and unabridged measurements.

Powder X-ray Diffraction

Powder X-ray Diffraction (PXRD) measurements and analysis were performed on all samples (Figure 3.6) to confirm their crystal structure. All various intercalations were best fitted to the $2H\text{-}Fe_{1/3}NbS_2$ structure with the space group $P6_322$. The refined in-plane a-b lattice parameters were found to be constant up to the refinement error (Figure 3.7). The refined c-axis was found to monotonically increase with intercalation, producing the values 12.18 Å, 12.19 Å, 12.22 Å, 12.27 Å respectively for (a), (b), (c) and (d). This is in agreement with previous studies on Fe_xTaS_2 which correlated an increase in the c-axis with increasing intercalation of iron [50].

Transmission Electron Microscopy

Transmission Electron Microscopy (TEM) measurements were performed on x = 0.31, x = 0.30 intercalations. Both samples corresponded to the $2H\text{-}Fe_{1/3}NbS_2$ structure (Figure 3.8-a). Figure 3.8 shows TEM images of the x = 0.31 sample with a characteristic atomic order of the three main axes: [001], [100] and [1$\bar{2}$0] (corresponding to Figure 3.8-b-d respectively).

Large scale TEM scans on the x = 0.30 sample are presented in Figure 3.9. A clear homogeneous spread of the Fe atoms is indicated along two main axes [100] and [1$\bar{2}$0]. The large scans sizes (35nm, 50nm and 100nm) allows us to determine this homogeneity up to the instrument limit.

Energy Dispersive X-ray Spectroscopy

Energy Dispersive X-ray Spectroscopy (EDS) measurements were performed on all four intercalations (Figure 3.10) in order to extract the percentage of iron intercalated between the NbS_2 layers. The dispersion spectroscopy and the accompanied fits presented produce the three elements ratio for all four intercalation. From this ratio the intercalation level (x) is calculated to be (a) x = 0.30 ± 0.02, (b) x = 0.31 ± 0.02, (c) x = 0.33 ± 0.02 and (d) x = 0.35 ± 0.02.

Additional EDS spatial resolved maps were measured on the x = 0.30, x = 0.31 and x = 0.35 intercalations in order to examine the distribution of each element. All intercalations indicate a homogeneous distribution over an area of approximately 900 μm^2 (Figure 3.11). This is another confirmation of the intercalation quality inside the sample.
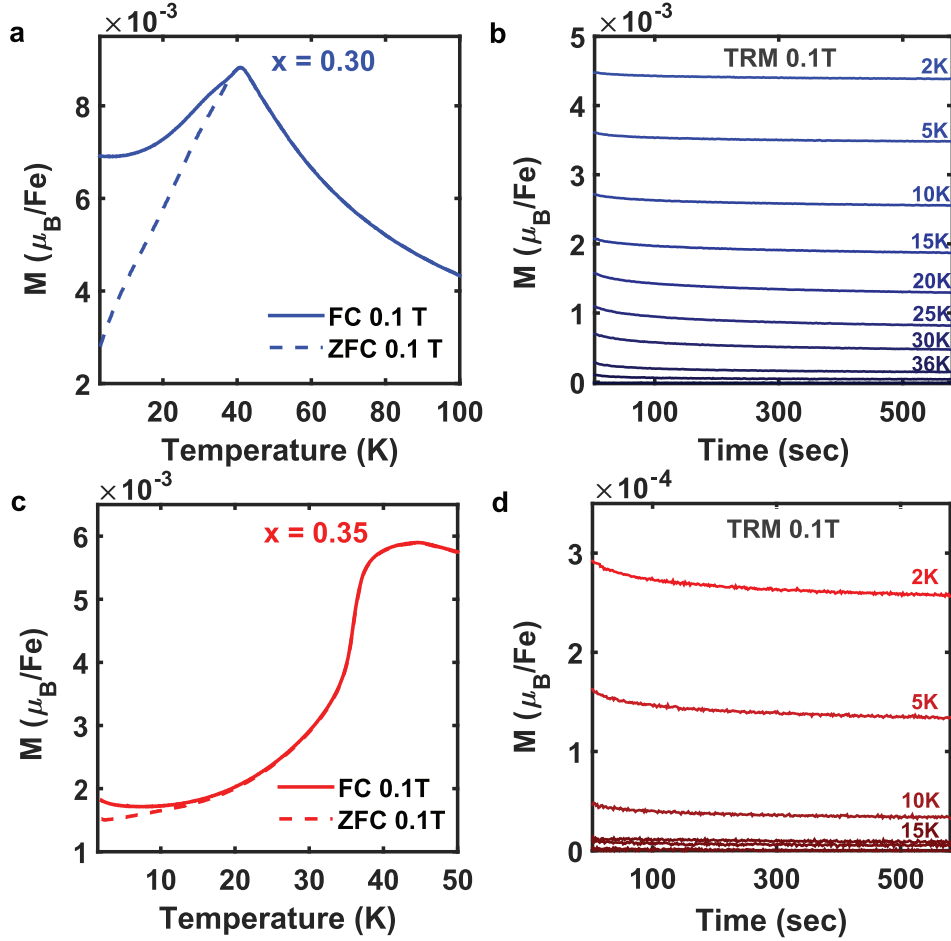
Figure 3.1: SG characterization of Fe$_x$NbS$_2$ for $x = 0.30$ and $x = 0.35$. (a),(c) 0.1 T magnetization versus temperature curves for each intercalation value: both the FC (solid line) and ZFC (dashed line) curves are shown. The AFM transition temperature (T_N) correlates to the sharp magnetization drop (approximately 41 K for x = 0.30 and 37 K for x = 0.35). The divergence of the FC and ZFC curves demonstrates the onset of a glassy frozen moment, which we identify as the effective SG freezing temperature (approximately 38 K for x = 0.30 and 15 K for x = 0.35). From Curie-Weiss fits we extract the effective moment to be 5.4, 5.2 and 5.4 μ_B/Fe for x = 0.30, 0.31 and 0.35 intercalations respectively (for full data and analysis see Appendix I). (b),(d) Thermoremanent magnetization (TRM) measurements performed at various temperatures after field cooling the samples in a field of 0.1 T. The relaxation measurements are presented after the magnetic field was removed. The y-axis exhibits an order of magnitude difference between $x = 0.30$ (b) and $x = 0.35$ (d) intercalations. The appearance of relaxation dynamics is correlated with the glassy state. Additional isothermal remanent magnetization measurements, performed after zero field cooling the samples, present similar dynamics indicating a common relaxation mechanism in both routines (see Appendix for full analysis).
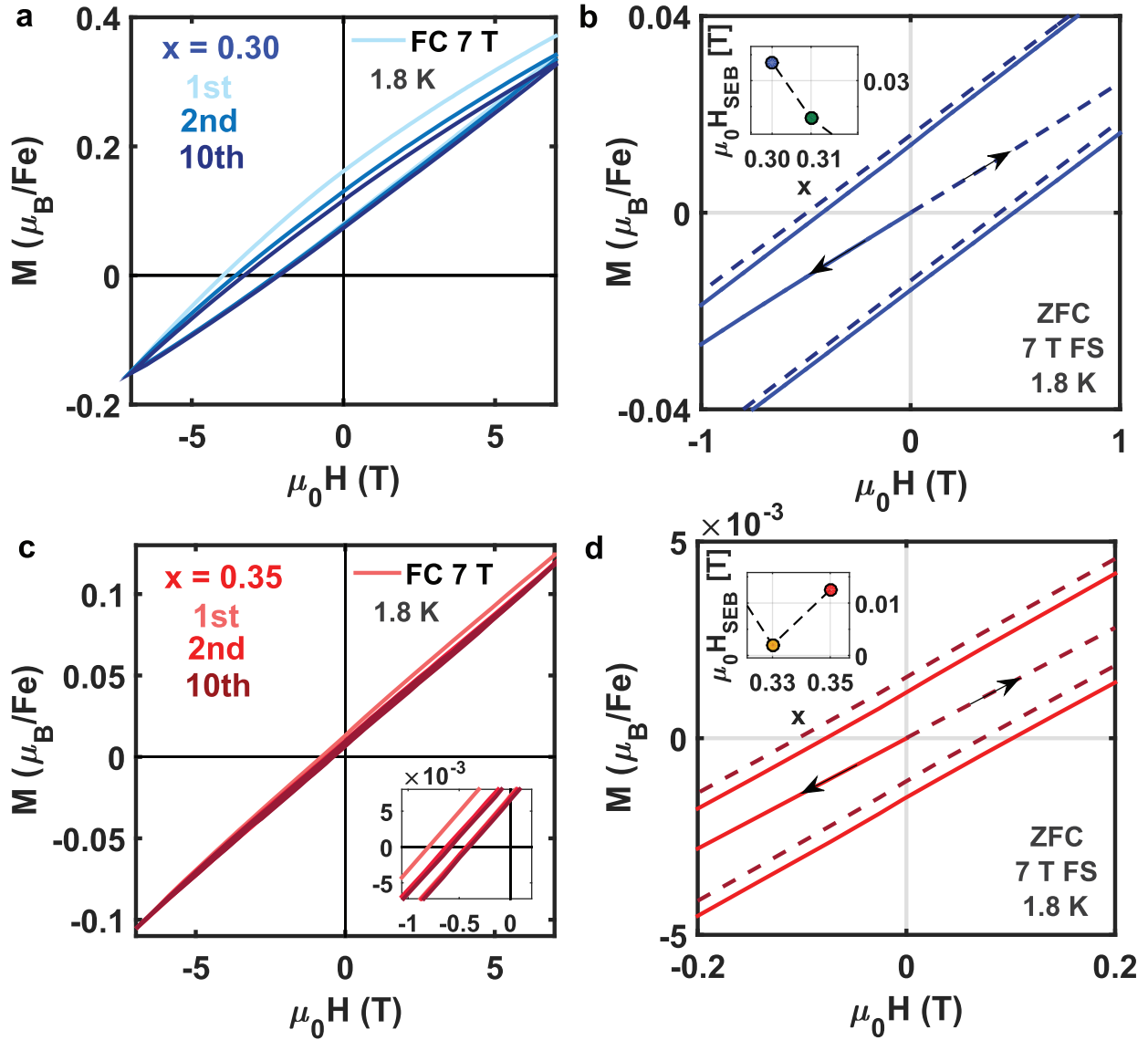
Figure 3.2: Low field exchange bias characterization. (a),(c) Shifted magnetic hysteresis loops measured after cooling the samples from above the transition temperature. The slight decrease of the shifted hysteresis loops and their coercivity after 10 consecutive field sweeps demonstrates a training process in which the exchange bias is robust (see inset for $x = 0.35$ intercalation). (b),(d) Zoom-in on hysteresis loops taken at 1.8 K after cool-down without any external field. For each intercalation the magnetic field sweep was performed twice: starting the sweep in the negative direction (solid lines) or the positive one (dashed lines). A spontaneous exchange bias of a few 100 Oe which is dependent on the initial sweep direction is visible. Insets: The monotonic increase of the exchange bias field while departing the $x = \frac{1}{3}$ intercalation.
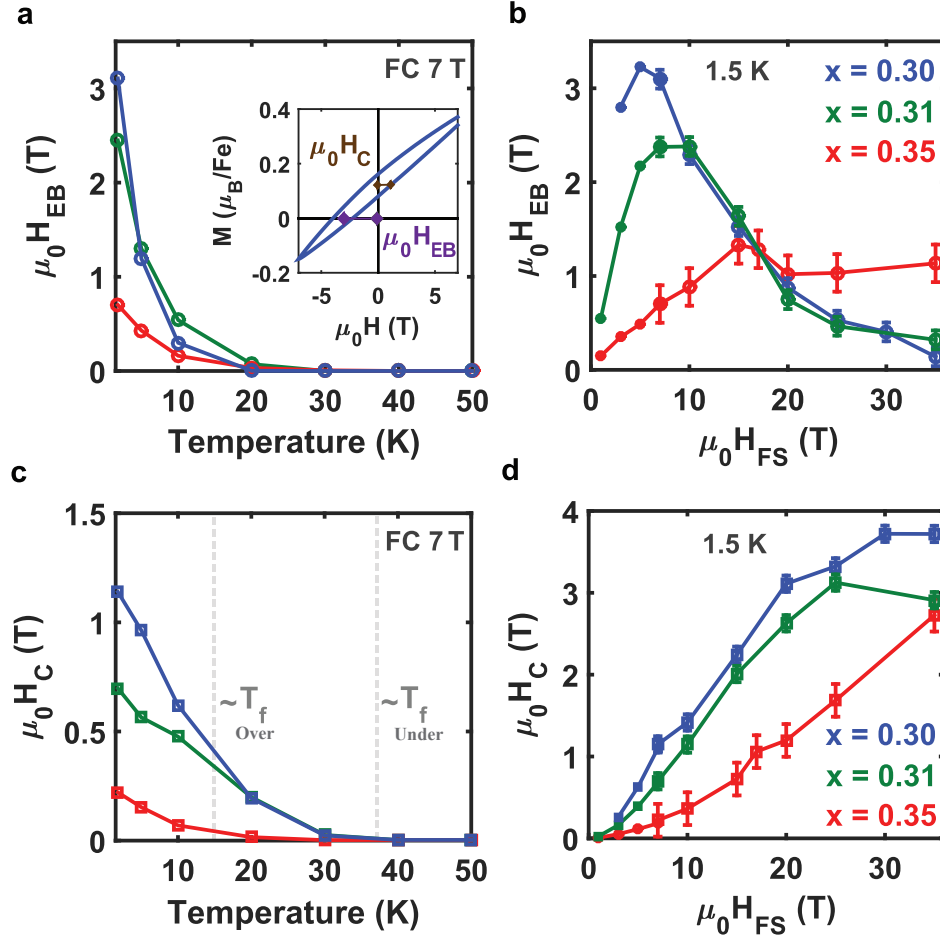
Figure 3.3: The temperature and field sweep dependencies of the exchange bias. (a),(c) The temperature dependence of the extracted exchange bias and coercive fields for $x = 0.30, 0.31, 0.35$ intercalations, after cooling in a 7 T magnetic field from above the AFM transition. Inset (a): The exchange bias field (purple) was extracted from each loop by taking the average of the x-intercepts: $H_{EB} = \frac{H_{\text{int 1}} + H_{\text{int 2}}}{2}$. The coercive field (brown), H_C, was calculated from the half width of the hysteresis loop at the average of the y-intercepts. (c) The dashed lines mark the approximate SG freezing temperature for under(over)-intercalated samples, according to the FC/ZFC divergence presented in Figure 3.1a,c. (b),(d) The extracted exchange bias and coercive fields versus the sweeping field for $x = 0.30, 0.31, 0.35$ intercalations, measured at 1.5 K. The $x = 0.30$ intercalation was cooled in a 7 T magnetic field. For $x = 0.31, 0.35$ intercalations the cooling fields are identical to the field sweep range. H_{EB} shows a non-monotonic response as the swept field passes through the metamagnetic transition. For under-intercalated samples the exchange bias at high fields is suppressed, vanishing for $x = 0.30$ intercalation and saturating (around 0.3 T) for $x = 0.31$. Contrarily, for over-intercalation ($x = 0.35$) the high field exchange bias is saturated around 1 T. H_C grows monotonically with no distinct variation in the field range of the metamagnetic transition.
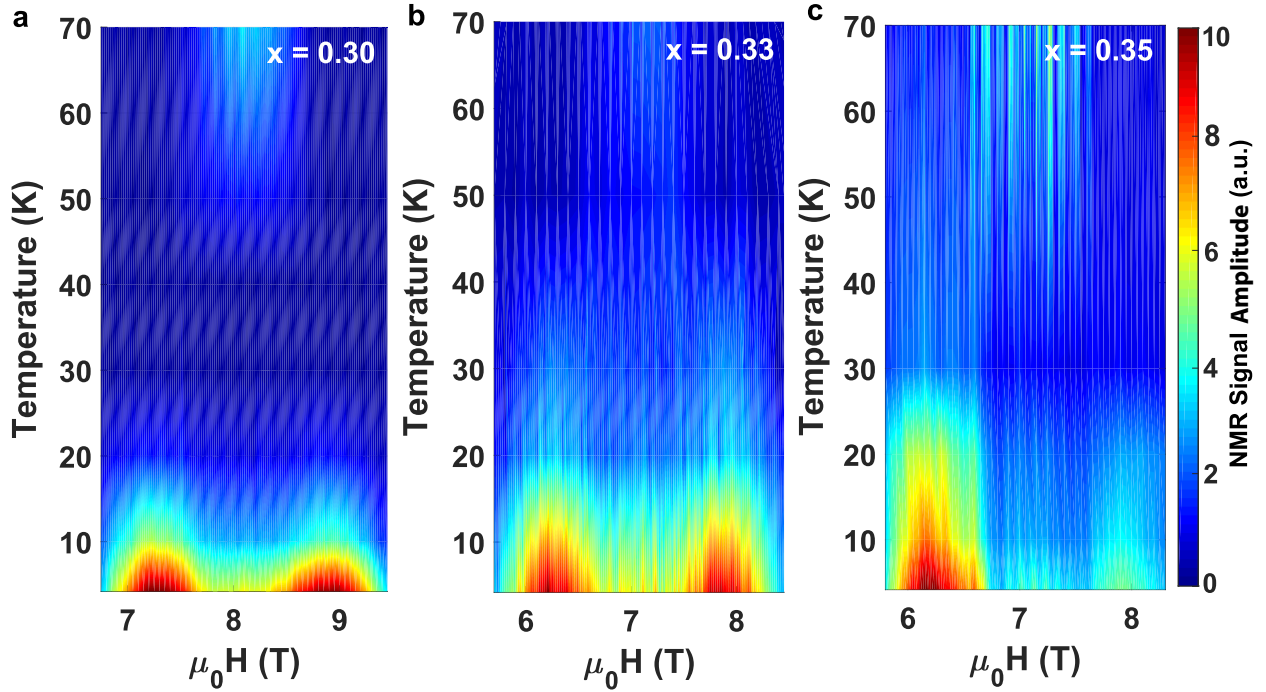
Figure 3.4: NMR measurements performed on $x = 0.30, 0.33, 0.35$ intercalations. Field-swept NMR spectra at 85 MHz ($x = 0.30$) and 74.5 MHz ($x = 0.33, 0.35$) for several temperatures between 70 K to 4.2 K. The samples were cooled and measured in a magnetic field oriented along the c-axis. For $x = 0.30$ intercalation the 4.2 K field sweep was ZFC. The presented color maps of the NMR amplitude (normalized and scaled by their maximum value) are interpolations of the raw data. All samples show a single paramagnetic quadrupolar spectra at high temperatures which splits into two broad peaks at low temperatures due to AFM ordering. (a) As the temperature is lowered the Nb peaks broaden for the $x = 0.30$ sample. At temperatures below 20 K, two broad peaks indicative of a long-range AFM order emerge. Additionally, an asymmetry component between the two peaks is present. (b) The stoichiometric sample ($x = 0.33$) shows a similar peak structure but with no asymmetry. For this intercalation, the AFM phase is not affected by cooling in a magnetic field. (c) For the $x = 0.35$ sample the Nb peaks are clearly visible at all temperatures, indicating the iron lattice is highly ordered. Below 25 K, two broad peaks with a massive asymmetry component appear.
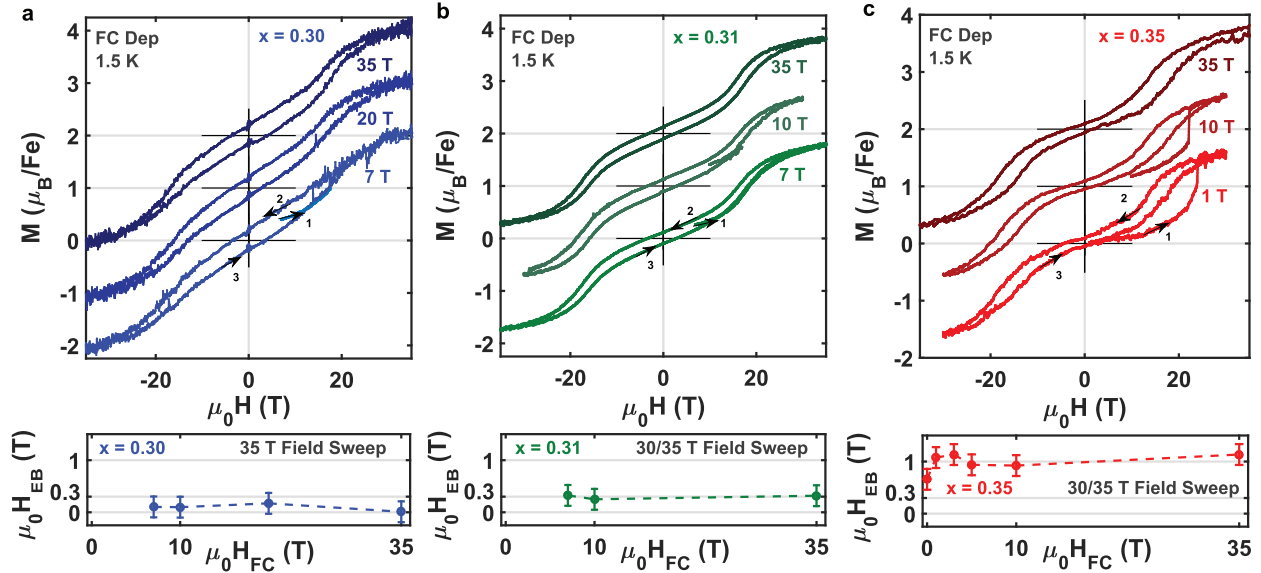
Figure 3.5: High field exchange bias. Out-of-plane magnetization versus high magnetic field sweeps (up to 35 T) measured after cooling in various magnetic fields from above the AFM transition temperature down to 1.5 K. Each loop is offset on the y-axis by 1 μ_B/Fe. The arrows/numbers presents the sweep direction of the hysteresis loop for each intercalation. (a) The $x = 0.30$ sample does not show any significant exchange bias when swept up to 35 T in the range of the cooling fields taken (7 T - 35 T). (b) For the $x = 0.31$ sample, a stable exchange bias of approximately 0.3 T is captured in the same field range (7 T - 35 T). (c) Finally, the $x = 0.35$ sample shows a clear exchange bias of around 1 T at all implemented cooling fields (0 T - 35 T), demonstrating the high field sweep connection to the formation of exchange bias. Moreover, the metamagnetic transition clearly appears (on the initial field sweep direction) when the cooling field is weak enough, subsequently merging into the major hysteresis loop.

Inductively Coupled Plasma Optical Emission Spectroscopy

A Perkin Elmer Optima 7000 DV ICP-OES in the Department of Chemistry at the University of California, Berkeley was used to perform inductively coupled plasma optical emission spectroscopy (ICP-OES). To digest the samples of FexNbS2, 2-8 mg of single crystals were heated in 1 ml hot nitric acid (86%). From this solution, Nb oxide precipitated, which was solubilized by addition of 1 ml HF (48%). The resulting solution was diluted to an appropriate concentration to perform the experiment, and the digestion vial was rinsed multiple times with HF to ensure complete dissolution. Due to the small sample sizes, analysis was limited to determining molar ratios of Fe and Nb. The fitted ICP-OES ratios of Fe/Nb are presented in table 3.1. For each growth number we present the intercalation
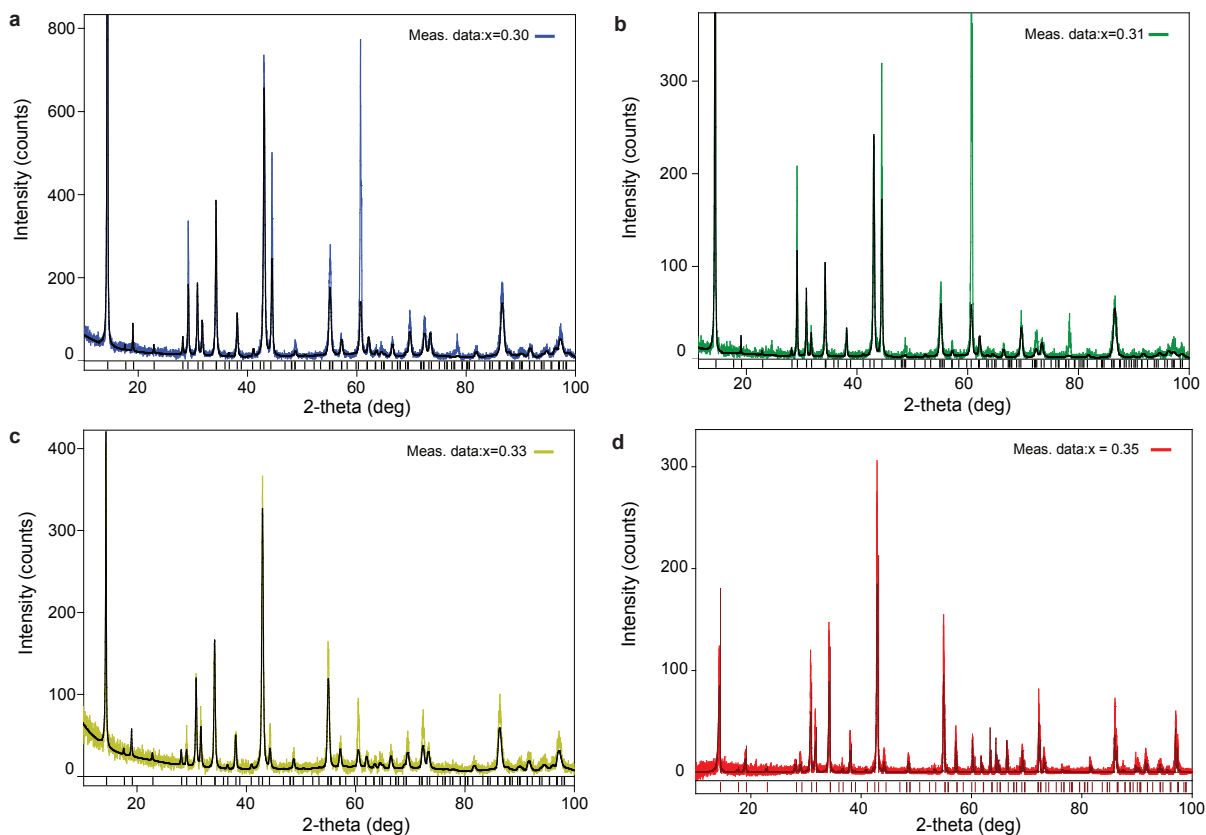
Figure 3.6: PXRD measurements on the four different intercalations studied. Blue, green, yellow and red correspond to X-ray measurements done on x = 0.30, x = 0.31, x = 0.33 and x = 0.35 respectively. The black curves are fits to the 2H-Fe$_{1/3}$NbS$_2$ structure.

labeling used in the main text along with the ICP-OES fitted ratio.

Heat Capacity

The AC heat capacity measurements (Figure 3.12) show a clear correlation to our magnetization measurements plotted in Figure 1a,c in the main text. As iron is removed from the fully packed x = 0.33 sample, the phase transition peak almost entirely vanishes, leaving a small kink close to the peak position extracted from the magnetization measurements. These curve profiles are also distinct from a typical glassy state [27]. In the context of the NMR, this suggests that the AFM and spin glass phases are highly correlated in the under-intercalated samples (x = 0.31 and x = 0.30), and the AFM order parameter is less robust than in the fully packed sample. Further, this data points to the homogeneity of the samples, for if the two phases were segregated in discrete volumes throughout the sample, the measurement
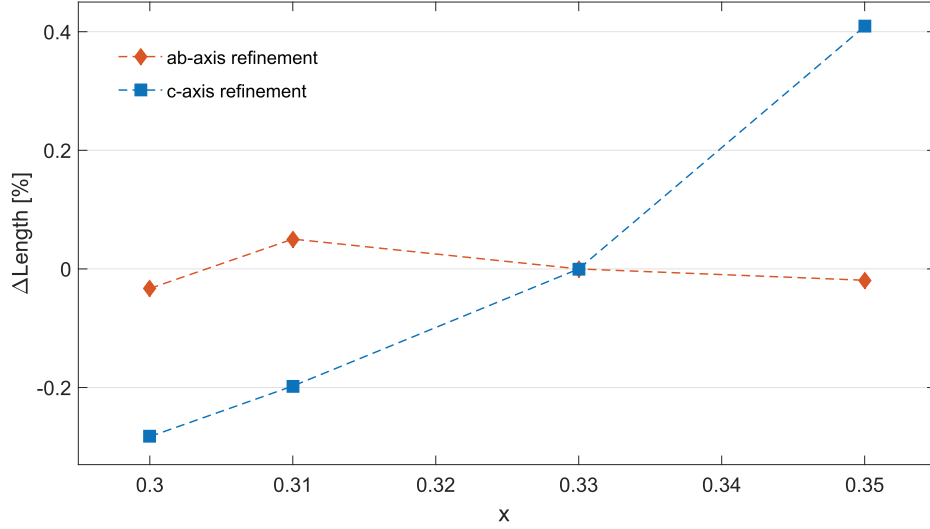
Figure 3.7: Dependence of the refined lattice parameters with respect to intercalation levels. The lattice parameters are plotted as the percentage change compared to the x = 0.33 intercalation level .

Growth Number	Label in text	ICP Fe/Nb Ratio
AG2437	x = 0.30	0.300±0.009
AG2353	x = 0.31	0.309±0.003
AG2312	x = 0.33	0.330±0.006
AG2334	x = 0.35	0.351±0.001

Table 3.1: ICP-OES fitted values

would indicate a peak associated with AFM order overlaid with a broad glassy background.

In the higher intercalation (x = 0.35) there is a significant reduction of the heat capacity anomalies compared to the x = 0.33 sample. These features, together with the magnetization measurements, suggest that the broadened peak is consistent with an intact AFM which is strongly associated with a glass phase on the time scale of this measurement. Importantly, these measurements also point to the homogeneity of the sample: the curve profile is not simply the additive profile one would expect from segregated volumes, but instead suggests that the AFM order itself is modulated by coupling with the coexistent glass.

A comparison between the AC heat capacity of sample x = 0.33 (Figure 3.12-c) to a similar intercalation in previous studies [35] resolve in very good agreement. Additionally, a reduced/vanishing heat capacity peak for $x < \frac{1}{3}$ is also seen in previous studies [35,36].
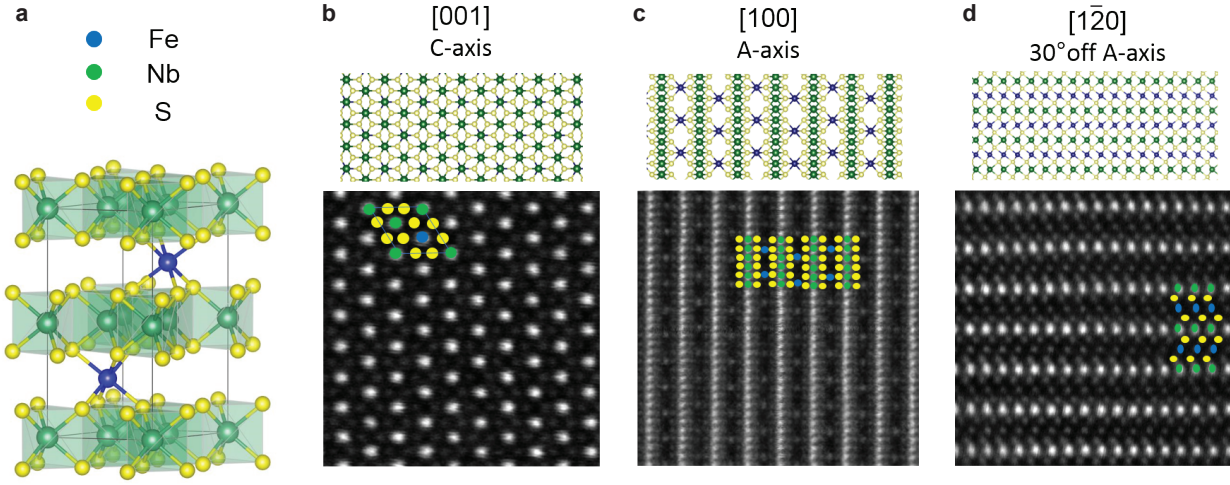
Figure 3.8: Structure and TEM measurements of $Fe_{x=0.31}NbS_2$. (a) The 2H-$Fe_{1/3}NbS_2$ crystal structure with the space group P6$_3$22 is illustrated. Iron, niobium ans sulfur atoms are presented as blue, green and yellow circles respectively. (b) [001] out-of-plane TEM image (top view) showing the perfect hexagonal structure of the niobium and sulfur atoms. (c) [100] in-plane TEM image elucidating the iron atoms are ordered with every 3rd niobium atom. (d) [1$\bar{2}$0] in-plane TEM image showing characteristic high symmetry axis atom positions.

Magnetization Field Sweeps Raw Data

The temperature dependent magnetization versus low field scans which were analyzed and presented in the main text (Figure 3a,c) are plotted in Figure 3.13. All scans were performed by FC in a 7 T magnetic field from above the AFM transition temperature.

We additionally plot the field cool dependent magnetization versus low field scans performed at 1.8 K (Figure 3.14). The evolution of the exchange bias and coercive field for low fields is demonstrated in panels d and e.

The field sweep dependent magnetization versus high magnetic field scans which were analyzed and presented in the main text (Figure 3b,d) are plotted in Figure 3.15.

Curie-Weiss Fits

Curie-Weiss fits were performed on the susceptibility data for x = 0.30, 0.31 and 0.35 intercalation values (Figure 3.16). The function $\chi_m = \frac{C}{T-\Theta}$ was used, where C is the Curie Constant and Θ_{CW} is the Curie temperature. The effective moment (μ_{eff}) of each curve was calculated by the known conversion of the fitted Curie Constant ($\mu_{eff} = \sqrt{8C}$). Table 3.2 shows the corresponding Curie temperatures (Θ_{CW}) and effective moments (μ_{eff}) for all intercalations.
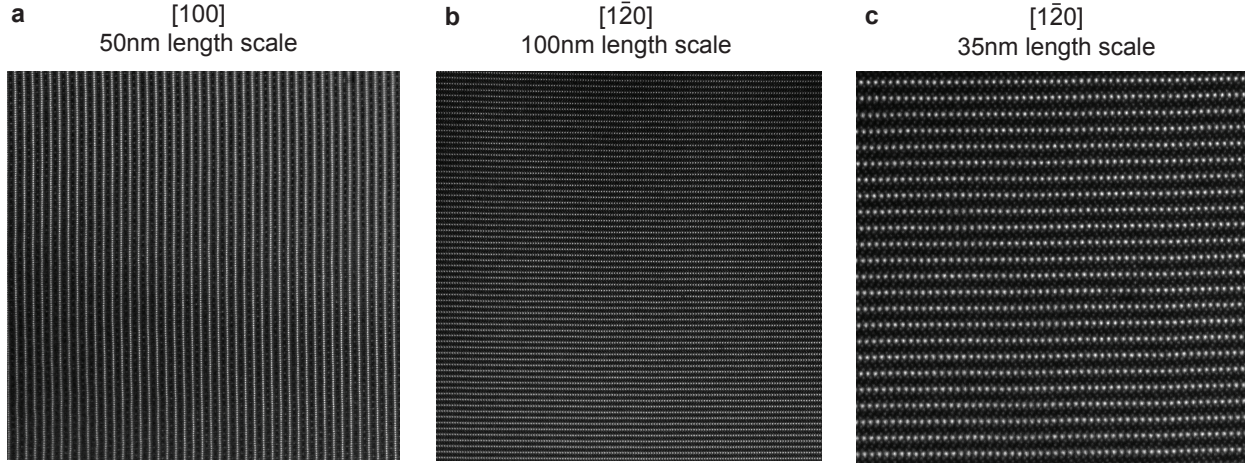
Figure 3.9: Large scale TEM measurements of $Fe_{x=0.30}NbS_2$. (a) [100] in-plane TEM image showing the iron atoms are spread homogeneously without any patches forming on a 50nm length scale. (b)-(c) [1$\bar{2}$0] in-plane TEM image showing the same homogeneous structure formed on a 100nm and 35nm length scale respectively.

	$\Theta_{CW}(K)$	μ_{eff} (μ_B/Fe)
$Fe_{0.35}NbS_2$	-50.7	5.4 $\pm$0.2
$Fe_{0.31}NbS_2$	-39.7	5.2 $\pm$0.2
$Fe_{0.30}NbS_2$	-40.3	5.4 $\pm$0.2

Table 3.2: Curie-Weiss fitting results

The analyzed effective moment per iron is similar between all intercalations including the fully packed structure (x = 0.33) [1]. Albeit when comparing the total moment relative to x = 0.33, a higher moment is captured for the x = 0.35 intercalation, corresponding to the relative increase of excess iron. This difference is related to the origin of the SG state between under- and over-intercalations. For the under intercalated samples, the fluctuating moment is overall conserved because of similar AFM correlations differed by deficiencies of iron sites in the magnetic lattice. Contrarily, for the over intercalated sample the excess iron spins, which are not part of the AFM lattice, add to the fluctuating moment their percentage change.

Relaxation Analysis

Both isothermal remanent magnetization (IRM) and thermoremanent magnetization (TRM) measurements were performed on each intercalation value. As described in the main text,
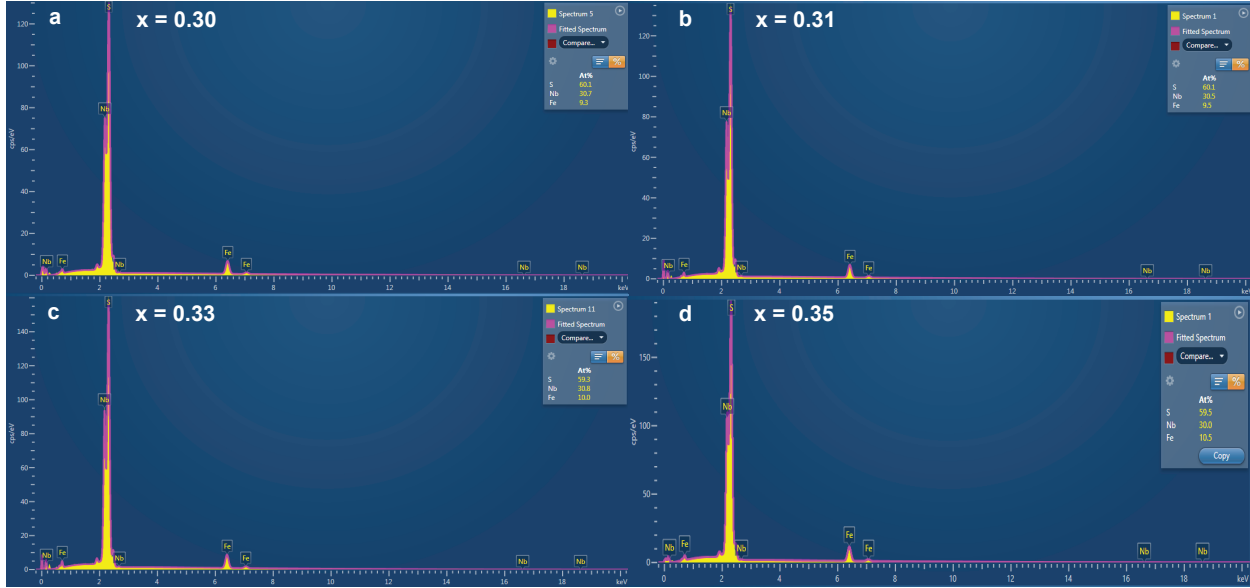
Figure 3.10: EDS measurements of the four intercalated samples are presented. The dispersion spectroscopy (Yellow curves) and the accompanied fits (Purple curves) give an atomic ratio (S:Nb:Fe) of 1.96:1:0.30 (a), 1.97:1:0.31 (b), 1.93:1:0.33 (c) and 1.98:1:0.35. These ratios are accurate up to an estimated error of ± 0.02.

IRM measurements were carried out by cooling samples down to 5 K without a field, applying a field for one hour and then removing the field, while TRM measurements are taken by cooling down to 5 K in the presence of a field, holding for an hour, and then removing the field.

The relaxation measurements for both IRM and TRM were best fitted (Figure 3.17) using the typical stretched exponential decay function of the form $M(t) = M_0 e^{-(\frac{t}{\tau})^{1-n}}$, where M_0 is the initial moment, τ is the characteristic relaxation time and n is the time stretch component [27, 51].

Simpler algebraic $(M(t) = M_0 t^{-a})$, logarithmic $(M(t) = M_0 - Sln(t))$, or simple Debye exponential relaxation $(M(t) = M_0 e^{-\frac{t}{\tau}})$ functions did not accurately describe the relaxation behavior observed [52]. Fits using the modified stretched exponential functions of the forms $(M(t) = M_a e^{-(\frac{t}{\tau})^{1-n}} + Sln(t) + M_0)$ and $(M(t) = M_0 t^{-b} e^{-(\frac{t}{\tau})^{1-n}})$ collapsed back to fit parameters consistent with a simple stretched exponential fit, absent modifications to the function [51, 53]. Together, this suggests that the observed data are consistent with glassy relaxation processes seen in SG systems.

Typical τ values for the glassy materials characterized in this study are in the range of .004-.071 seconds (shown in Table 3.3). Within the context of the coexistent AFM/SG phases suggested in this paper, these small τ values may be suggestive of a cooperative process, where SG relaxation is strongly enhanced by the coexistent AFM phase. Between

	IRM			TRM		
	M_0 [μ_B]	τ [s]	n	M_0 [μ_B]	τ [s]	n
$Fe_{0.30}NbS_2$	0.0119	0.071	0.884	0.0878	0.033	0.990
$Fe_{0.31}NbS_2$	0.0045	0.010	0.907	0.0248	0.014	0.988
$Fe_{0.35}NbS_2$	0.0058	0.009	0.873	0.0066	0.004	0.967

Table 3.3: Relaxation fitting results

IRM and TRM measurements on the same intercalation values, the relaxation times and time stretch components are comparable, indicating a common relaxation mechanism in both routines. The difference between the TRM and IRM measurements (shown in the inset of Figure 3.17-a) was found to be constant across the routine with only minor relaxation, thus further supporting a conserved moment across field changes.

Field Dependence of Magnetization versus Temperature

Temperature dependent magnetization curves together with TRM measurements at different fields for x = 0.30 intercalation (Figure 3.19) and x = 0.35 (Figure 3.18). For the x = 0.35 intercalation the M/H versus T measurements show the glassy state's robustness to high fields, as the ZFC and FC separation is slightly enhanced while increasing the field up to 7 T [Figure 3.18(a)-(d)]. For the x = 0.30 intercalation the SG response is suppressed together with the AFM transition, albeit diverging at lower temperatures [Figure 3.19(a)-(d)]. Similar trends for both cases are captured in the TRM measurements taken at identical fields. For x = 0.35 intercalation we do not see any significant change in the temperature dependent relaxation curves [Figure 3.18(e)-(h)], contrarily to x = 0.30 which indicates a suppression of the relaxed moment [Figure 3.19(e)-(h)] comparable with the respective M versus T splitting temperature.

Aging Memory Effects

During the initial cool-down of a ZFC measurement, a 1 hour pause was taken below the freezing temperature. The sample was then cooled to 1.8 K, and magnetization was measured while increasing the temperature of the sample. This measurement is shown in Figure 3.20, performed on the x = 0.30 sample, and repeated at three waiting temperatures: 20 K, 27.5 K, and 35 K. A dip in the magnetization at each pause temperature was observed. The inset shows $\Delta M = M_{no\ pause} - M_{pause}$, emphasizing the difference between the no-pause and pause measurements. This memory effect originates from the system relaxing into lower energy metastable states during a pause at a given temperature [27,54]. Upon returning to this temperature, it can revert to the local minimum found by the end of the initial pause, illustrating that both time and temperature are key players in determining the accessed states in these systems.

Just as the antiferromagnetism biases the local energy landscape to support a large exchange bias, it ensures the landscape possesses deep minima robust against large perturbative fields, allowing aging effects to occur at much higher fields than those of other SG systems [54].

Exchange bias Anisotropy

We propose the underlying mechanism behind the giant exchange bias relies on biasing of the local multiminima energy landscape of the SG by the coexisting antiferromagnetism. With the predominant ordering direction of the antiferromagnetism being out-of-plane [32], we performed in-plane exchange bias measurements to probe if this enhancement persisted (Figure 3.21). In all intercalation values, we observed only a small separation in the FC and ZFC measurements in magnetization measurements (Figure 3.21a-c). Correspondingly, we measured a reduced exchange bias in all samples that is on the order of those observed in canonical SG systems, indicating that we are only accessing the SG's contribution to the exchange bias (Figure 3.21e). The dependence of the out-of-plane exchange bias on intercalation value (Figure 3.21e inset) illustrates the delicate interplay between the strength of the AFM and glass phases in enhancing the exchange bias. The AFM ordering direction is thus crucial to the origin of the giant exchange bias.

Magnetization Characterization of the x = 0.33 Intercalation

We study our closest intercalation to $x = \frac{1}{3}$ in order to probe the magnetization response of the fully packed regime. ZFC and FC curves do not show any variance in the full temperature range measured (Figure 3.22a). Specifically, the AFM transition has an identical response (between ZFC and FC curves) indicating there is no glassy behaviour up to the limit of our measurement system. Additionally, relaxation measurements show the fast dynamics of the AFM phase with no apparent relaxing moment (Figure 3.22b). Magnetic field sweeps show no reminiscence of hysteresis about zero field (Figure 3.22c), indicating the glassy state is less significant in this intercalation. Furthermore, the sharpness and hysteresis of the metamagnetic transition is pronounced in this inetrcalation (Figure 3.22d), illustrating the variance of this transition in the other intercalations.

Field swept NMR at fixed temperatures

We present the NMR raw data used for constructing the color plot in Figure 4c in the main text. The NMR spectra was measured during field sweeping at fixed various temperatures. The quadrupolar Nb peaks are clearly visible at all temperatures. Below 30 K, two broad peaks with an asymmetry component appear in the NMR spectra.

3.4 Appendix II: Minor Loops

Minor loops are typically defined as a hysteresis loop in which saturation has not been reached by the applied external field [55, 56]. It is well documented that a minor loop, taken after field cooling, may exhibit a shifted hysteresis loop due to the external field being too small to completely reverse the magnetization, which in certain cases has been erroneously reported as an exchange bias [57, 58]. In our study, the dominant AFM coupling endemic to the material precludes a saturation plateau below the metamagnetic transition. However, data taken past this metamagnetic transition indicate a plateau in magnetization, a clear indication that the loops taken in this field regime are major loops, not minor loops.

We additionally point to the more subtle definition of an "effectively saturated system". This definition suggests that a loop is no longer "effectively" minor if the maximum applied field is stronger than the anisotropy field of the material, $H_{max} > H_A$, and should no longer exhibit a shifted minor loop [39, 59–64]. Here, the magnetocrystalline anisotropy fields are on the order of 1 meV [1, 65], a value far below the maximum applied fields within this material. The observation of magnetic saturation in this system is particularly salient in the context of a different giant exchange bias system with competitive maximum exchange bias fields [66], where saturation is never observed. We further note that the observation of a spontaneous exchange bias (Figure 2b,d and Figure 5c in the main text), observed after cooling absent a field, is entirely inconsistent with minor loops. Further, the only systems which display well-defined, spontaneous exchange bias, to our knowledge, are disordered single phases containing FM and AFM/SG domains, or certain SGs themselves [67]. Taken together these data clearly indicate that the exchange bias cannot be conflated with a minor loop throughout a significant portion of the data taken.

We further note that training of the exchange bias loops is further inconsistent with the basic definition of a minor loop (Figure 2a,c in the main text). While magnetic relaxation may clearly play a role in glassy systems such as this, we note that the asymmetry of the training effect (here, comparing the shift in x-intercept on the positive and negative field sweeps) is generally inconsistent with simple magnetic relaxation, and instead consistent with classic exchange bias systems. We next point to recent experiments on FM/SG thin film interfaces, where a clear link between the origin of exchange bias and glassy behavior is established [22]. This and subsequent experimental and theoretical work establish that exchange bias in bilayers is engendered by a glassy, disordered interface between the bilayer, in contrast to the simplistic pinning typically invoked [18, 19]. Here, the glassy dynamics of the glass phase are directly attributed to the training effect, suggesting that the training effect in any exchange biased system is ultimately determined by glassy dynamics at a bilayer interface. Indeed, schemes involving simple interfacial pinning cannot explain the training effect; instead, models incorporating disorder (and hence glassy dynamics) are requisite to understanding the training effect. To the best of our knowledge, a more complex interpretation such as this is needed to explain the training effect, not only in our system, but in exchange biased systems in general. In our text, we build upon this previous work by leveraging an anisotropic AFM coupled to a SG phase within a single phase, resulting in

new design criteria for giant exchange biased systems.

Our observations regarding the interplay of spin glass and AFM order parameters also help separate the observed bias from minor loop effects. As mentioned in the main text, the spontaneous bias observed at both low and high fields, as well as the leveling off of the bias field upon sweeping past the metamagnetic transition, clearly establish that minor loop phenomena is not responsible for the majority of data here. However, at intermediate FC fields, field swept below the metamagnetic transition, disentangling a true bias from a minor loop is more complex. First, the robust training effect observed already distinguishes the shifted hysteresis as a bias rather than a minor loop. Second, we note that the bias trends observed here are entirely at odds with minor loops: since the spontaneous bias seen when sweeping to either low or high fields cannot be explained by minor loop effects, it very difficult to explain the smooth crossover we observe between the regimes by minor loop effects (Figure 3 of the main text). It is much more natural to explain our data by the pinning of the uncompensated moment of the SG, by the AFM spin texture.
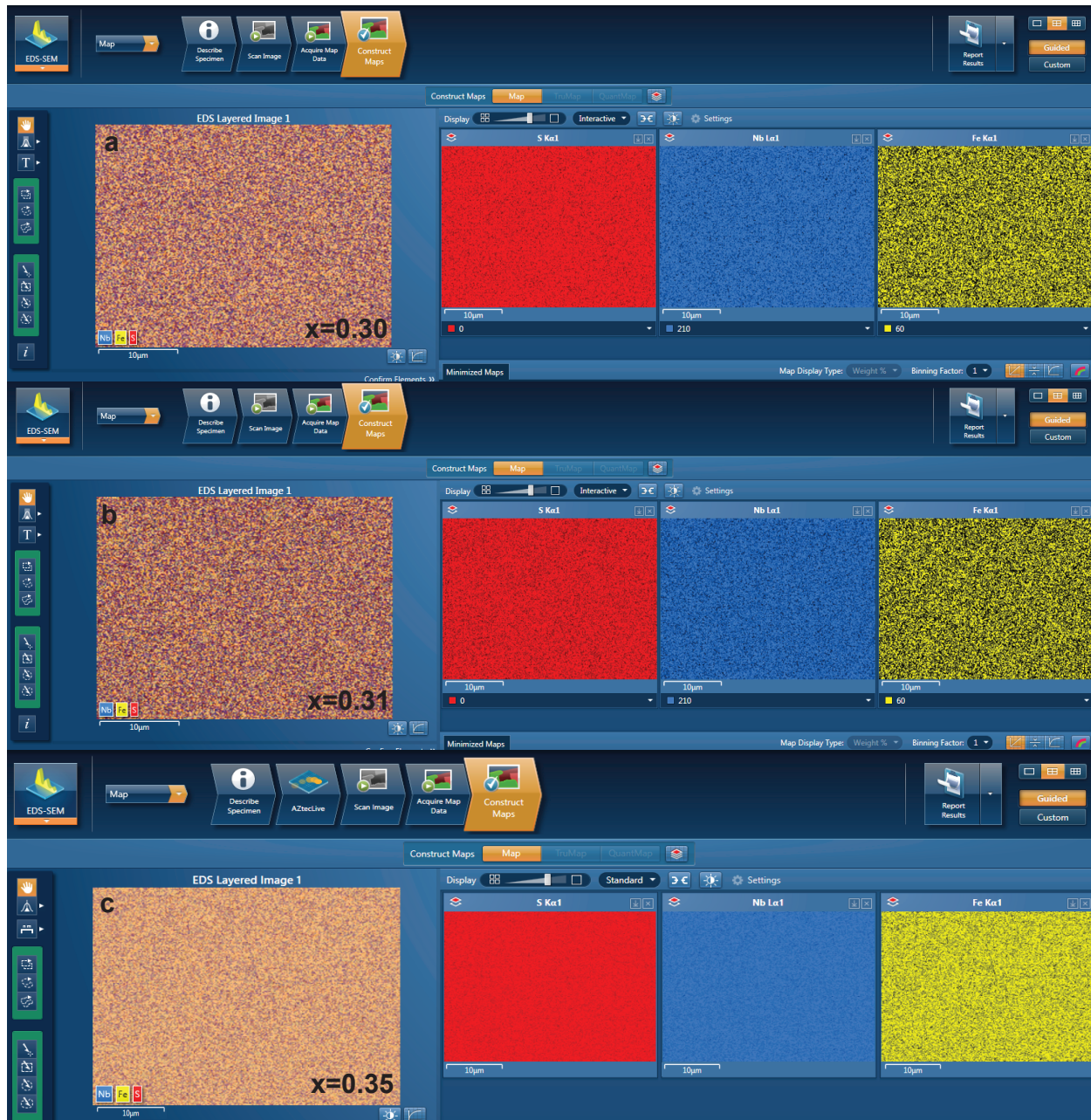
Figure 3.11: EDS distribution maps of the x = 0.30, x = 0.31 and x = 0.35 samples are presented. The scan size for all samples is approximately 900 μm^2. Sulfur (S), Niobium (Nb) and Iron (Fe) are presented in Red, Blue and Yellow colors respectively. A homogeneous distribution is indicated up to the resolution of a Scanning Electron Microscope.
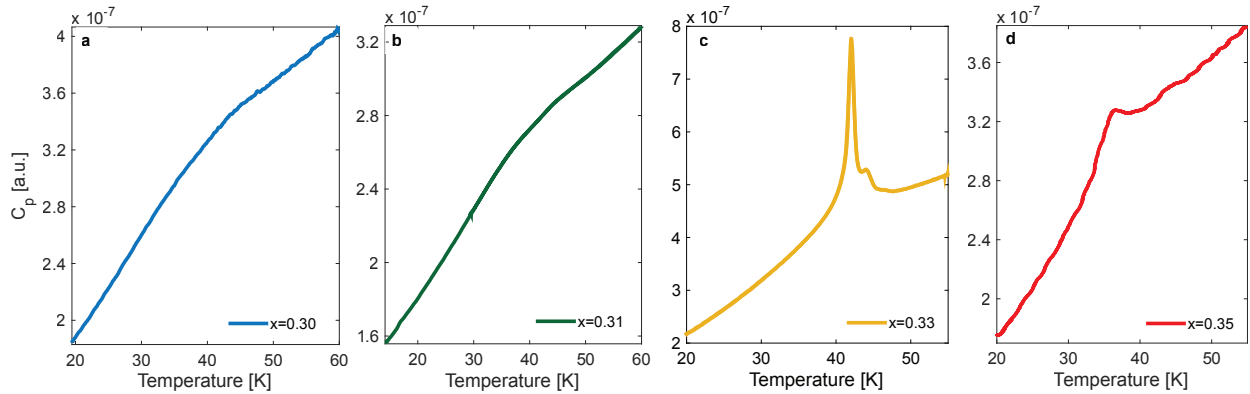
Figure 3.12: AC heat capacity versus temperature measurements of the x = 0.30 (a), x = 0.31 (b), x = 0.33 (c) and x = 0.35 (d) intercalation. Blue, green, yellow and red curves correspond respectively to the intercalation levels state before. Note that the heat capacity is plotted in arbitrary units (a.u.).
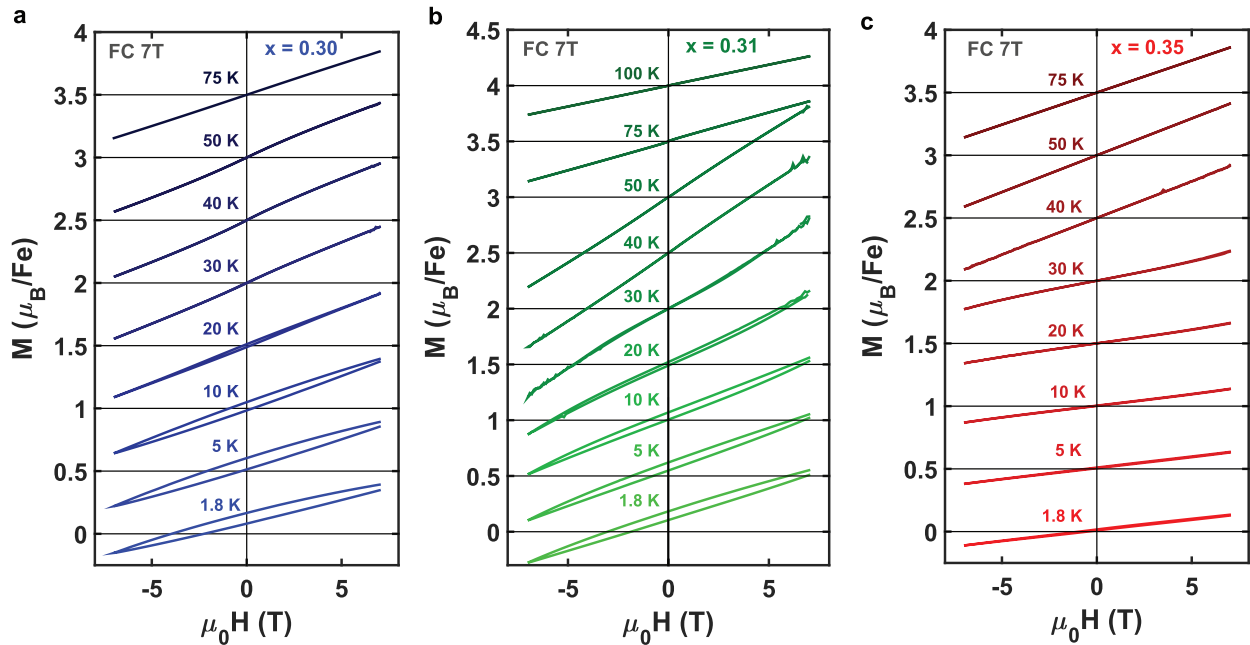
Figure 3.13: Magnetization versus low magnetic field measurements performed on $Fe_{0.30}NbS_2$ (a), $Fe_{0.31}NbS_2$ (b) and $Fe_{0.35}NbS_2$ (c). The temperature dependence of the exchange bias and coercive field is demonstrated, all field cooled under a 7 T external field. All loops were taken from +7 T to -7 T back to +7 T. Each loop is offset on the y-axis by 0.5 μ_B/Fe. The magnetic field was applied along the c-axis of the samples.
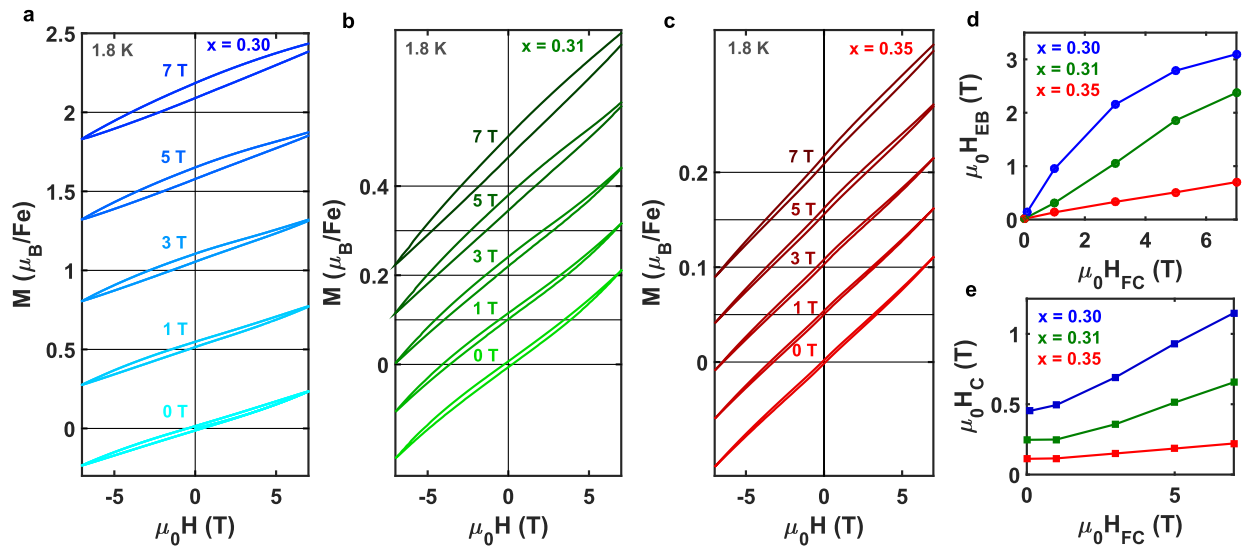
Figure 3.14: Magnetization versus low magnetic field measurements performed on $Fe_{0.30}NbS_2$ (a), $Fe_{0.31}NbS_2$ (b) and $Fe_{0.35}NbS_2$ (c). The cooling field dependence of the exchange bias and coercive field is demonstrated, all performed at 1.8 K. All loops were taken from +7 T to -7 T back to +7 T. Each loop is offset on the y-axis by 0.5 (a), 0.1 (b) and 0.05 (c) μ_B/Fe. The magnetic field was applied along the c-axis of the samples. (d) The extracted exchange bias field versus the cooling field, measured at 1.8 K, for x = 0.30, 0.31 and 0.35 intercalations. (e) The extracted coercive field as a function of cooled field, measured at 1.8 K.
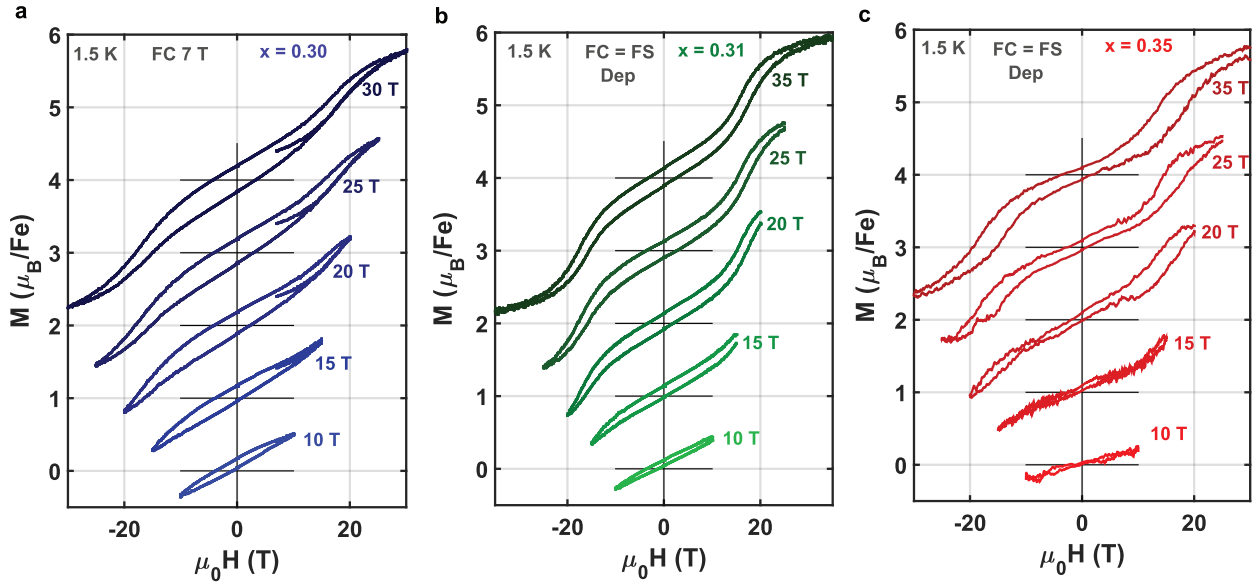
Figure 3.15: Magnetization versus high magnetic field loops measured in various sweep ranges. Each loop is offset on the y-axis by 1 μ_B/Fe. The magnetic field was applied along the c-axis of the samples. (a) Loops performed on the $x = 0.30$ intercalation at 1.5 K after field cooling in a 7 T magnetic field and sweeping to various fields. (b),(c) Loops performed on the $x = 0.31$ and $x = 0.35$ intercalations at 1.5 K after field cooling in various fields subsequently sweeping the magnetic field to the same values (i.e. FC = FS).
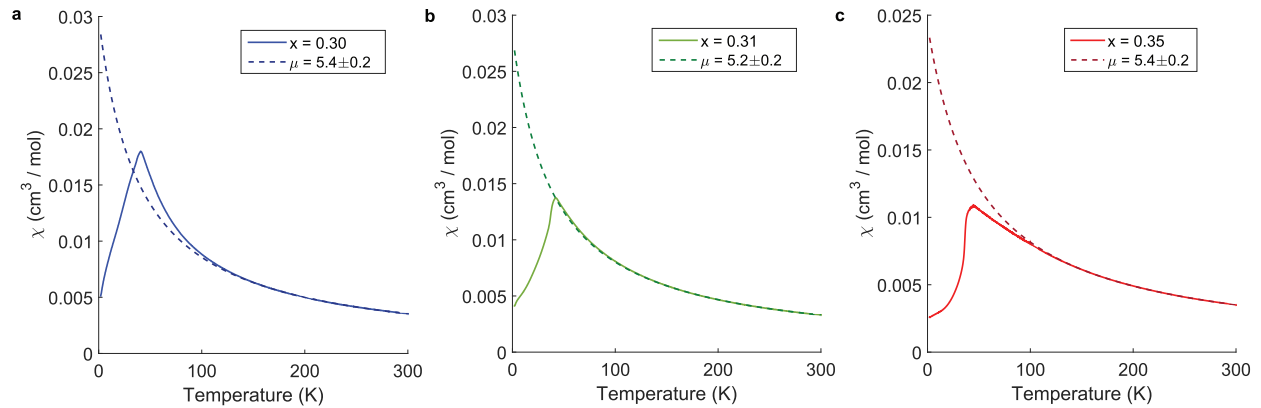
Figure 3.16: χ_{mol} versus temperature for x = 0.30 (a), 0.31 (b) and 0.35 (c) intercalation values. The data above $\simeq 150K$ was fitted to the Curie-Weiss model $\chi = \frac{C}{T - \Theta_{CW}}$ (dashed lines). From these fits, we extracted the effective moments (μ_{eff}) and Curie temperatures given in Table 3.2.
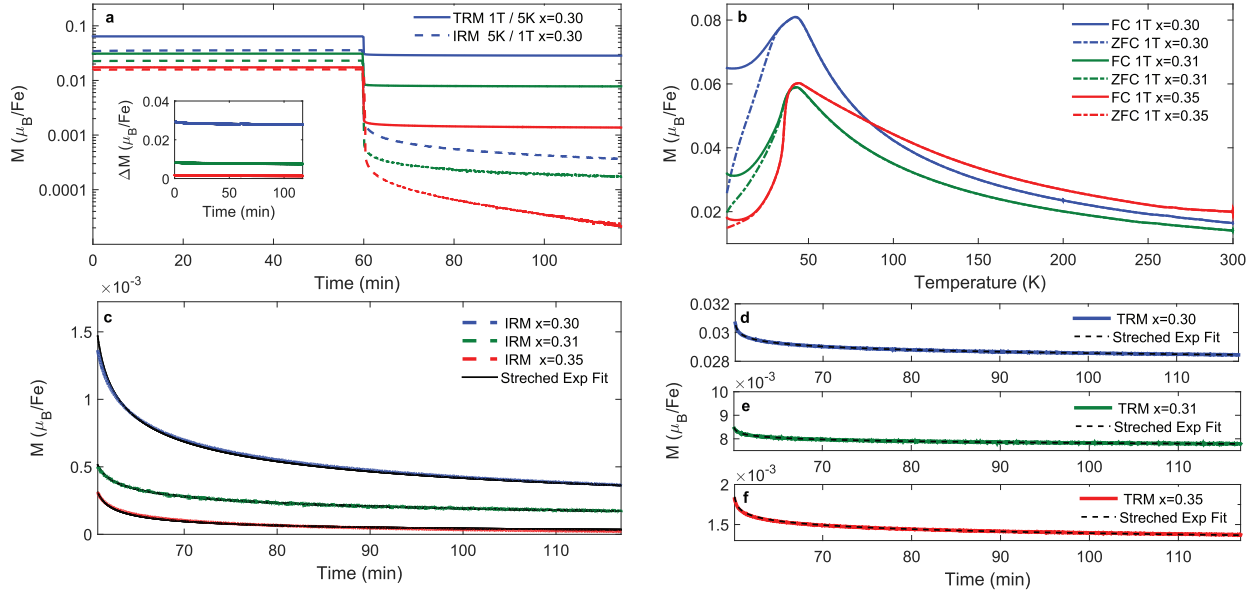
Figure 3.17: Intercalation dependent relaxation measurements. (a) A full IRM (dashed lines) and TRM (full lines) measurement sequence is plotted. The IRM curves were obtained by ZFC to 5 k, applying a magnetic field of 1 T for 60 min, removing this field and finally waiting for 60 min. The TRM curves were obtained by FC in a 1 T magnetic field to 5 K, waiting 60 min, removing this field and finally waiting for 60 min. The inset shows the calculated Δ M = TRM - IRM, emphasizing the induced FC moment is highly robust compared to the weak relaxation effect. (b) FC and ZFC magnetization versus temperature curves for all intercalations measured at 1 T. The difference between the FC and ZFC curves is comparable to the staring point of the relaxation sequence. (c)-(f) Zoom in on the IRM / TRM relaxation measurements and their corresponding fits respectively. The fits were performed using a typical stretched exponential decay function. From these fits, we extract the relaxation times for each intercalation given in Table 3.3.
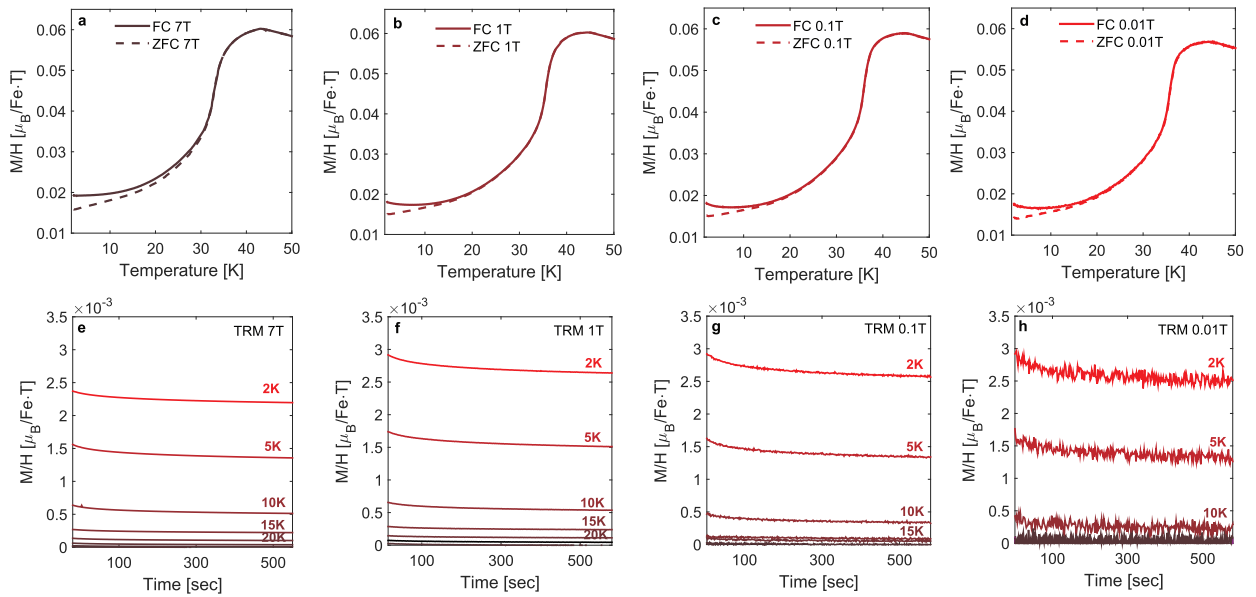
Figure 3.18: C-axis magnetization versus temperature and TRM measurements of the x = 0.35 sample. (a)-(d) Magnetization versus temperature scans FC (solid lines) and ZFC (dashed lines) in fields of 7 T, 1 T, 0.1 T, and 0.01 T. The y-axis is scaled by the magnetic field applied. (e)-(h) TRM scans (described in the relaxation analysis section) at different temperatures after cooling in fields of 7T, 1 T, 0.1 T, and 0.01 T. The y-axis is scaled by the magnetic field the sample was cooling in.
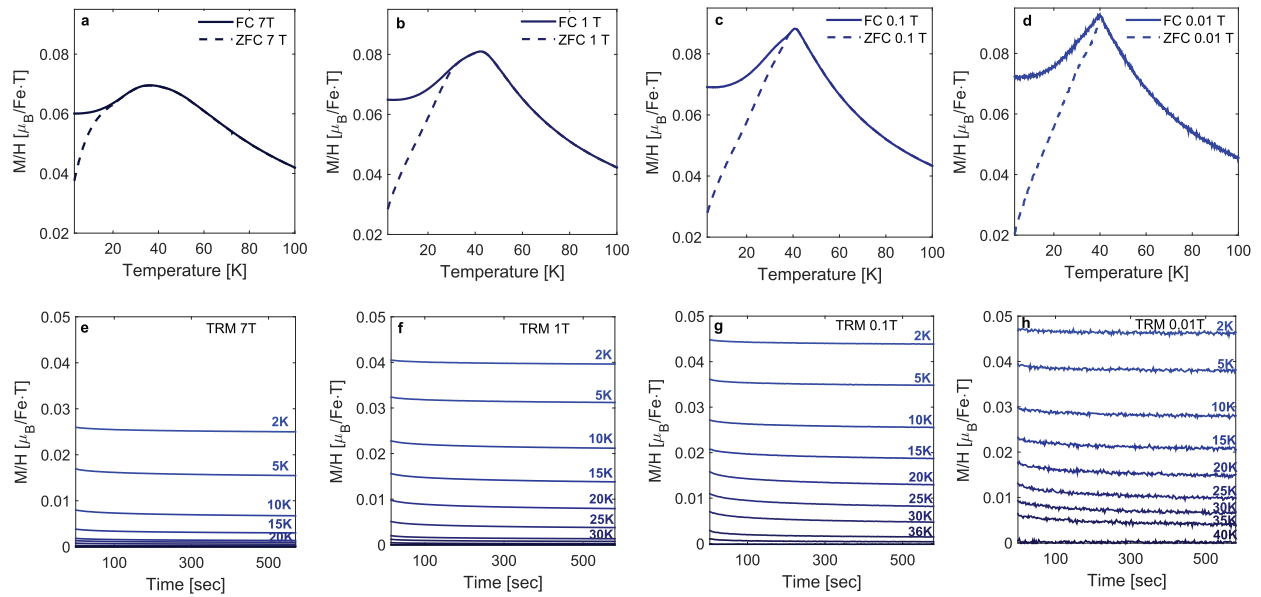
Figure 3.19: C-axis magnetization versus temperature and TRM measurements of the x = 0.30 sample. (a)-(d) Magnetization versus temperature scans FC (solid lines) and ZFC (dashed lines) in fields of 7 T, 1 T, 0.1 T, and 0.01 T. The y-axis is scaled by the magnetic field applied. (e)-(h) TRM scans (described in the relaxation analysis section) at different temperatures after cooling in fields of 7T, 1 T, 0.1 T, and 0.01 T. The y-axis is scaled by the magnetic field the sample was cooling in.
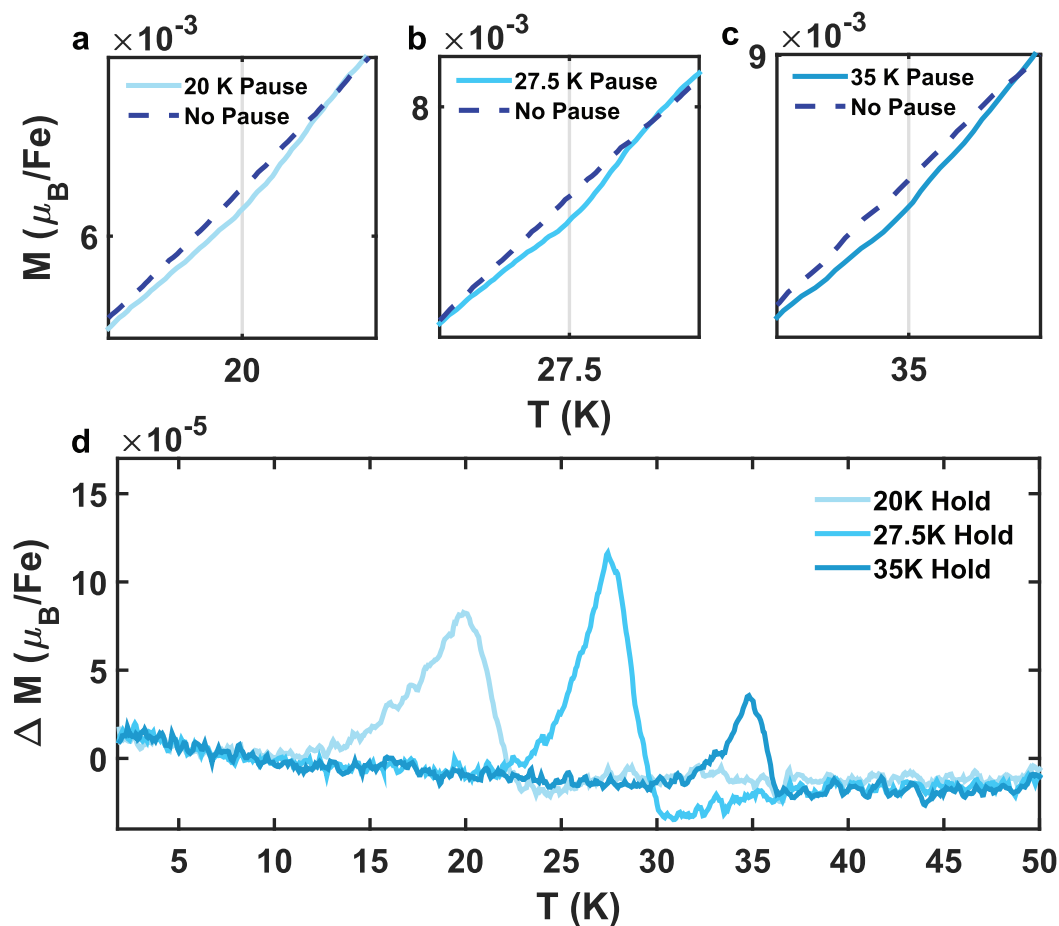
Figure 3.20: Aging memory effect measured on a x = 0.30 sample, using an applied magnetic field of 1000 Oe. All measurements were done after ZFC the sample. At each cool-down we have waited for one hour at a different temperature [No Pause (dashed line), 20K (a), 27.5K (b) and 35K (c)]. Distinct variations near the waiting temperatures appear in the magnetization measurements. (d) The calculated Δ M = ZFC(No Pause) - ZFC(Pause) is plotted with respect to temperature for each waiting point. This reflects the effective change of the measured magnetization correlated to the paused temperatures.
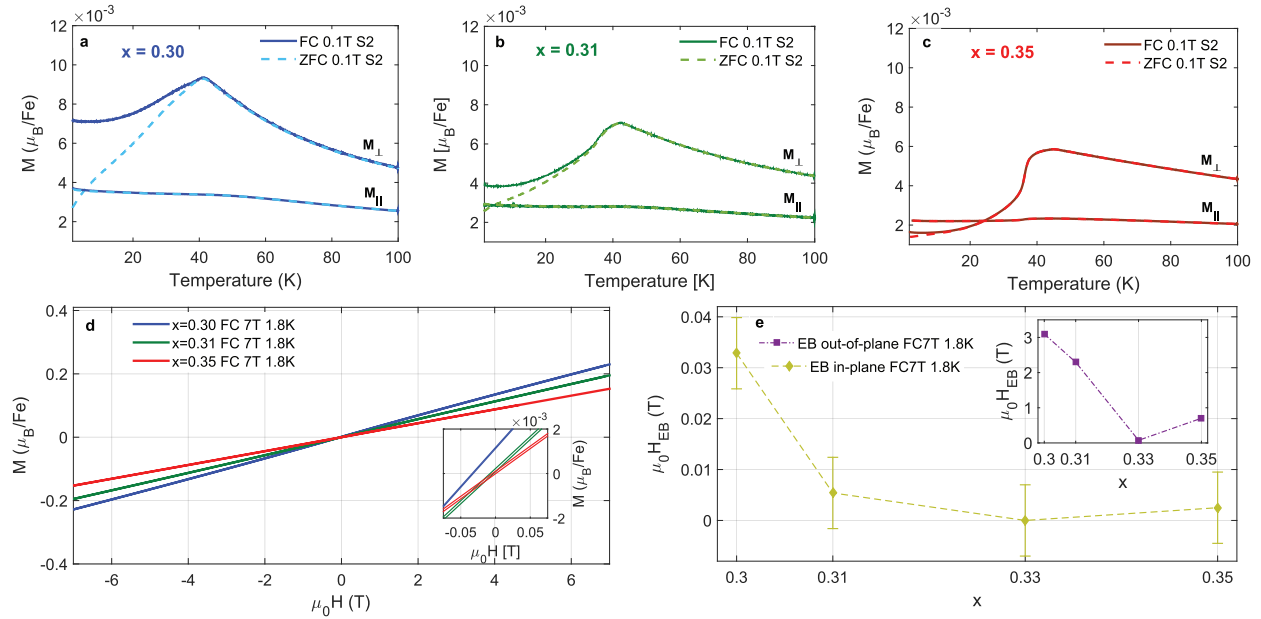
Figure 3.21: In-plane magnetization measurements. (a)-(c) Magnetization versus temperature scans for both out of plane (c-axis) and in-plane (ab plane) directions. FC (0.1 T) and ZFC curves, measured at 0.1 T, are plotted for x = 0.30, x = 0.31 and x = 0.35 intercalations respectively. The known anisotropy and easy axis of the magnetic phase is clearly observed. (d) Magnetization versus in-plane magnetic field scans measured at 1.8 K for all three intercalations. The samples were initially FC with a magnetic field of 7 T. The inset focuses on the exchange bias established in the samples. (e) The calculated exchange bias is plotted with respect to the intercalation value (x). Repeatable measurements have been performed in order to verify this result. The error bars have been established by the variation of these measurements. The exchange bias observed is increasing as the intercalated iron departure $x = \frac{1}{3}$. Additionally, the exchange bias is two orders of magnitude smaller than for the out of plane one. The inset demonstrates the exchange bias intercalation dependence for magnetic field applied in the out-of-plane direction (calculated from Figure 2b in the main text and Figure 3.22).
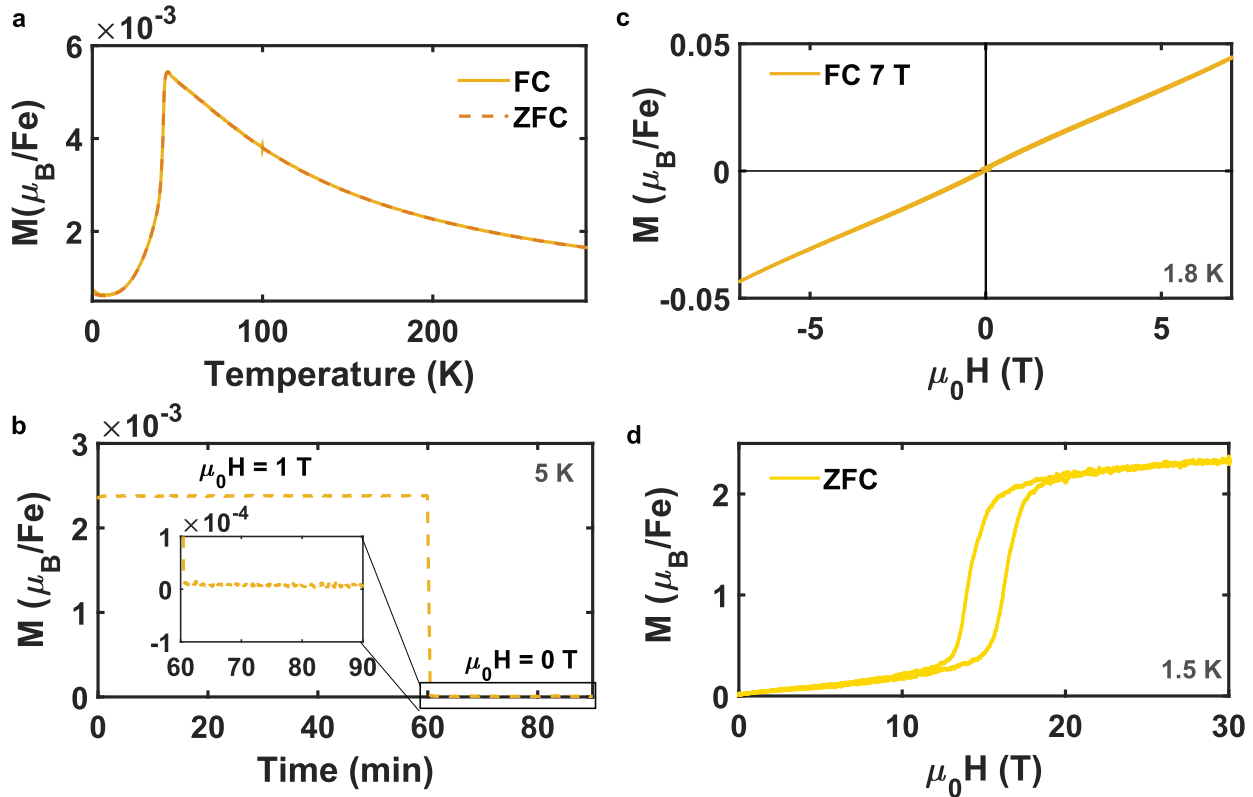
Figure 3.22: Out-of-plane Magnetic Characterization of $Fe_{0.33}NbS_2$. (a) 0.1 T magnetization versus temperature curves: both the FC (solid line) and ZFC (dashed line) curves are shown. (b) IRM relaxation measurement obtained by ZFC to 5 k, applying a magnetic field of 1 T for 60 min, removing this field and finally waiting for 30 min. Inset: zoom-in on the measurement after the magnetic field is turned off. No relaxation is present. (c) Low magnetic field sweep measured after cooling the sample in a 7 T field from above the AFM transition temperature. The magnetic field was swept from 7 T to -7 T back to 7 T. There is no sign of hysteresis about zero field. (d) High magnetic field sweep measured after ZFC the sample. The magnetic field was swept from 0 T to 30 T and back to 0 T. Hysteresis of the metamagnetic transition is present with no sign of zero-field hysteresis. [1]
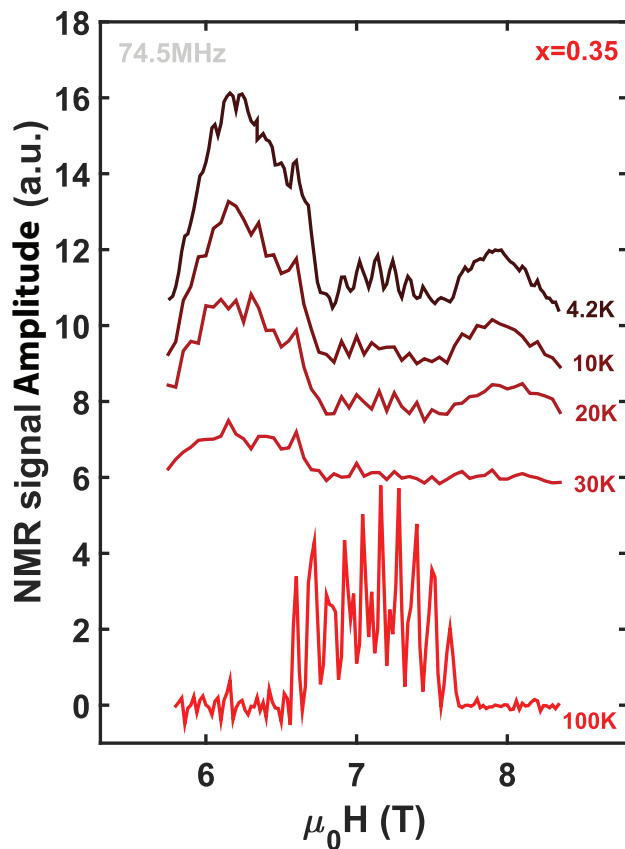
Figure 3.23: Field Swept NMR data for $x = 0.35$ intercalation. Field-swept NMR spectra performed at 74.5 MHz on the $x = 0.35$ intercalation for several temperatures between 100 K to 4.2 K. The magnetic field was applied along the c-axis of the sample. All field sweeps were performed after field cooling the sample. The presented data is offset on the y-axis for clarity. The quadrupolar coupling was extracted to be 1.25 MHz.

Chapter 4

Switching

"I remember cold!
"I remember hot!
"I remember something that I think I just forgot."

– Lisa Lambert & Greg Morrison
The Drowsy Chaperone

4.1   Introduction

In addition to the exchange bias and other history-dependent effects described in the previous chapter, there is a more unusual memory behavior in Fe_xNbS_2 whose relationship to the spin glass phase is less clear. First observed in Reference [68], the anisotropy of the conductance in Fe_xNbS_2 can be altered via the application of brief electrical current pulses. This ability lends itself to applications such as magnetic RAM and spin valves. While present-day technologies largely leverage the charge degrees of freedom of electrons, there has been an increasing focus on spin as research in magnetic memory shows more and more promise to surpass its charge-based counterpart. The current generation of magnetic memory in development utilizes an antiferromagnetic layer in order to pin a neighboring ferromagnet in place, but it is centered around the reorientation of a ferromagnetic layer. Magnetic memory based instead on the manipulation of an antiferromagnetic component has the potential to be faster, more dense, more energy-efficient, and more stable, due to the faster dynamics, lack of stray fields, and lower susceptibility to external fields of antiferromagnets compared to ferromagnets [69–71]. This has been difficult to realize in a physical system, however, for some of the same reasons that it is desirable: being insensitive to external fields and producing little to no net fields themselves, antiferromagnets are difficult to manipulate and it is not trivial to read signatures of any manipulations that might occur.

In recent years, there has been progress in the study of methods and antiferromagnetic materials that are able to overcome these challenges. Leading the charge were CuMnAs and Mn2Au, two antiferromagnets that were shown to have resistance changes in response to ap-

plied current pulses [70,71]. The proposed mechanism for this response was this: the applied current pulse becomes locally spin-polarized around the antiferromagentic sublattices, applying a torque to the sublattices that results in a collective rotation which reorients the Neel vector; the application of a perpendicular pulse results in a perpendicular orientation for the Neel vector [69–71]. The results are read out in the material's anisotropic magnetoresistance (AMR), discussed in more detail in Section 1.4.

4.2 Switching and symmetry

The local spin-polarization of the applied current in CuMnAs and Mn2Au is allowed because of the symmetry of these crystals. Specifically, they are inversion symmetric but their antiferromagnetic sublattices are not. This allows a local coupling between electron momentum and spin polarization via Rashba spin-orbit coupling, which is described by an energetic term of the form $H \propto (\vec{z} \times \vec{p}) \cdot \vec{\sigma}$, where $\vec{z}$ is the direction of broken inversion symmetry, $\vec{p}$ is proportional to the momentum, and $\vec{\sigma}$ is the Pauli matrix vector. Simply put, momentum is odd under inversion and spin is even, so this term is overall odd under inversion. Therefore, this coupling is only allowed when the system itself breaks inversion symmetry.

To explain this more pedagogically, let's first consider why a crystal that does not break inversion symmetry cannot induce a net spin polarization in a current that flows through it. We will start by assuming the opposite, that there is nonzero Rashba spin-orbit coupling which causes a current flowing through an inversion-symmetric crystal to result in a non-zero spin density. Let's say that the current flows in a direction $\hat{x}$, and that the induced spin polarization is in direction $\hat{x}'$. Applying inversion, the current direction is reversed, becoming $-\hat{x}$, while the crystal itself and the spin direction $\hat{x}'$ are both unchanged. Therefore, applying a current in either $\hat{x}$ or $-\hat{x}$ in this system will induce a spin polarization of $\hat{x}'$. If we apply currents of equal magnitudes in the directions $\hat{x}$ and $-\hat{x}$, they will cancel out to zero net current, while they cause spin polarizations in the same direction, and so cannot cancel out. We end up with zero charge current and nonzero spin polarization. This contradicts the initial assumption, that the spin polarization is coupled to the charge current, as we can now change the spin polarization by 'applying' appropriate equal-magnitude and opposite-direction charge currents, which is equivalent to applying no charge current. There is no relationship between the charge current applied and the resulting spin polarization. It follows that spin polarization in an inversion- symmetric system cannot be coupled to a charge current in this way. This is illustrated in Figure 4.1.

Returning to CuMnAs and Mn$_2$Au: in these systems, the crystal structure is inversion symmetric and therefore, by the above argument, the net spin polarization of an applied current must be zero. Their antiferromagnetic sublattices, however, do break inversion symmetry - so it was proposed that each sublattice experiences a locally polarized current, with an opposite polarization to that seen by the other sublattice.

Our system, Fe$_x$NbS$_2$, on the other hand, itself breaks inversion symmetry. This implies that the applied current can take on a net spin polarization, and apply torque to the local mo-
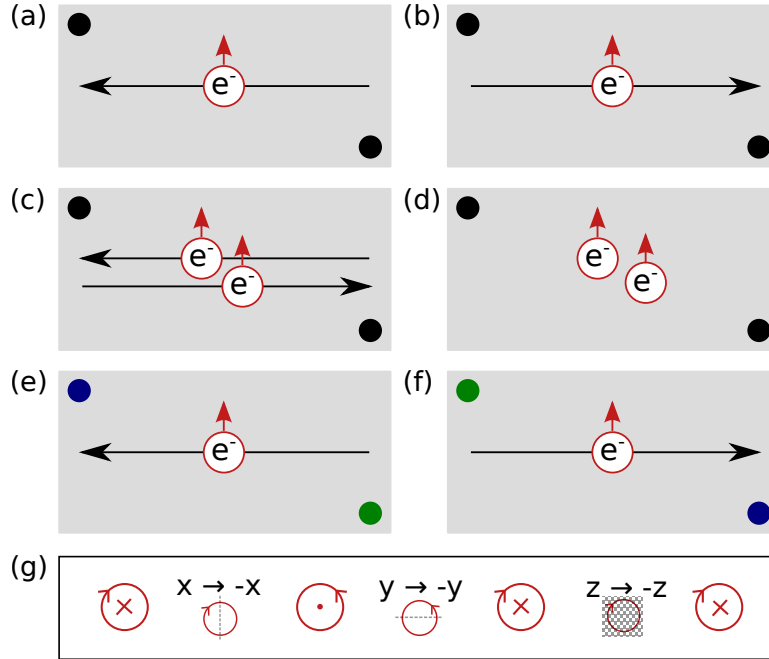
Figure 4.1: (a) Charge current flowing through an inversion symmetric system and associated spin density. Black dots are shown on the corners of the system to indicate that it is invariant under inversion. (b) The situation shown in (a), under inversion. The system is the same (indicated by the equivalence of the configuration of the dots on the corners), and the spin polarization is in the same direction, but the charge is now flowing in the opposite direction. (c) The situation in (a) combined with that in (b) - two charge currents, both leading to spin polarizations in the same direction, flowing in opposite directions. (d) Equivalent to situation (c), in which the charge currents cancel but the spin-polarization does not. This contradicts the initial assumption, that the spin-polarization is coupled to an applied charge current. (e) Charge current and associated spin density in a system that is not inversion symmetric. Dots of different colors are shown on the corners of the system so that it can be seen that the system itself is different under inversion. (f) The situation shown in (e), under inversion. The current direction has reversed while the spin-polarization has not, but no contradiction is reached because the system itself has changed (indicated by the reversed colors of the dots on the corners of the system). (g) Schematically, a spin under inversion. Without loss of generality, the spin starts pointing along z. Reversing the x coordinate changes the direction of the spin, and reversing the y coordinate changes it back. Reversing the z coordinate does not further alter the spin, so it is unchanged under inversion.

ments in that way. Our understanding of the switching mechanism in Fe_xNbS_2 has evolved significantly, as will be outlined later in this chapter and in Chapter 6, but this discussion serves to provide the context in which switching in Fe_xNbS_2 was initially studied.

4.3 Switching response in iron-intercalated niobium disulfide

The setup of the switching measurements in Fe_xNbS_2 are as follows, with devices prepared as described in Section 4.4. Devices have two perpendicular bars for the application of current pulses, and two thinner bars 45° from each of the pulse bars to aid measurement. The measurement and pulse geometries can be found in Figure 4.2 (a-d) and (e), respectively. Figure 4.2 (f) shows a characteristic switching protocol: brief current pulses are sent in perpendicular directions, and the response variable of interest is the resistance between pulses, as measured in one of the geometries shown in (a-d). Between experiments, those currents typically range from 10^4 to $10^5 A/cm^2$, and the durations range from $0.01ms$ and $100ms$. The time between pulses is generally either 15 or 30 seconds for a given experiment. The bottom panel of Figure 4.2 (f) shows the shape of a typical switching response, with the resistance increasing or decreasing upon the application of perpendicular pulses in a repeatable and stable way. Details such as the amplitude of the response and the sign of the response (whether a given pulse results in a high or a low resistance state) depend primarily on the pulse parameters, the temperature, and the level of iron content in the device, as will be discussed in the following sections.

Current density dependence

The dependence of the switching response on the pulse current density is non-monotonic, as was initially reported in Reference [8] and can be seen in Figure 4.3 (a). Once the switching response turns on at a high enough current density, its amplitude quickly reaches a maximum and then decreases before leveling off with higher and higher current densities. In some samples, the maximum and stable region are preceded by a sign change in the switching response. The non-monotonicity extends as well to the pulse duration dependence of the switching response, shown together with the pulse density dependence in Figure 4.3 (b). Note that the pulse duration is included on a log scale, and that a simple argument based on the total energy being imparted into the system by Joule heating is not sufficient to explain the relationship between pulse density, pulse duration, and maximum switching response. This shape of the response under varying pulse parameters is surprising in the context of our initial understanding of the switching behavior and its drivers. More surprising is the response's dependence on iron intercalation level, described in the next section.
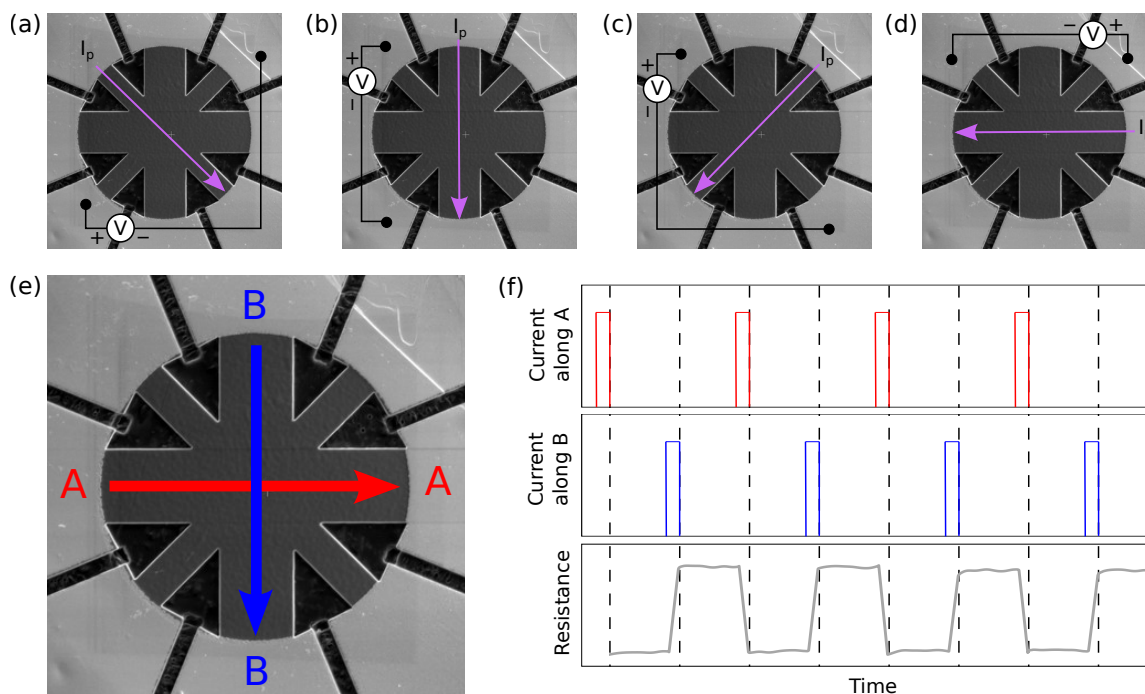
Figure 4.2: (a-d) Measurement geometries for a typical switching device. I_p and its associated arrow indicate the direction of the AC probe current. The probe current is applied and voltage is measured concurrently with the application of current pulses, but measurement and switching geometries are shown separately here for clarity. (e) Geometry for applying switching pulses. Perpendicular pulses are applied within the plane of the crystal. (f) Typical switching protocol and response. For a single protocol, as shown schematically here, the same current amplitude, current duration, and time between pulses is used for all pulses. Top panel: Current along A as a function of time. Middle panel: Current along B as a function of time. Bottom panel: Characteristic response. This particular dataset was taken in the measurement geometry shown in (c), but it is representative of the response in any of the geometries. Because the current pulses cause large spikes in the measured voltage during their duration, a hampel filter is applied to the data to show only the resistance between current pulses.
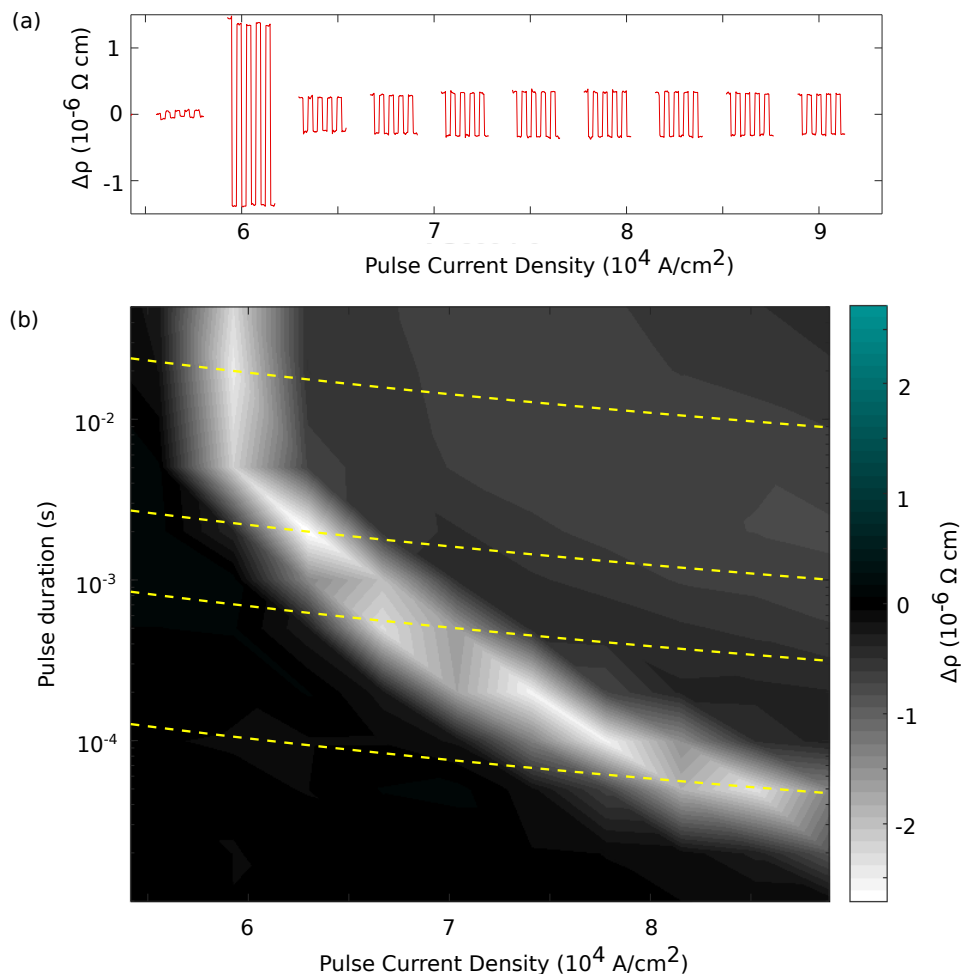
Figure 4.3: Representative pulse parameter dependence of Fe_xNbS_2. Shown here are data taken at 2K on a device with $x = 0.35$. (a) Pulse current density dependence of the switching response. There is a sharp maximum in the amplitude of the response right where the switching begins, and thereafter the amplitude is stable with increasing current density. (b) Pulse current density and duration dependence of the switching response. The intensity indicates the amplitude of the switching response from peak-to-peak. A negative value is assigned to behaviors with high resistance resulting from A pulses, and a positive value to those with low resistance from A pulses. Dashed lines indicate current density and durations that correspond to equal energy from Joule heating.

Temperature dependence

The switching response in $Fe_x NbS_2$ is strongest at 2K, and disappears above the magnetic ordering temperature, as shown in Reference [72]. Considering the full pulse density dependence (as in Figure 4.4), it can be seen that this trend goes beyond a shifting of the switching peak; the maximum attainable switching amplitude decreases with increasing temperature, and switching is no longer achievable when the material is no longer ordered.

Intercalation dependence

While our initial understanding of the switching in $Fe_x NbS_2$ did not immediately lend itself to an explanation of the pulse current dependence we observed, it is shown to be more directly insufficient by the differences in our measurements of $x > 1/3$ and $x < 1/3$ samples. This difference was intially reported in Reference [72], and is shown in Figure 4.5. The two measurements shown here were taken on devices with different levels of iron intercalation, but the measurements were otherwise identical in every relevant way: the pulse geometry, the measurement geometry (that shown in Figure 4.2 (c)), and the current directions relative to the crystal axes were all the same between these two measurements. They were also both taken at 2K, with a pulse current density of about $15 \times 10^4 A/cm^2$ and duration of about 10ms, well in the stable-switching regime. Most notably, while the devices have comparable magnitudes of switching response, they have opposite signs; while an A pulse brings the $x < 1/3$ sample to a low resistance state, it brings the $x > 1/3$ sample to a high resistance state. Measurements of more samples with a variety of iron contents reveal a smooth dependence of the switching amplitude on x, with zero-crossing somewhere between $x = 0.33$ and $x = 0.34$, depending on the pulse parameters [72].

Conclusions

As will be discussed further in Chapter 6, the temperature dependence of the switching signal, together with this sign change, strongly supports the magnetic nature of the switching. The pulse current dependence of the switching response is surprising in the specific context of a mechanism in which the Neel vector is rotated by a spin polarized current. The intercalation dependence is yet more difficult to reconcile with this sort of explanation, and points to the importance of some qualitative difference resulting from different intercalation levels, or to competing orders. One major difference between the off- and on-stoichiometry samples is the presence (or absence) of a spin glass, as discussed in depth in Chapter 3. The spin glass could contribute to the strength and stability of the switching response by enhancing the anisotropy of conduction electron scattering, by changing the nature of defects and therefore domain walls, and by locally stiffening the AFM order parameter [72]. The different signs above and below perfect stoichiometry point to an inherent difference between the spin glass created by the two kinds of disorder (excess and deficient iron), or to a difference between
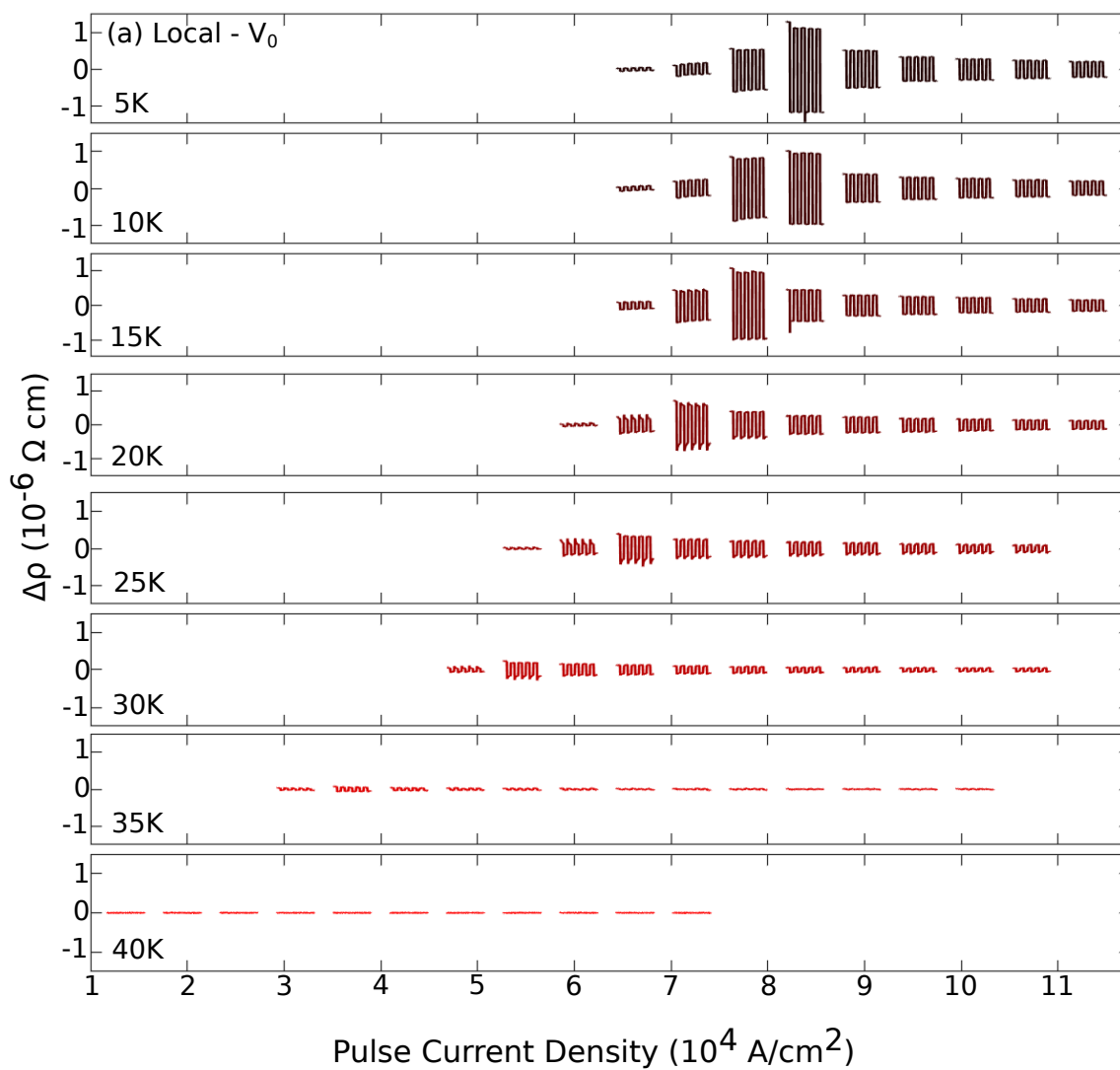
Figure 4.4: Temperature dependence of switching response in $Fe_{0.35}NbS_2$. Each panel shows the switching as a function of pulse current density; all pulses have a duration of 10ms. From top to bottom, the response is shown at temperatures increasing from 5K in increments of 5K to 40K. This figure was initially published in the supplement of Reference [2], and is discussed in more detail in Chapter 6.
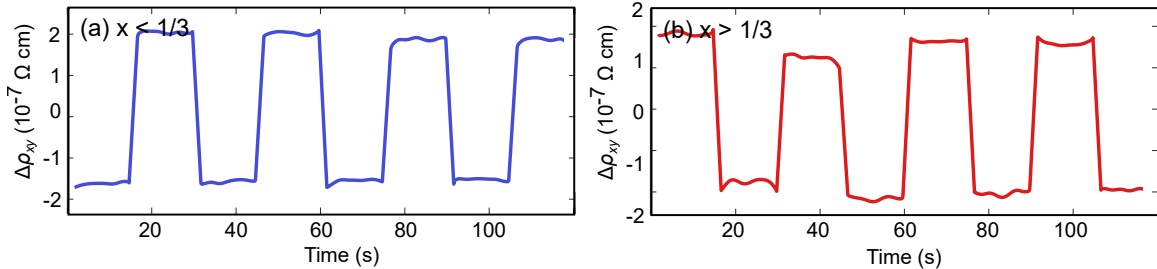
Figure 4.5: Switching responses in two measurements nearly identical except for the iron content of the devices. Both cases use a pulse geometry and protocol like that shown in Figure 4.2 (e) and (f), and measurement geometry like that shown in Figure 4.2 (c). They are additionally taken with the same pulse parameters and at the same temperature. (a) Switching response in $x < 1/3$ device. (b) Switching response in $x > 1/3$ device.

the nature of the AFM order above and below $x = 1/3$. Chapter 5 will present and discuss data taken to explore these possibilities.

4.4 Appendix I: Sample preparation

Devices for switching measurements are prepared as described in the following sections.

Exfoliating the crystals

First, crystals of appropriate dimensions are obtained. These dimensions vary depending on the exact kind of device being made, but generally are determined by (1) what is feasible to pattern in the FIB, and (2) what is needed for the measurement being planned. As a general rule of thumb, crystals between 0.5 and $5\mu m$ thick and between 50 and $300\mu m$ across are optimal regarding point (1), usually leading to a fabrication time in the FIB between 1 and 6 hours depending on details of the mounting, the device design, and the FIB operator. Larger samples are possible to fabricate with more time, with increased tolerance for damage from the FIB, or with more flexibility in designing the FIB pattern. For switching measurements, (2) usually translates to aiming for samples between 0.5 and $2\mu m$ thick, so that switching current densities are achievable with relatively safe and attainable absolute currents.

If luck is on one's side, crystals this small can be found by dipping a small, broken wooden stick into the batch of crystals as-grown, and finding the smallest crystals that stick to the wood via static electricity. Often, however, crystals of the desired dimensions are not readily available. In this case, larger samples can be cleaved or exfoliated.

Exfoliation of TMDs and intercalated TMDs for the purpose of FIB fabrication is best done with a low-residue tape, such as Nitto's PVC film coated with acrylic-based adhesive (commonly known as blue tape). Sandwich crystals between two layers of tape (adhesive sides

in), and pull the sides apart rapidly. Better results can be obtained by pressing the tape well in order to minimize air bubbles, either with hands or with tweezers. Flakes can then be transferred to a substrate directly from the tape, or they can be carefully pulled from the tape with the scalpel. The latter approach has the benefits of enabling different mounting media and of minimizing extra flakes on the substrate, that may need to be removed or cut through with the FIB in order to ensure good separation between electrical contacts.

Pure TMDs are generally easier to exfoliate than most materials, because their layers are held together by van der Waals forces. The process can still be challenging, however, and there are differences between specific TMDs in terms of both the level of ease and the nature of the challenges. One difficulty can be the fragility of the crystals, especially the ease with which they can crumple both before and after being exfoliated. To mitigate this, it is best to avoid handling the crystals with tweezers except as an auxiliary tool; the crystals should be lifted on top of a scalpel blade or stuck to a wooden stick with static electricity rather than squeezed between tweezer teeth. This is a good rule of thumb when working with any crystals small enough to cut with the FIB, although the exact kind of damage it protects against varies slightly.

Intercalated TMDs are often more difficult to exfoliate than their unintercalated counterparts, because the intercalant bonds to the chalcogens in the TMD layers. In cases where exfoliation with tape alone proves unfruitful, it can be helpful to first slice the crystal with a scalpel.

Mounting the crystal

Once a crystal of suitable dimensions is obtained, it can be mounted either on an adhesive or directly on a substrate. When mounting directly on a substrate, the crystal needs to be small enough that it can stick to the substrate with van der Waals forces, and ideally thin enough that platinum (or some other conductive element) can easily be used to connect it electrically in the FIB. This generally corresponds to a thickness of $1\mu m$ or less. When working with larger crystals, or when the additional FIB time requirement of platinum deposition is unfeasible, the samples can instead be mounted on an adhesive. TorrSeal epoxy resin is a good choice of adhesive for switching devices, holding up well under vacuum and down to cryogenic temperatures. After placing a blob of TorrSeal on the substrate, the crystal is picked up on the underside of a wooden stick and, in order to avoid submerging the crystal entirely in the TorrSeal, the crystal is brought close to the surface of the TorrSeal and kept there until the natural shaking of the experimenter's hand deposits it on TorrSeal. If necessary, the TorrSeal is gently disturbed with the wooden stick so that the surface of the crystal is flush with the surface of the TorrSeal, without any TorrSeal on top of the crystal. The substrate with TorrSeal and the crystal is then cured for 30 minutes at 120 degrees Celcius, or for 1 hour at 80 degrees Celcius. If these temperatures are not optimal for the sample to be subjected to, Devcon 5 Minute Epoxy can alternatively be used. It cures at room temperature and does so very quickly, as the name suggests. This makes the mounting process a bit more challenging, and Devcon additionally has been found empirically to lead
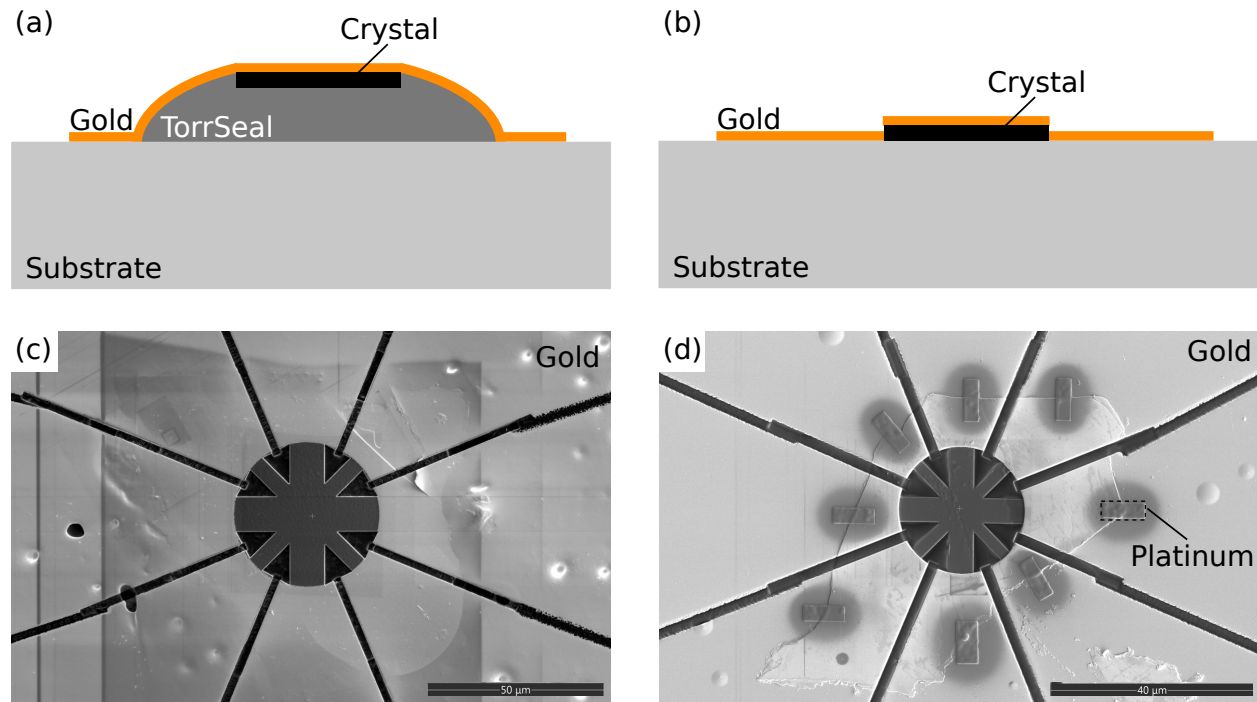
Figure 4.6: (a) Schematic of pre-FIB mounting on TorrSeal. (b) Schematic of pre-FIB mounting directly on a substrate. (c) Example of post-FIB device on TorrSeal. (d) Example of post-FIB device directly on a substrate.

to a greater rate of devices breaking.

Once the sample is mounted and any adhesives have been cured, gold is deposited onto the substrate. This is done after creating and applying a mask made of Kapton tape, so that gold is deposited only on a square of about $1-2mm^2$ around the crystal. See Figure 4.6 (a) and (c). After deposition, the substrate is mounted on an SEM stub with conductive adhesive, which is additionally used to ground the gold to the SEM stub.

Patterning the crystal

The sample is patterned using an SEM/FIB dualbeam system. See Figure 4.6 (c) and (d) for examples of completed devices. First, if the sample is directly on a substrate rather than mounted on adhesive, platinum is deposited at the edges of the crystal as shown in Figure 4.6 (d) in order to ensure good electrical contact between the sample and the gold on the substrate. If the crystal is thicker than about $0.5\mu m$, platinum is first deposited just off the edge of the crystal onto the substrate – this softens the step from crystal to substrate that the deposited platinum will need to traverse. Once the crystal is well-connected, gold is removed from what will be the active area of the device using a beam current of $1.6nA$. This

step can precede the platinum deposition if needed, but platinum overspray onto the active area of the device then needs to be checked for and rectified if found. The main pattern of the device (for typical switching devices, this is comprised of the triangular regions shown in Figure 4.6 (c) and (d)) is then cut using the same or a slightly higher beam current, depending on the size of the pattern and crystal. Cuts are made from the main pattern to just past the edges of the crystal. Finally, with a lower magnification and a higher beam current, these cuts are continued to the edge of the gold.

Chapter 5

Half-Magnetization Plateau

"Happy families are all alike; every unhappy family is unhappy in its own way."
– Leo Trotsky

Materials in this chapter were previously published in

- Shannon C. Haley, et al., *Half-magnetization plateau and the origin of threefold symmetry breaking in an electrically switchable triangular antiferromagnet*, Physical Review Research **2**, 043020 (2020).

5.1 Introduction

As was seen in Chapter 4, the switching behavior changes signs as we change the amount of iron contained between the niobium disulfide layers. This presents two possibilities: (1) the antiferromagnetic order is manipulated in the same way in both cases, but the resistance anisotropy for a given state changes, or (2) the antiferromagnetic order is manipulated differently in the two cases. The second possibility could arise from differences in the 'write-in' mechanism, or from differences in the antiferromagnetic order itself. It is difficult, however, to measure qualitative differences between these samples, because the presence of disorder smooths out features and obfuscates what might otherwise be obvious signatures.

In broad strokes, their behaviors as measured by basic characterization techniques are the same. As a function of temperature, an AFM transition is seen a bit below $40K$ in both magnetization and resistance. There is a splitting of the field-cooled and zero-field-cooled magnetization curves, indicative of the presence of a spin glass. As a function of magnetic fields up to 7T, there is some slight hysteresis and overall a very small magnetic susceptibility. Heat capacity shows two transitions in temperature at zero field, which split apart with applied field.

In high magnetic fields, however, some differences do stand out; see the $35T$ DC field measurements in Chapter 3. And, as will be seen in the present chapter, there are differences as well when measuring in $60T$ pulsed magnetic fields. The most important guiding insight

into the switching behavior that comes from these pulsed field measurements is not, however, from measurements of the over- and under-intercalated samples, but of the on-stoichiometry $Fe_{1/3}NbS_2$. From these measurements, we were able to:

1. Track the edges of the coexisting low-field AFM phases,

2. Determine the degree of in-plane canting of the spins,

3. Identify the dominant interactions in our system, and

4. Identify a previously-unknown high-field phase

We were able to gain some insight into the second and third points listed here based on our observations of magnetic susceptibility as a function of temperature in low field, shown in Fig. 5.1(a). First, the drop in the susceptibility below about 45K indicates, as has been noted earlier, that the interactions between the spins are predominantly antiferromagnetic. Second, comparing the magnetic response with the magnetic field pointing in-plane and that with the field pointing along the c-axis reveals a marked magnetic anisotropy. There is a significant preference of the spins to point along the c-axis, resulting in a higher susceptibility in that direction in the paramagnetic regime. To quantify these observations a bit more, we followed Ref. [73] to relate the magneto-crystalline anisotropy D to the in- and out-of-plane Curie-Weiss temperatures. The temperatures were found from the fits in Fig. 5.1(a) to be -110K and -26K, respectively; this analysis yields $D \approx 1$meV. While Ref. [74] gives slightly lower Curie-Weiss temperatures (-135K and -40K), these values give a virtually unchanged estimate of D, which is proportional to their difference.

The first point is partially revealed by our heat capacity data, Fig. 5.1(b), which shows two transitions as a function of temperature which split further and further apart with an increasing applied magnetic field. What is not clear from this data is whether these transitions will continue to split apart, and what kind of magnetic behavior we can expect from the phases they delineate.

5.2   Measurement set-up

The magnetization of iron-intercalated niobium disulfide was measured under applied fields up to 60T at the National High Magnetic Field Laboratory at Los Alamos National Laboratory. The measurement apparatus takes advantage of the high rate of change in the magnetic field generated by a pulsed magnet by measuring the change in flux through coils of wire during the pulse. The current induced in the coils is proportional to the time derivative of the magnetization and magnetic field together:

$$I \propto \frac{dB}{dt} = \frac{dM}{dt} + \frac{dH}{dt} \tag{5.1}$$
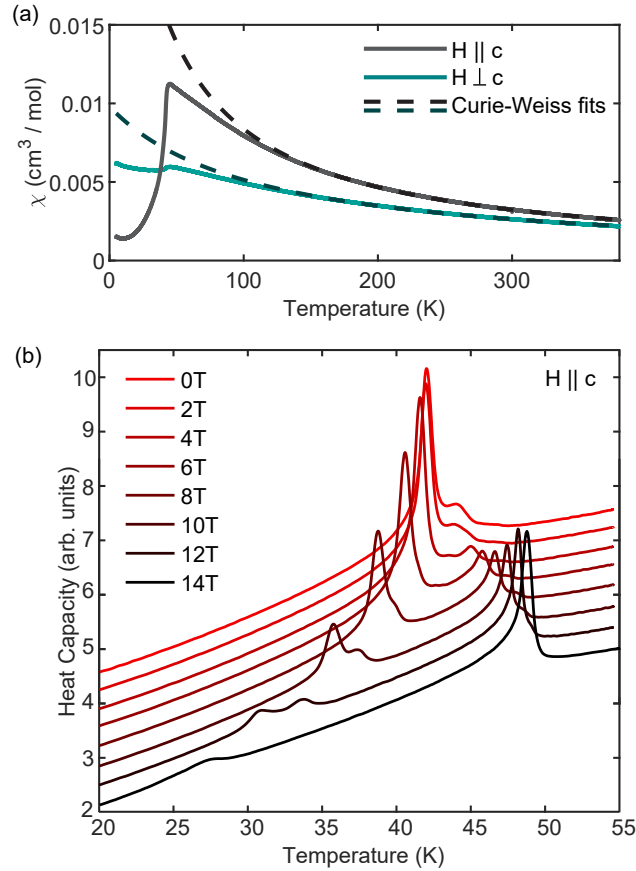
Figure 5.1: (a) Curie-Weiss fits of both out of plane ($H \parallel c$) and in plane ($H \perp c$) susceptibility. (b) Heat capacity measurements show two transitions, which split with the application of field parallel to the c-axis. Curves are offset to enhance visibility.

The change in applied magnetic field is then separated out to isolate the time derivative of the magnetization of the sample, which is integrated and correlated to the applied field. Because the measurement of magnetization is, ultimately, an integral, any zero-field offset is not detected by this method. Additionally, due to variations in the sample placement and coil windings, the determined values are proportional to the magnetization of the sample but do not directly provide the actual values. These are determined by scaling the magnetization measured in pulsed field to curves taken at the same temperatures in low fields.

A stack of about 30 co-aligned crystals of iron-intercalated niobium disulfide was assembled to ensure there was sufficient mass to allow a clear readout. The crystals were packed in an ampoule and held in place with vacuum grease.

5.3 Measured behavior

Measurements of the magnetic susceptibility as a function of temperature in low applied fields show AFM behavior below a transition near 45K (Fig. 5.1 (a)). Fitting to the paramagnetic regime, the Curie-Weiss law yields an estimate of $5\mu_B/Fe$ for the effective moment of the material, a quantity which is slightly higher than the expected moment at saturation. This is in agreement with the values found in the literature, which predominantly range from 4.3 to $5\mu_B/Fe$ [74–78], although there is one report as high as $6.3\mu_B/Fe$ [79]. Heat capacity measurements resolve two clear transitions at zero field (Fig. 5.1 (b)). With the application of field, these transitions move apart from each other in temperature. The lower temperature transition has a further splitting at higher fields, indicating the presence of an additional intermediate phase.

High field measurements further elucidate the nature of the phase transitions. Measurements at 0.6K and 20K of the magnetization as a function of applied field are shown in Fig. 5.2 (a). The full set of measurements, taken at temperatures ranging from 0.6K to 50K, is given in [3], and the phase boundaries determined in part from these measurements are shown in Fig. 5.3. These measurements were performed on a stack of about 30 co-aligned crystals, which were roughly 1mm in diameter and had an average thickness of 0.1mm.

There are three dominant phases at low temperature evident in the data: (I) the zero field phase characterized by a small magnetic moment, (II) the 'plateau' phase characterized by a nearly constant magnetic moment centered around half the estimated saturation moment, and (III) a high field phase which approaches the fully saturated moment. The final phase gets pushed above 60T at the lowest temperatures. An intermediate phase bridging the zero field and plateau phase has only a weak feature in the magnetization (see Ref. [3]).

The experimental phase diagram, Fig. 5.3, shows a non-monotonic dependence of the ordering temperature on applied field. This can be explained by the impact of an applied field on a reduced dimensional system [80]; as the field increases, both the order parameter and these fluctuations are suppressed. The latter effect increases in the transition temperature in low field, and the former brings down the transition temperature at higher fields. We also observe a second ordered phase, which is destroyed in that low field regime.

These measurements were confirmed in stacks and individual single crystals in pulsed and DC magnetic fields, see Ref. [3]. The latter was used to scale the former, because only relative changes could be recorded in our pulsed-field measurements. In addition, data on other compositions with $x = 0.339$ suggest changes in stoichiometry do not affect the field-dependent ground state, though they can shift the phase boundaries [3].

5.4 Background on Magnetization Plateaus

Plateaus in the magnetization of triangular-lattice antiferromagnets have been predicted and observed many times. In particular, a plateau at one-third of the fully saturated moment, corresponding to two spins pointing along the field direction for every one spin pointing

against it, is predicted from the simplest possible Hamiltonian for a frustrated triangular lattice AFM with an applied magnetic field:

$$H = J \sum_{NN} S_i \cdot S_j + \sum_i S_i \cdot H \qquad (5.2)$$

In this case, the one-third plateau is stabilized by quantum fluctuations in a phenomenon known as order-from-disorder [81].

One-half magnetization plateaux have been predicted in cases where next-nearest neighbor interactions are significant, and can again arise from quantum fluctuations [82, 83]. They have also been predicted classically, in cases where both next-nearest neighbor interactions and the single-ion anisotropy are significant [84]. The former considers a truly 2-dimensional triangular lattice, while the latter considers a layered system with ferromagnetic coupling between the layers, wherein the lattices are aligned with each other. Both of these pictures deviate a bit from our system, which has staggered layers of triangular lattices.

While they have been predicted, prior observations of half-magnetization plateaux are rare, and bear significant differences from the behavior seen in the present system - in particular, Fe_xNbS_2 shows a plateau which is stable over a large magnetic field range, and does not demonstrate the sort of cascade of plateaux that have been seen elsewhere [85, 86].

5.5   Extracted coefficients and microscopic insights

To understand the physical mechanism responsible for the magnetization plateaus, we study a minimal model motivated by our density functional theory calculations. In addition to the single-ion anisotropy D, we find that a model with nearest neighbor (NN) and next nearest neighbor (NNN) exchange couplings within a single plane of iron atoms, as well as NN and NNN couplings between adjacent planes, is sufficient to accurately reproduce an evolution of magnetic states in field that is consistent with our magnetization findings. We restrict our attention to the iron atoms and their localized d states, which form a lattice of S=2 spins, and consider a short-range Hamiltonian

$$\hat{H} = E_0 + 2J_1 \sum_{\langle i,j \rangle} \hat{S}_i \cdot \hat{S}_j + 2J_2 \sum_{\langle\langle i,j \rangle\rangle} \hat{S}_i \cdot \hat{S}_j + 2J_{1c} \sum_{\langle i_c,j_c \rangle} + 2J_{2c} \sum_{\langle\langle i_c,j_c \rangle\rangle} \hat{S}_i \cdot \hat{S}_j - \sum_i D(\hat{S}_i^z)^2, \ (5.3)$$

where J_1 and J_2 are the NN and NNN exchange couplings within a single Fe plane, J_{1c} and J_{2c} are the NN and NNN couplings between adjacent planes, and D is the magnetoanisotropy of Fe spins. E_0 encompasses any nonmagnetic contributions to the total energy. The exchange coupling sums are over all unique bonds. In a large neighborhood of relevant exchange coupling values, this model has three distinct phases at zero temperature as the magnetic field is varied. (1) An "AFM stripe" phase at a low field with a magnetic unit cell of four iron spins, two in each of two layers, with one spin in each layer pointing up along +c and one along -c in a stripe configuration. (2) A half-magnetization plateau at intermediate field

with a magnetic unit cell of eight iron spins, four in each of two layers, with one spin in each layer pointing along -c and three along +c. (3) A saturated phase at high field with a magnetic unit cell of two iron spins, one in each of two layers, with all pinned to point along +c, parallel to the applied field H. These phases are consistent with two close antecedents of this Hamiltonian, discussed in Refs. [82, 84]

Due to the spins being large ($S = 2$), we perform a classical analysis of Eq. 5.3. We search for the ground state of Eq. 5.3 using many different sized trial unit cells. While a fully 3D classical Monte-Carlo simulations would be more exhaustive, the present analysis is sufficient because high-field measurements of the nuclear magnetic resonance suggest that the plateau has a relatively simple spin texture [3]. We find that the magnetic unit cell for the ground state is always small over a very broad range of parameters J, D, and h, with no more than 8 Fe atoms. Intuitively, this small unit cell is consistent with the short-ranged nature of the dominant interactions.

The classical analysis shows there is a large range of couplings $(J_1, J_2, J_{1c}, J_{2c})$ which produce the three phases observed as a function of magnetic field when $D > 0$ is large. The key observation is that, for $J_1 > 0$ and $J_2/J_1 \ll 1$, there is a large region in the (J_{1c}, J_{2c}) parameter space that approximately reproduces the magnetization curves - the "stripy" AFM, UUUD, and UUUU are the only three ground states for a wide range of $J_{1c}/J_1 > -1$ and $J_{2c}/J_1 < 0$. In fact, the only 1/2-magnetization plateau without a UUUD structure between the two layers occurs for only a small region of parameter space. We may conclude that Eq. 5.3 qualitatively reproduces the observed transitions in the magnetization even without precise estimates for the coupling parameters.

We now quantitatively predict the critical magnetic fields for the transitions from the model Eq. 5.3. For large $D > 0$, the transition from the stripe phase to the plateau phase occurs when $h = 4(J_1 + J_{1c} + J_2)$ and the transition from the plateau phase to the saturated phase occurs when $h = 12(J_1 + J_{1c} + J_2)$. Quantitative analysis requires estimates of the parameters $(J_1, J_2, J_{1c}, J_{2c}, D)$, which we ascertain through a combination of experimental and numerical means. As was discussed in the introduction, we determined the magnetocrystalline anisotropy D from the in- and out-of-plane Curie-Weiss temperatures to be $D \approx 1$.

Our DFT calculations, performed with the Perdew-Burke-Ernzerhof (PBE) functional [87] and Hubbard U corrections [88], corroborate this picture. We note that the calculated D, being a highly local property, is sensitive to the Hubbard U used to approximately treat the localized Fe d electrons. This sensitivity has been documented for several Fe-based compounds in previous literature [89, 90]. However, the experimental estimate of D allows us to choose a U value that yields a similar anisotropy, and with which to compute the exchange constants in the minimal model. Using a Hubbard U of 0.3 in our PBE+U calculations at experimental lattice parameters (see supplement [3] for details), we obtain $D = 1.09$, with the easy axis along c, in very good agreement with experiment. Using six inequivalent magnetic collinear configurations with Fe spins along the c axis, we solve an overdetermined system of equations to determine the unknown couplings J. The values of all J as well as D are given in Table 5.1.

D	J_1	J_2	J_{1c}	J_{2c}
1.09	0.76	-0.006	0.39	-0.22

Table 5.1: PBE+U ($U = 0.3$) values of magneto-crystalline anisotropy D and NN and NNN interplanar and intraplanar couplings in Eq. 5.3. Units are per Fe atom. With the conventions used in Eq. 5.3 positive values for J represent AFM couplings, negative values are FM, and a positive value of D implies an easy-axis along c for the anisotropy.

As an experimental check, the Curie-Weiss temperatures can be related to the sum of the coupling constants corresponding to all of a given Fe atom's interactions, giving an estimate $\sum_i J_i = 6(J_1 + J_2 + J_{1c} + J_{2c}) \approx 1.1$ (assuming all couplings beyond nearest and next-nearest neighbors are negligible), where the factor of 6 arises because each atom has six nearest and next nearest neighbors. This is somewhat in tension with our PBE+U results, which from Tb. 5.1 gives $6(J_1 + J_2 + J_{1c} + J_{2c}) \sim 5.4$. Despite the fairly large overestimate, our PBE+U calculations, with $U = 0.3$ so that $D \sim 1$, notably yield reliable *relative* values of exchange constants consistent with the estimates based on our experiments. Our choice of U also predicts an AFM stripy phase to have the lowest energy of all collinear magnetic configurations examined, in line with the results of our classical model and neutron data [33]. Moreover, the tendency for DFT+U to overestimate exchange constants at small or near-zero values of U is well documented [91–93], while capturing their relative values well. Following previous work [94] we uniformly scale J_1, J_2, J_{1c} and J_{2c} so that $6(J_1 + J_2 + \cdots) = 1.1$, in line with our Curie-Weiss data, and closely agreeing with the data in Ref. [74], whose fitted temperatures predict a slightly higher $\sum_i J_i \approx 1.3$.

Taking the scaled parameters $(J_1, J_2, J_{1c}, J_{2c}, D) = (0.15, -0.0012, 0.077, -0.044, 1.09)$, we can semi-quantitatively reproduce the magnetization curve. We estimate the g-factor as $g = 2.09 = g_{\text{Fe}}$ [95]. This yields estimated critical fields of 15 and 45, as shown in Fig. 5.2. With no fitting to the experimental magnetization in Fig. 5.2, we already have found remarkable agreement between theory and experiment. Fine-tuning the J values within the range of error of the Curie-Weiss data (see Ref. [3]) moves the transition fields into even better agreement.

The UUUD phase responsible for the half-magnetization plateau is stable at the classical level over a wide range of applied fields. The model Eq. 5.3 qualitatively reproduces the critical field strengths and quantitatively captures the magnitude of the magnetization. However, it fails to describe some of the fine features of the measurements, such as the small, positive slope of the magnetization within plateaus and the intermediate phase detected by measurements between the plateau and stripy order. The symmetry constraints of the switching reported in Ref. [8] also indicate an in-plane component to the moment at zero field which is not accounted for in this model. To capture the remaining fine features of $Fe_{1/3}NbS_2$ would require a more sophisticated 3D model with vastly more parameters and temperature effects, similar to [84,96]. Nevertheless, as a minimal model that only includes a subset of
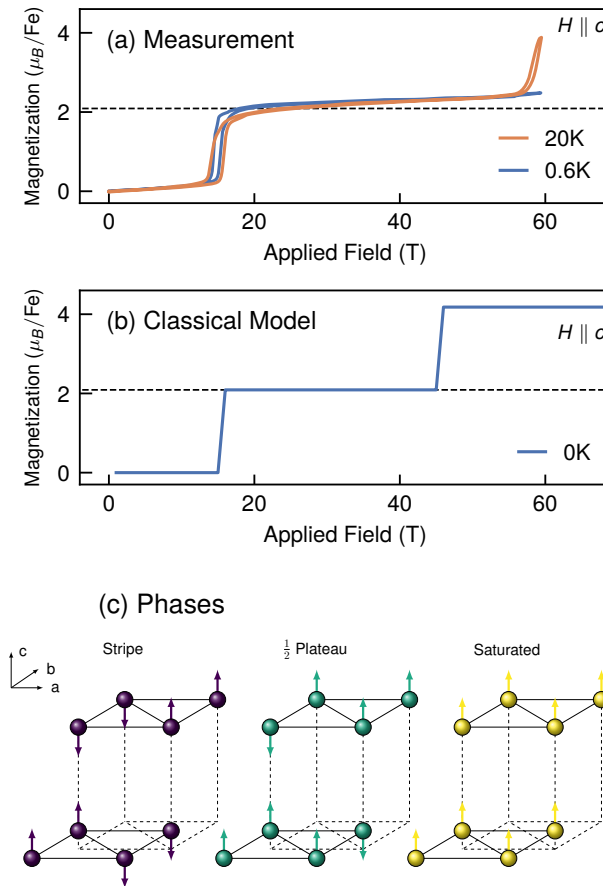
Figure 5.2: (a) Magnetization response of $Fe_{1/3}NbS_2$ to an out-of-plane pulsed field. (Data from a 25T pulse is used below 15T for the 0.6K curve.) At 0.6, the magnetization shows two flat plateaus at 0 and 1/2 of the saturated magnetization (dashed line). At 20 a further transition, likely to a fully saturated state, is observed near 60. (b) Magnetization response of the model, Eq. 5.3, computed classically. Three plateaus are clearly visible: a stripy AFM phase, a UUUD phase, and a saturated PM phase. (c) Cartoons of the spin configurations in the eight site unit cell.
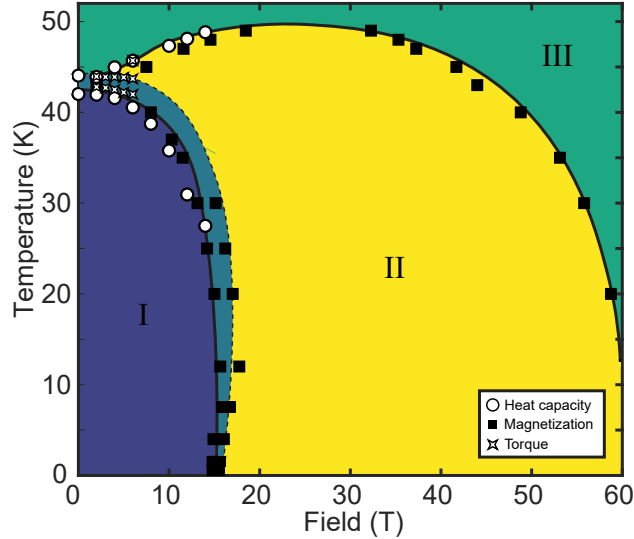
Figure 5.3: Experimental phase diagram of $Fe_{1/3}NbS_2$, as a function of temperature and field applied along the c-axis. Calculations suggest that region I is a stripe phase while region II (the plateau) is UUUD. The origin of the intermediate phase bridging the stripe and UUUD phase is not known. Phase boundaries were determined by torque magnetometry, heat capacity and pulsed field magnetization measurements; see Ref. [3] for details. Phase boundary lines are a guide to the eye.

the degrees of freedom, the model is highly consistent with measurements and seems to have identified the dominant interactions responsible for the magnetization response of $Fe_{1/3}NbS_2$.

5.6   Conclusions and Neutron Scattering

The experimentally observed magnetization is reproduced very well with a totally classical model. While the behavior seen in high fields is abnormal, it seems to be the result of abnormally large second-nearest-neighbor interactions and single-ion anisotropy creating conventional magnetic phases with an unconventional robustness. Having this second confirmation of the size of the single-ion anisotropy (the first being the Curie-Weiss fit), and considering the low-field order necessary to create such a robust region of constant near-zero magnetization before the half-magnetization plateau, it is now apparent that this system is more or less ising-like. This has significant implications for our understanding of the switching behavior in this material. In particular, the mechanism proposed in $CuMnAs$ and $Mn2Au$, and assumed in our system [8, 70, 97], involves the rotation of an in-plane Néel vector. This is no longer a meaningful model in a system with no in-plane spin component,

so a different kind of mechanism is likely at work.

While TMDs and intercalated TMDs are often thought of primarily in terms of their 2D properties, these measurements and the model that explains them makes clear that inter-layer interactions are necessary for a full understanding of their properties and behaviors – indeed, in this case $J_{1c}/J_1 \approx 1/2$.

Neutron scattering measurements have shone a light on how these ideas come together [98] in the following way. In this subsequent study, it was found that there are two zero-field antiferromagnetic phases, one of which dominates in the $x < 1/3$ system and the other in the $x > 1/3$ system, with near perfect coexistence in the $x = 1/3$ system. The energetic fa-vorability of each respective phase depends sensitively on the ratios of higher-order exchange constants, including inter-layer exchange constants. These phases are themselves nematic, so while the original spin-orbit-torque driven mechanism cannot be applied without some modification, there is a directionality to the magnetic order which in principle be redirected. These measurements also explain the 'extra' phase that is seen between the two transitions with temperature at zero field - it is the onset of one of these antiferromagnetic orders, while the lower transition is the onset of the other.

While the neutron scattering measurements suggest a straightforward explanation for the ob-served intercalation-dependence of the switching behavior, it is unclear what role might still be played by the spin glass. Certainly, this may be an important component of the process which reorients the nematic magnetic domains, or at least which enables their reorientation in such large proportion.

5.7   Appendix I: Additional Measurements

This section provides a number of additional and unabridged measurements.

High Field Magnetization

The magnetization as a function of applied field was measured in pulsed magnetic field, with several 60T and 25T measurements, shown in Fig. 5.4. The susceptibility, as determined by taking the field derivative of the magnetization data, is shown as well for ease of identifying phase transitions. The phase boundaries in the experimental phase diagram (Fig. 4 in the main text) are the centers of the hysteresis loops, calculated as the midpoint between the peaks in susceptibility on the way up (0 to 60T) and on the way down (60 to 0T). The 60T measurements taken at 0.6K and 4K have a discontinuity where the gain was saturated due to the magnetization changing too quickly during the 0 to 60T leg of the pulsed measurement. Additional measurements up to 25T were taken at those temperatures, which did not have the same saturation issue. The 0.6K measurement found in the text is predominantly from the 60T pulse, with the saturated portion of the measurement replaced with the data from the 25T pulse. The 0 to 60T leg of the measurement is entirely from the 60T pulse.
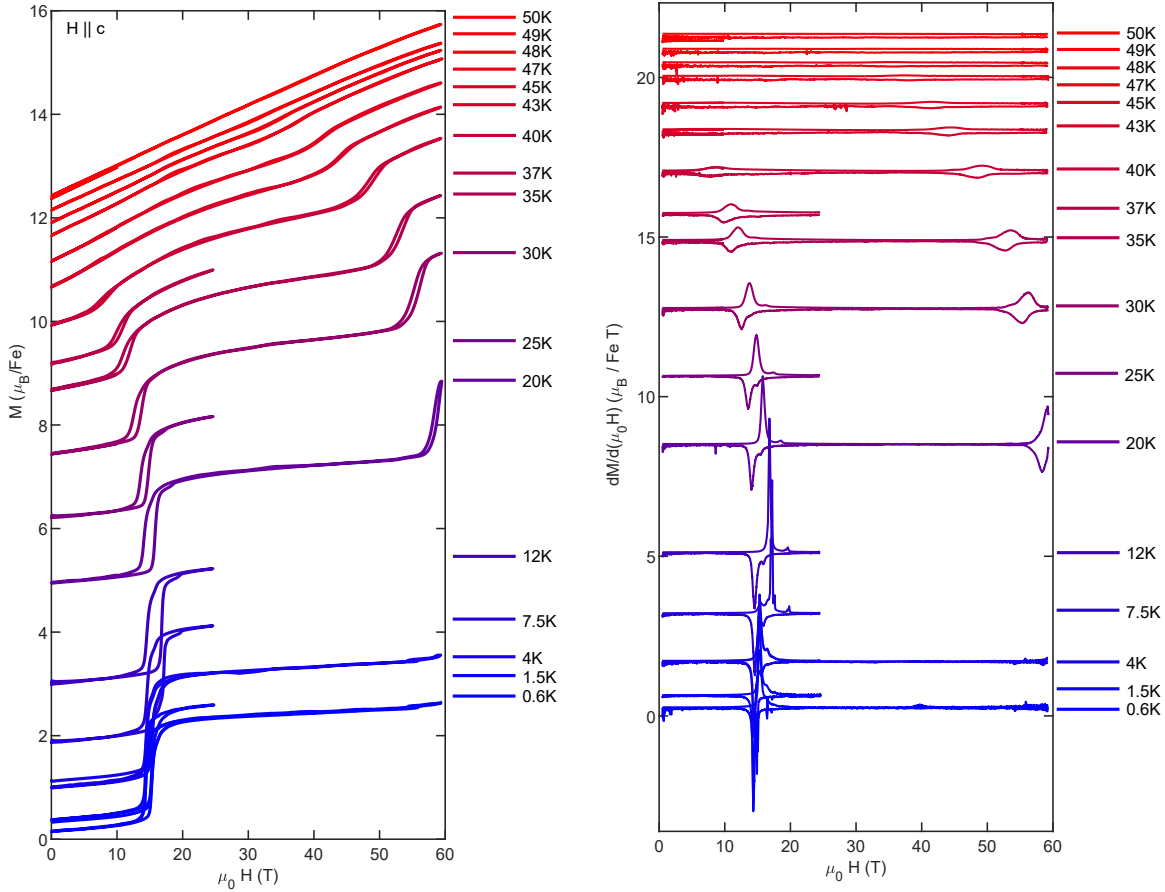
Figure 5.4: High field measurements of the out of plane magnetization (left) and susceptibilities (right), taken at a variety of temperatures.

DC Field and Single Crystal Measurements

The primary results presented in this paper are based on 60T pulsed field measurements of a stack of 30 co-aligned crystals all from the same growth batch. The nature of these results, including the sharpness and location of the transition, was confirmed via 30T DC field measurements of the stack (Fig. 5.7 (a)) and 60T pulsed field measurements of a single crystal (Fig. 5.7 (b)). The center of the phase transition does not move with the slower sweep rate of a DC measurement, although it does broaden slightly. There is strong agreement between the pulsed field single and stacked crystal curves. This shows that the location of the transition is not sample dependent, and that the primary observed effect is not an artifact of a multi-sample measurement. The single crystal measurement has a flatter character than the stack measurement; this could be due to slight misalignments in the stack, a smaller number of domains in one crystal as opposed to a stack of 30, or a stronger influence of the

background on a smaller signal, to name a few possibilities. The single crystal was a part of the measured stack; it was chosen from the stack because it was the thickest, at about 0.2mm.

High field magnetization with more iron

Pulsed field measurements of Fe_xNbS_2 with $x = 0.339$ (slightly higher iron content than the perfect $x = 1/3$) are similar to those of the main sample studied in the text, $x = 0.330$, with plateaus in the magnetization appearing at low temperature (Fig. 5.5). The exact locations of the transitions differ from the locations found in the main $x = 0.330$ sample, indicating a sensitive dependence of the phase boundary location on the exact iron content. It should be noted that this pulsed field data on the $x = 0.339$ sample is not background-corrected (a procedure which requires a second magnet pulse to go along with each measurement), and so its precise shape may differ slightly from what is presented.

Torque Magnetometry

The anisotropy of the magnetic response of Fe_xNbS_2 was further studied via torque magnetometry. The full dataset is given in Fig. 5.6 (a). The measurement was performed with a magnetic field applied at various angles θ with respect to the sample's c-axis, as shown in Fig. 5.6 (b). For each temperature and field, the torque as a function of angle θ was fit to an equation of the form $\tau = Q_1 \sin(2\theta) + Q_2 \sin(4\theta)$, as illustrated in Fig. 5.6(c). These components were then analyzed as a function of temperature at each field in order to identify phase transitions (Fig. 5.6(d) and (e)). The two strongest features correspond to the lower-temperature and intermediate-temperature phase boundaries shown in the phase diagram in the main text. Notably, these features are identified using different components of the torque response.

In-plane Heat Capacity

While the transitions move dramatically with the application of field along the c-axis (Fig. 2(b) in the main text), magnetic field applied perpendicular to the c-axis has no effect on the heat capacity or on the transitions that it probes, as seen in Fig. 5.7(c).

Susceptibility vs Temperature

The phase transitions discussed in the main text are also visible in DC field measurements taken as a function of temperature, shown in Fig. 5.7 (d).
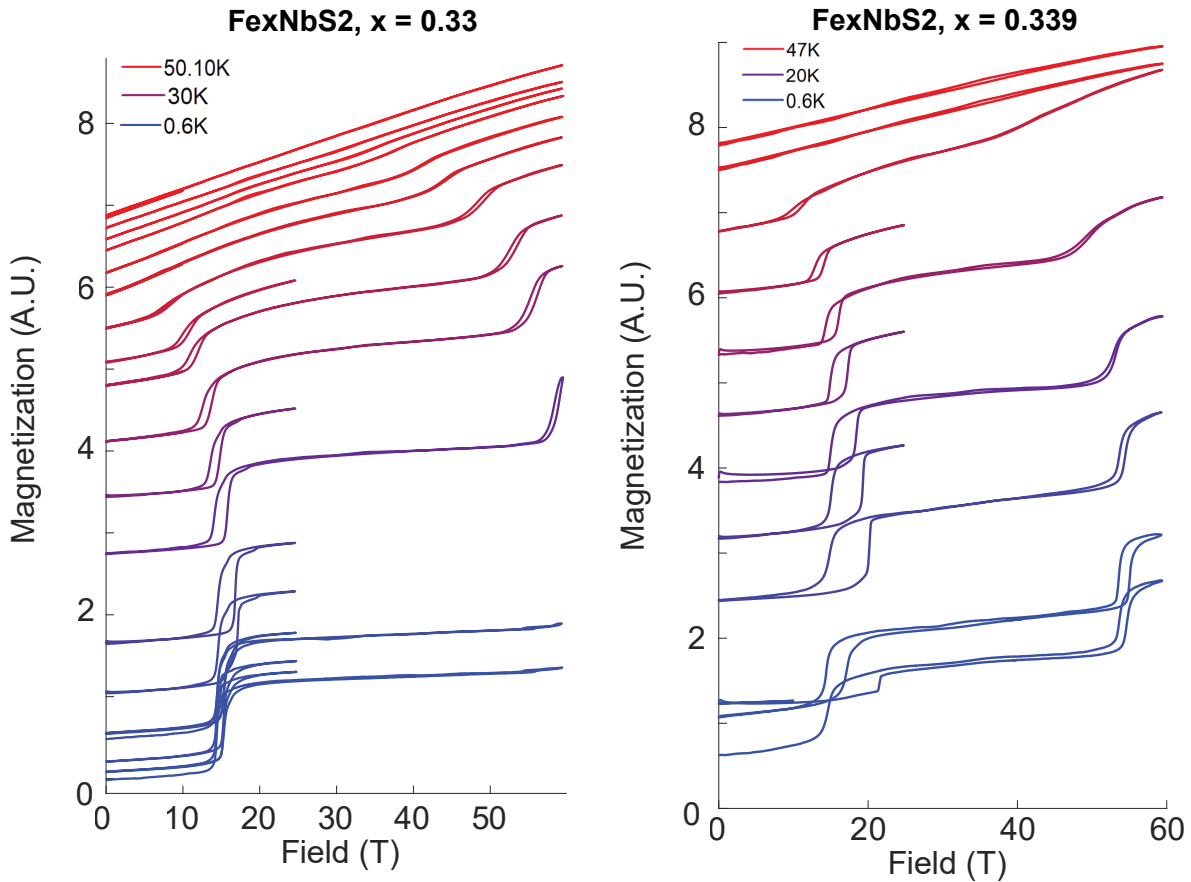
Figure 5.5: A side-by-side comparison of the pulsed field magnetization of $Fe_{0.33}NbS_2$, left, and $Fe_{0.339}NbS_2$, right.

Additional Intermediate Phase

The main text focuses on the dominant features seen in the heat capacity and magnetization. However, there is also a minor peak visible in both measurements, shown in magnetization in Fig. 5.8. We ascribe this feature to an intermediate phase between the stripy and plateau phases. However, since the corresponding peaks are small, it is not possible to track the transitions with the same level of certainly as the dominant phases. Nevertheless, the intermediate phase seems to have magnetization of around 1.6, which is almost exactly 1/3 of the saturation magnetization. This is suggestive of a connection to UUD spin configurations in a three spin unit cell, which are responsible for 1/3 magnetization plateaus.
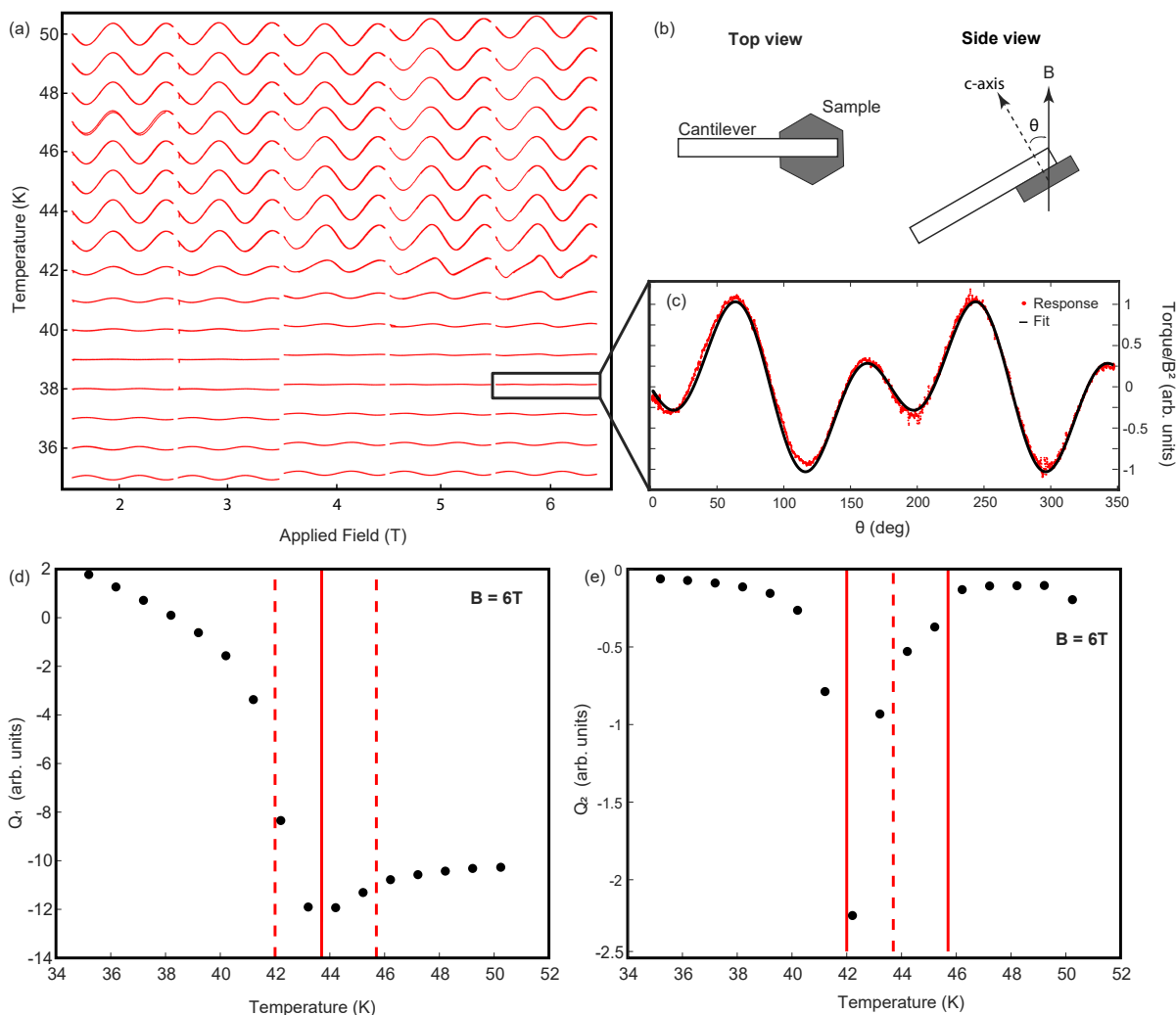
Figure 5.6: (a) Torque-vs-angle curves at temperatures from 35 to 50K, and fields from 2 to 6T. The curves shown are normalized to the field squared, but this is not important for the analysis, which compares measurements taken at the same field. (b) Schematic of the experiment, establishing the relevant directions and meaning of the angle θ. (c) An example of a response curve shown with its fit. This measurement was taken at 38.2K and 6T. (d) and (e) The amplitudes of the $\sin 2\theta$ and $\sin 4\theta$ components, respectively, of the response curves as a function of temperature. A solid red vertical line indicates the identification of a transition from the given plot. A dotted red vertical line indicates the location of a transition which was identified from the other plot.
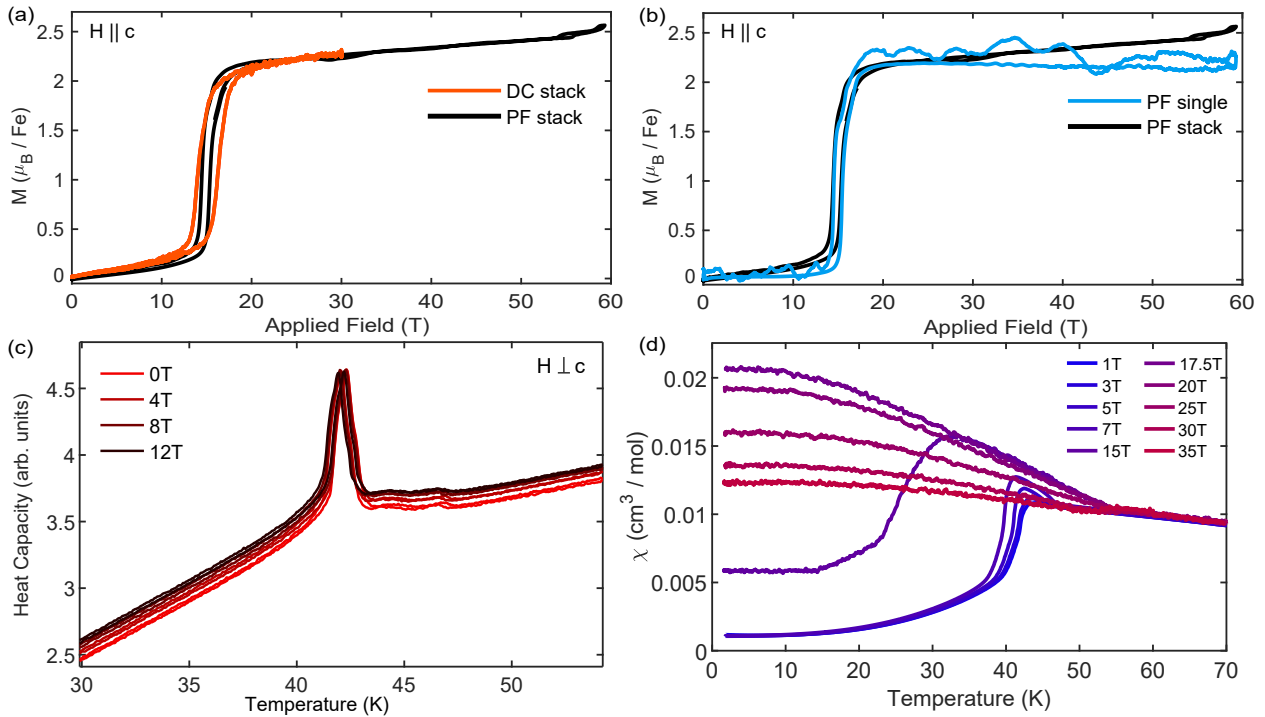
Figure 5.7: (a) Comparison of the magnetization measured in 30T DC field to the magnetization measured in 60T pulsed field (PF). The DC measurement was taken at 1.6K, and the PF measurement shown was taken at 4K. (b) Comparison of PF measurement of a single crystal to PF measurement of the stack of crystals used for the primary results of this paper. Both measurements were taken at 4K. (c) Heat capacity with an in-plane applied magnetic field. (d) Susceptibility as a function of temperature measured in fields ranging from 1T to 35T.

High Field Transport

Transport measurements taken in 60T pulsed field are shown in Fig 5.9. These measurements show increased scattering at the primary phase boundaries, as seen in the magnetoresistance, as well as a change in slope of the Hall resistance over the transition.
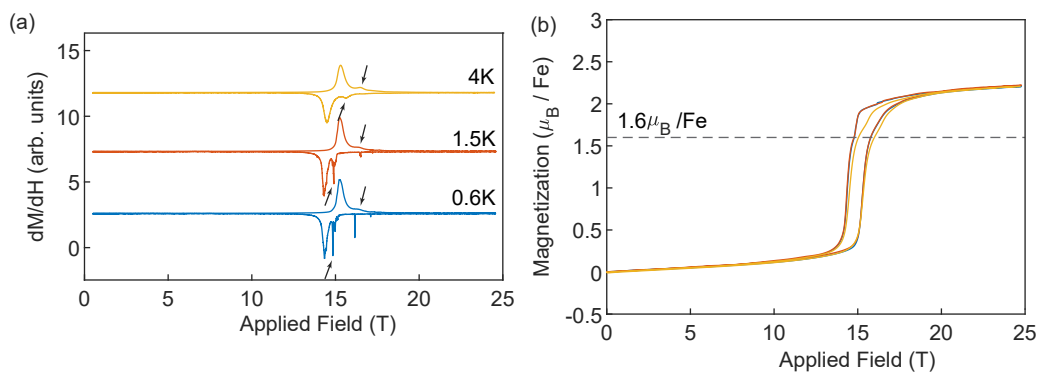
Figure 5.8: (a) Susceptibility measured at 4K, 1.5K, and 0.6K, offset for discernibility. Small features corresponding to intermediate phase boundary are indicated with black arrows. (b) Magnetization at these temperatures, with dotted line indicating 1.6, which is approximately 1/3 of the saturation magentization.
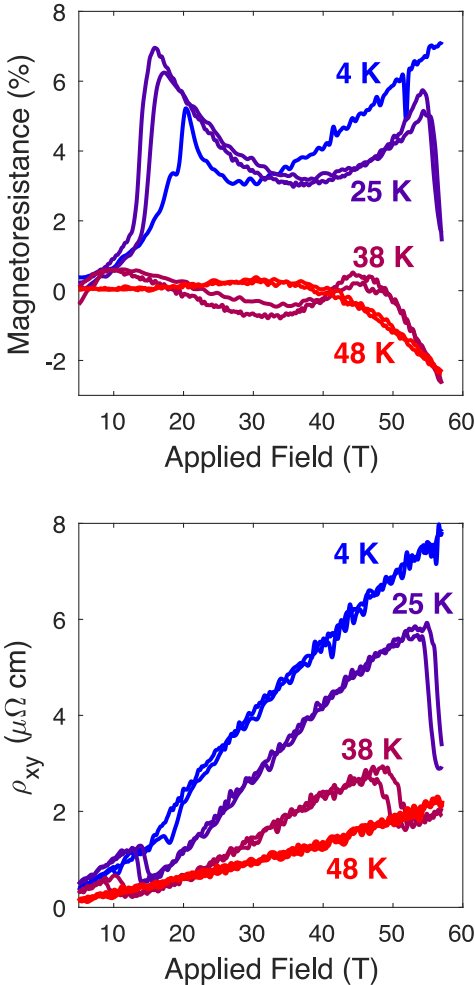
Figure 5.9: Magnetoresistance and Hall resistance measured in high pulsed field.

Chapter 6

Non-local Switching

"We can only see a short distance ahead, but we can see plenty there that needs to be done."

– Alan Turing

Materials in this chapter were previously published in

- Shannon C. Haley, et al., Long-range, Non-local Switching of Spin Textures in a Frustrated Antiferromagnet, arXiv:2111.09882 (2022).

6.1 Introduction

At this point, the question of what comprises the switched states seems to be more or less resolved: anisotropic antiferromagnetic magnetic domains of specific orientations are selected for by the switching pulses. This interpretation follows most directly from (1) the correspondence between the threshold switching current and the antiferromagnetic order parameter as measured in neutron scattering, (2) the geometry-dependence of the switching response, (3) DFT calculations of the conductivity anisotropy of the magnetic domains, and, perhaps most compellingly, (4) the opposite switching responses observed in stripe- and zig-zag- dominated samples.

Certain details remain to be addressed, however. In particular, what underlying mechanism leads the domains to re-orient in response to a current pulse? Conventional insight would point to the spin orbit torque exerted on the localized moments by the applied current, which becomes spin-polarized thanks to the inverse spin galvanic effect. Indeed, our system has the correct symmetry for this, as discussed in Section 4.2. The overwhelmingly out-of-plane nature of the antiferromagnetic order, though, and the unchanging direction of the Neel vector this implies, points to the necessity of some additional subtlety in this interpretation. In developing this more subtle treatment, it is perhaps necessary to consider the features of this material beyond its spin texture. Two very notable considerations are the spin glass phase and magnetoelastic coupling that had previously been observed in these samples. The

experiments that will be described in the following sections originally were conceived of in order to explore the role of the former in the switching response, and ultimately pointed to the previously unappreciated importance of the latter.

6.2 Spin glass superfluids

As the amount of iron between layers of niobium disulfide increases from 0.31 to 0.35 iron atoms for every niobium atom, one kind of antiferromagnetic order dies in favor of another. As discussed in Section 3, these otherwise single-phase-dominated samples also host a disorder-based magnetic behavior, however, which they do not share with the mixed-phase $Fe_{0.33}NbS_2$: a spin glass. Intuitively, this can lead to abnormal memory behaviors due to the complicated energy landscape that the spins collectively explore, with many local minima to occupy in a strongly history-dependent way. It is likely that this aspect of the spin glass contributes to the robustness of the switching response, although it is difficult to disentangle this effect from the simple fact of having a single dominant phase, as there is not an intercalation level which exhibits both significant spin glass behavior and co-dominance of multiple AFM phases.

Another aspect of the spin glass which may contribute to the robustness of the switching response relates not to the prolonged memory of the device – seen in the long timescales over which the altered resistance does not move – but to the extended reach of a switching pulse – seen in the large amplitude of the response. Ref. [99] describes how a spin superfluid can emerge in spin glasses, and more generally in frustrated spin systems: due to the existence of a continuous set of degenerate spin orientations, torque is transmitted in a dissipationless way through the system.

6.3 Non-local switching response in iron-intercalated niobium disulfide

The switching response in iron-intercalated niobium disulfide follows a characteristic shape as a function of the current density of the switching pulses. The material shows no response up to a certain current density, then displays unstable switching behavior which varies across devices for a small window of current densities, after which it stably switches with a large amplitude, and then finally the amplitude decays with further increased current density. In most devices, this decay does not go all the way to zero switching response.

The switching response away from the active area of the device is a bit simpler; at a higher current density than was required to switch the device locally, a response in the nonlocal channel is registered. this response persists for a small range of current densities and then the system returns to no observable response. There are two curious features of the nonlocal switching response which bear further consideration: first, in nearly all devices measured the

nonlocal response has an opposite sign to the local response, and second, the further set of nonlocal contacts often sees a stronger response than the closer set.

6.4 Strain measurements

The two order parameters are known to have strong magneto-elastic coupling [100] and so it is likely that strain can be used to tune the switching behavior. To demonstrate this, we study the switching behavior under strain. Fig. 6.1(b) and (c) show switching responses observed for the same $x = 0.31$ device, where (b) is the response after the device is cooled with no applied strain and (c) is the response after being cooled with strain (corresponding to an applied $40V$ to the piezoelectric cube the device was mounted on). At the current density shown, there is a change in sign of the switching response due to the applied strain. At higher current densities, the original sign is recovered (see Fig. 6.5 in this chapter's appendix), so that there is a sign flip as a function of the pulse current density. This similarity to the $x = 0.33$ sample behavior could be explained by the strain subtly altering the RKKY-dominated exchange constants and allowing a slight increase in the minority zigzag phase, as illustrated in Fig. 6.1 (e). Supporting this, the lattice distortion associated with magnetic ordering is small, with high-resolution synchrotron powder XRD measurements taken at low temperatures showing an a lattice parameter of 5.65407 ± 0.00015Å for the zig-zag-dominated samples and 5.65486 ± 0.00018Å for the stripe-dominated samples (See Figs. 6.7, 6.8, 6.10, and 6.9 in this chapter's appendix). This corresponds to a difference on the order of 0.1%, which is what is achievable with the piezoelectric cube used for this experiment. Strain can therefore tune the switching response for a $x = 0.31$ device, to that of a device with $x = 0.33$ – a direct indication magneto-elastic coupling can be used to manipulate the domain structure of the magnetic texture.

The complexities of the competing order parameters notwithstanding, the collective dynamics associated with the ordered phases or with the coexisting spin-glass phase will have collective modes that can carry spin currents. Typically, scattering off conduction electrons has limited the spin decay length to nanometers, and only in a small number of insulating antiferromagnets can this be extended to microns [101–104]. To our knowledge, such magnons have not been used to also store information non-locally in the same antiferrromagnet. In this study we show that this unusual situation can be realized. By leveraging the intertwined order parameters of Fe_xNbS_2, spin information is not only carried far from the regions carrying the pulse current, but can also be stored non-locally, tens of microns away from the active area.
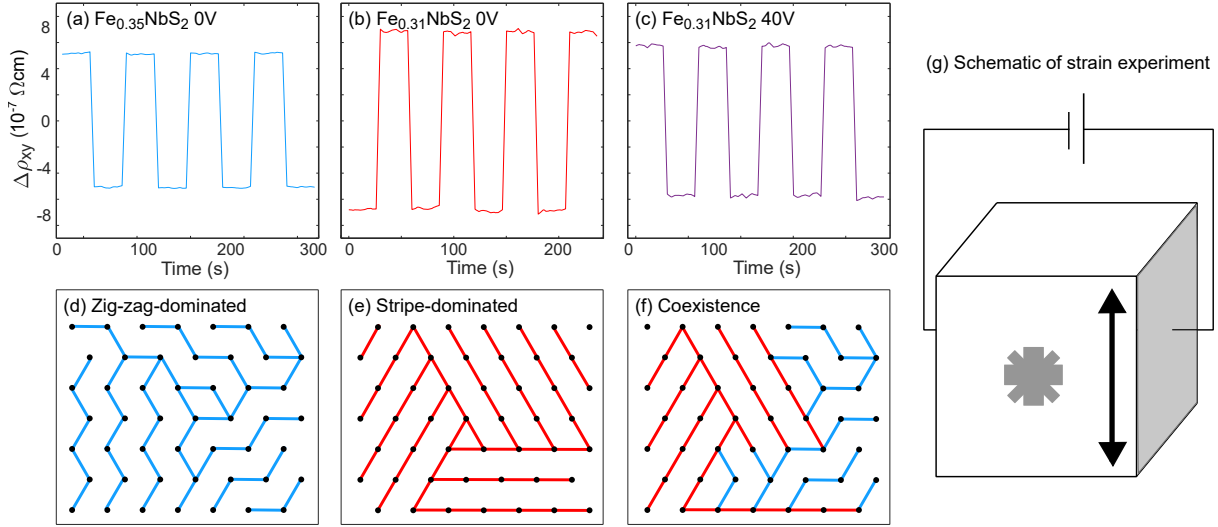
Figure 6.1: Switching behavior under applied uniaxial strain. (a)-(c) The change in transverse resistivity while $10ms$ DC current pulses of about $5 \times 10^{-4} A/cm^2$ are applied in alternating directions. (a) Measurement for a device made of $Fe_{0.35}NbS_2$ with no applied strain. (b) Measurement for a device made of made of $Fe_{0.31}NbS_2$ with no applied strain. (c) Measurement for a device made of $Fe_{0.31}NbS_2$ following cooling from room temperature with applied strain corresponding to $40V$ on the piezoelectric cube the device was mounted on. (b) and (c) were measured on the same device. Complete dataset with pulse current dependence is available in this chapter's appendix (Fig. 6.5). (d) Dominant spin texture in $Fe_{0.35}NbS_2$. (e) Dominant spin texture in $Fe_{0.31}NbS_2$. (f) Proposed spin texture in $Fe_{0.31}NbS_2$ cooled under strain. Proportion of zigzag phase is exaggerated. (g) Schematic of strain measurement. Voltage is applied between two electrodes around a cube of piezoelectric material, causing a directional expansion of the material which strains the device mounted on the cube.

6.5 Results

Measurements presented in this work were primarily performed on samples of $Fe_{0.35}NbS_2$. Heat capacity and magnetization measurements of characteristic samples are shown in Fig. 6.2 (a) and (b), respectively, showing magnetic transitions and spin glass behavior consistent with our previous characterizations of $Fe_{1/3}NbS_2$ and $Fe_{0.35}NbS_2$. [105, 106] In Fig. 6.2 (c) we illustrate a device designed to measure the non-local switching response of the antiferromagnetic texture of Fe_xNbS_2. DC current pulses are applied along the directions denoted as A and B, with a view to triggering magnons that can transport spin down the neck of the device. After the application of a pulse, the transverse resistance as measured with an MFLI lock-in amplifier using an AC probe current (denoted with I_{probe}) at three distinct locations
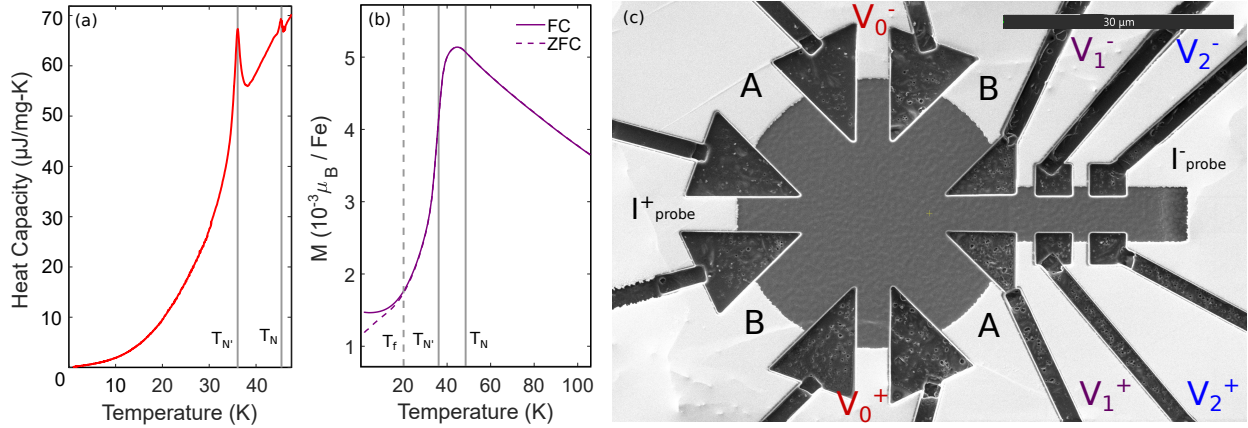
Figure 6.2: Basic characterization of devices made of $Fe_{0.35}NbS_2$. (a) Heat capacity as a function of temperature. Vertical solid lines marks T_N and $T_{N'}$, the AFM transitions. (b) Magnetization as a function of temperature measured in 1000Oe along the c-axis. The field-cooled (FC) measurement, shown as a solid curve, was measured from low to high temperature after cooling the sample in an 1000Oe field. The zero-field-cooled (ZFC) measurement, shown as a dotted curve, was measured from low to high temperature after cooling the sample with no external field. Vertical dotted and solid lines indicate the onset of the spin glass behavior (T_f) and the AFM transitions (T_N and $T_{N'}$), respectively. (c) A switching device made from a bulk crystal. The two pulse bars are marked A and B. The AC probe current is applied along the path marked I_{probe}. The local signal is measured using the contacts labeled V_0, and the non-local signals are measured using the contacts labeled V_1 and V_2.

goes to either a higher or lower resistance state, depending on whether an A or B pulse has been administered. More information about this can be found in the Methods section. The low temperature longitudinal resistivities of the devices measured had some small variations but were generally close to $10^{-4}\Omega cm$. The contacts marked V_0, which intersect the current pulse bars, will be referred to as local, and the contacts marked V_1 and V_2 will be referred to as non-local in this paper.

Fig. 6.3 (a) shows the local response as a function of pulse current density. The response is not monotonic, instead turning on at about $8 \times 10^4 A/cm^2$, quickly reaching a maximum, and then decreasing slightly to reach a stable level around $11.4 \times 10^4 A/cm^2$. The measurements taken at $25\mu m$ and $35\mu m$ from the center of the active portion of the device are shown in Fig. 6.3 (b) and (c), respectively. The measurement taken $35\mu m$ from the center requires a larger current density to register a change from the pulses than is necessary at $25\mu m$ from the center, and both require larger current densities than the local response. The relative sizes of the responses vary from device to device, but the current density required is largely

unchanged. Similar devices made of Fe_xNbS_2 $x \approx 1/3$ show weak local switching, but no stable switching response at the non-local contacts (supplement). The progressively larger current densities required to observe a switching response further from the active area of the device is largely consistent with the propagation of magnons, which dissipate with distance. There are two notably surprising aspects to this result, however. First, the non-local contact V_2, while requiring a larger current density, tends to have a larger switching response than the non-local contact V_1. As discussed below, an important reason for this is that the former is closer to the edge of the crystal. Second, the non-local contacts generally exhibit an opposite switching response to the local contacts V_0, so that the pulse directed in the same direction (A or B) will raise the local transverse resistance and lower the non-local transverse resistance. This suggests that the preferred domain orientation upon a current pulse differs between the two regions.

The response of ρ_{xx} between the $25\mu m$ and $35\mu m$ non-local contact is shown in Fig. 6.3 (d). The non-local R_{xx} response closely mimics the $25\mu m$ non-local R_{xy} response, with a peak just below $10.5 \times 10^4 A/cm^2$. The response of ρ_{xx} is notably absent where the $35\mu m$ non-local ρ_{xy} response is strongest; this suggests that the full conductivity tensor is affected in the $25\mu m$ non-local region, whereas the $35\mu m$ non-local region has a dominant response only in the off-diagonal components ρ_{xy}. This could be explained by increased domain-wall scattering in the former, whereas the latter has fewer domains. In order to explain the opposite response between the local and $35\mu m$ non-local switching, the average principal axis of highest conductivity must be similarly oriented in the perpendicular direction.

Fig. 6.4 (b) shows the temperature dependence of the pulse current with the maximum switching response for both local and non-local contacts; this is based on an analysis of data shown in Figs. **??**, 6.11, and 6.12 in this chapter's appendix. These measurements were taken on a device with non-local contacts $20\mu m$ and $27\mu m$ away from the center of the active area. At all three locations on the device, the threshold switching current grows with increasing temperature below the AFM temperature, closely mimicking neutron scattering measurements of the peak intensity corresponding to the AFM order parameter (Fig. 6.4(a)). This, and the disappearance of the switching response at the Néel temperature, demonstrates a direct connection between the threshold current for switching and the opening of an AFM gap.

6.6 Discussion

The temperature dependence of the switching amplitude shown in Fig. 6.4 is strongly indicative that the threshold current required for the switching is proportional to the magnitude of the antiferromagnetic order parameter. The nonmonotonic shape of the switching behavior as a function of current density observed locally is also observed in the non-local contacts, suggesting the same underlying behavior is also present in these regions. Collective excitations carry spin and rotate the spin texture in these non-local regions in the same way that the spin-polarized current pulses do in the local region.
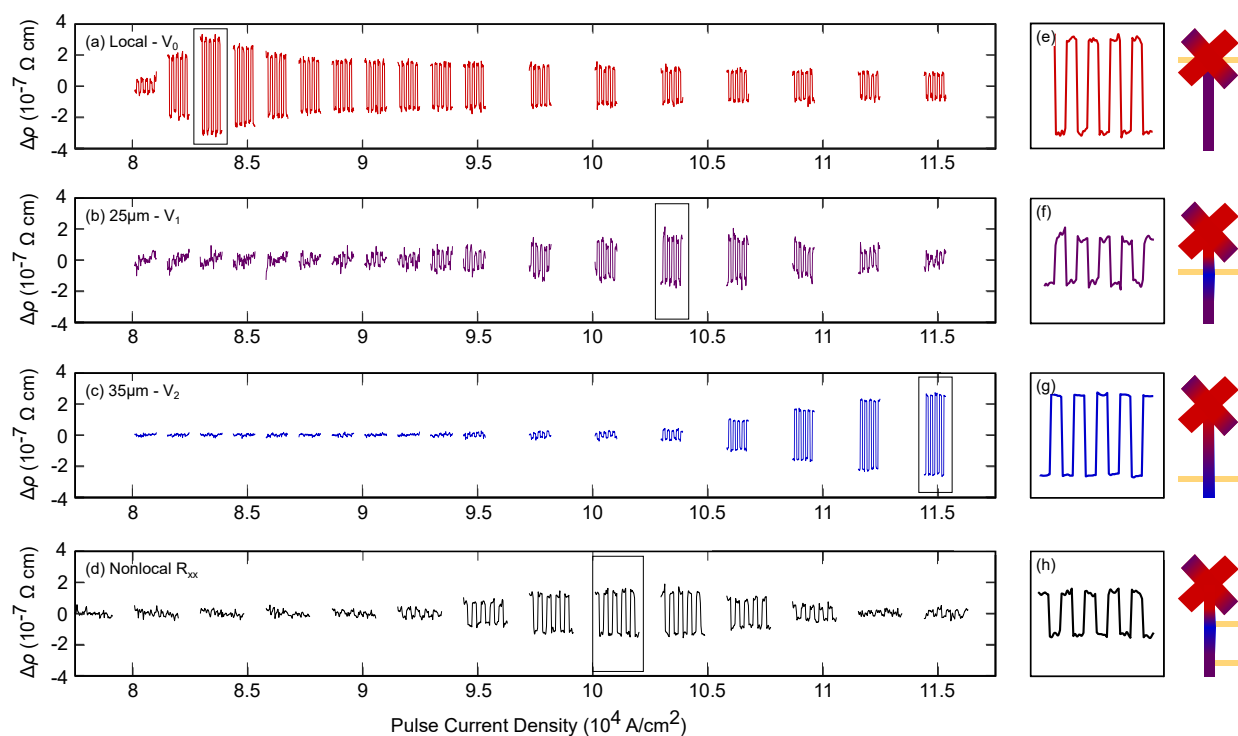
Figure 6.3: Switching responses shown at various pulse current densities. (a) Transverse resistance response measured locally between the contacts labeled V_0. (c) Transverse resistance response measured $25\mu m$ from the center of the device, between the contacts labeled V_1. (e) Transverse resistance response measured $35\mu m$ from the center of the device, between the contacts labeled V_2. (d) Longitudinal resistance measured on the non-local portion of the device, between two adjacent contacts labeled V_1 and V_2. (e), (f), (g), and (h) Single sets of switching responses at the current densities indicated on the left. Schematics to the right illustrate locations of measurement contacts, with shading indicating possible domain distribution at the given current density (red and blue are perpendicular domains and purple indicates multi-domain regions).
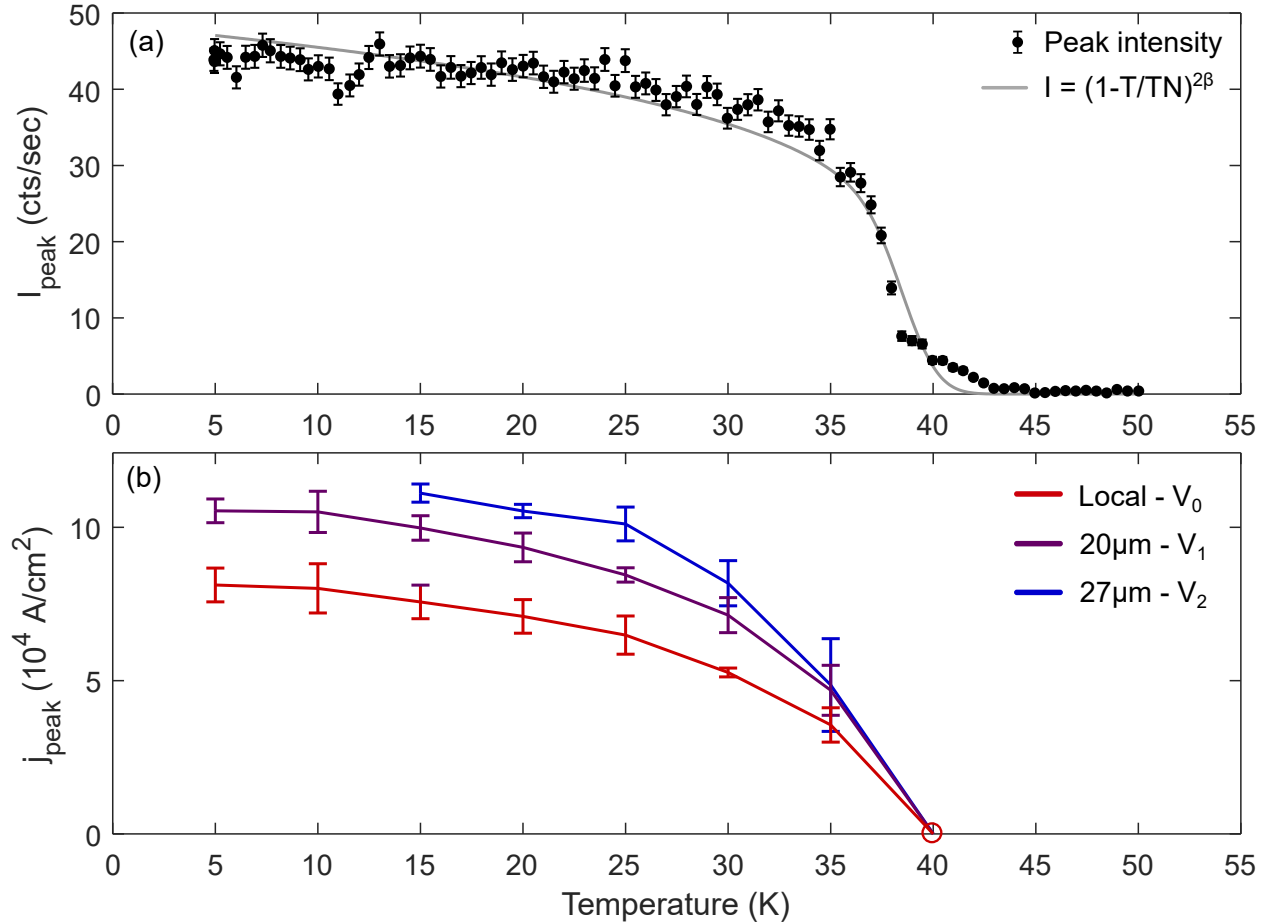
Figure 6.4: Comparison of temperature dependencies of neutron scattering measurements and switching measurements. (a) Order parameter peak intensity measured with neutron scattering as a function of temperature, with the associated critical exponent fit, with $2\beta = 0.21(2)$. (b) Current density of peak switching response as a function of temperature, for all three sets of measurement contacts. Peak switching was determined by fitting the amplitudes of the responses to a Gaussian model, whose standard deviations give the uncertainty indicated by the error bars. The open circle at $40K$ denotes the lack of switching at this temperature regardless of current density. The full dataset can be found in this chapter's appendix.

Two unusual features from the data deserve some attention. (i) The non-local response closer to the active area has a consistently smaller signal than that closer to the crystal's edge. (ii) The second non-local region has an average principal axis of highest conductivity that is always oriented perpendicular to that of the local region.

We suggest that both of these effects are connected by the elastic response of the system. Little et al. recently showed that the antiferromagnetic order is strongly coupled to a structural distortion. Here, we have demostrated that strain can directly control the sign of the switching response (Fig. 6.1(b),(c)) [107]. The situation is similar to the physics of martensites, where magnetostrictive effects can prefer a multi-domain state as the total elastic energy is balanced against the energy penalty of creating a domain boundary. [108] For clamped samples, such as those studied here, the incompatibility between the bulk strain induced by the AFM order and the surface strain acts as an "elastic charge" that produces a long-range field [108–111] introducing a competing energy that can make multi-domain states favorable – a situation comparable to the long-range magnetic dipole fields in FMs [112]. Therefore, away from the local regions where spin is transferred due to the driving current, the system will tend to rotate in the opposite direction in order to preserve the balance of domains in different orientations.

Since the clamped boundary is the originator of the long-range forces, it is natural to expect that this effect is most stark close to the crystal's edge, as seen in the $35\mu m$ non-local ρ_{xy} response, while the region surrounding the closer non-local contacts would need to rearrange less. The $25\mu m$ non-local response would then detect domain wall scattering and smaller re-orientations of the Néel vector, explaining its relatively smaller response in ρ_{xy} and larger response in ρ_{xx}, which is amplified by domain boundary scattering. Finally, we note that in order for this mechanism to be effective, the internal strain of the device must be significant – comparable to the strains applied in our experiment shown in Fig. 6.1(g) of $\sim 0.1\%$. Given that anisotropy of the lattice parameters themselves is only $\sim 0.1\%$, this suggests that the applied current pulses must orient a significant fraction of the device into a single domain, away from the active area. This also explains the reduction of ρ_{xx} at higher currents, which would be lowered by the reduction of domain walls.

Disorder [113, 114], entropy [115, 116], and leakage current provide alternative explanations for the equilibrium domain configuration between pulses. Disorder-driven domain formation, however – in which domains are tied to defects – does not explain the stronger signal at the farther non-local contact nor its sign being opposite to the local contacts. Similarly, leakage current also does not explain why switching is so much stronger in the farther non-local contact V_2 than in V_1. Entropy-driven domain formation should be strongest close to the Néel temperature, which is inconsistent with the switching being enhanced as the temperature is lowered below the transition. We therefore suggest that the natural explanation is the combined action of spin-carrying collective excitations coupled to the magnetoelasticity of the system.

Typically, metals transport spin via their conduction electrons, while magnetic insulators transport spin through collective excitations such as magnons. Conduction electron spin currents generally decay more quickly than magnon spin currents, and in practice antiferro-

magnetic metals in particular tend to have very short spin diffusion lengths, largely around or under $2nm$ - as is, for example, the case in Mn based alloys. [117–121]. In magnetic insulators, on the other hand, spin decay in single crystal systems has been extended to ten microns (see the case of α-Fe_2O_3 [104]). To account for the long distances of spin transport observed, the transport medium in the present system is likely to also be collective modes. This is further suggested by the particular relationship between disorder and switching that we see - while the presence of disorder should decrease the efficiency of spin transport and spin torque mediated by conduction electrons [122], it has been proposed as an avenue for spin superfluidity when considering the dynamics of localized electron spin [99]. We observe the strongest switching responses - both locally and non-locally - in samples with excesses or deficiencies of iron. While these are the samples with single domain types, as found through neutron scattering, they are also disordered, as can be seen in the suppression of peaks in their heat capacity, as well as in the suppression of the magnetic ordering temperature as compared to the pristine samples.

Our data suggests that the spin imparted by the current pulses is not only carried by the partially spin-polarized electrons, whose generating mechanism has been discussed in Refs. [68, 71, 123, 124], but also by the collective excitations launched by the pulses, allowing regions of the sample that are tens of microns away to be switched. These scales are orders of magnitude larger than spin decay lengths of typical metallic antiferromagnets, which is a welcome discovery relevant for potential technologies based on such materials. [117] One question is to which order the collective excitations belong. A natural candidate is the antiferromagnetic order itself, whose magnons transfer their spin to the nearest domain wall. However, multiple pulses in the same direction would be expected to lead to incremental changes in ρ_{xy} as the wall is pushed, whereas we observe single-pulse saturation of the signal. Another scenario is that there exists a collective mode capable of carrying spin that travels through domain boundaries with relative impunity. The presence of a spin glass is a candidate, arising from magnetic disorder or from the frustration of two ordered ground states. [72] Importantly, recent evidence suggests that the spin glass and the antiferromagnetic order are strongly exchange-coupled. [106] Future work is needed to reveal the microscopic mechanism behind the non-local response, but for now it would be interesting to see whether other electrically switchable antiferromagnets can show similar behavior. The observation of non-local switching due to collective antiferromagnetic dynamics could open a new pathway to magnonic memory and other spintronic applications of complex antiferromagnets.

6.7 Methods

Single crystals of Fe_xNbS_2 were synthesized using a chemical vapor transport technique. A polycrystalline precursor was prepared from iron, niobium, and sulfur in the ratio $x : 1 : 2$ (Fe:Nb:S). The resulting polycrystalline product was then placed in an evacuated quartz ampoule with iodine as a transport agent (2.2 mg/cm^3), and put in the hot end of a two zone MTI furnace with temperature set points of 800 and 950 for a period of 7 days. High

quality hexagonal crystals with diameters up to several millimeters were obtained.

Devices were fabricated using the FEI Helios G4 DualBeam focused ion beam at the Molecular Foundry at LBNL. The devices were mounted on Torr Seal and sputtered with gold for electrical contact. In most cases the crystals were exfoliated to reach a thickness under $4\mu m$. The switching pulses were single square waves administered with Keithley 6221 Current Sources.

Transport was measured during the switching experiments via an MFLI lock-in amplifier. An AC probe current ran through the device both during and in between switching events, and for each measurement in this work had an rms value between $25\mu A$ and $100\mu A$ and a frequency of either $277Hz$ or $1333Hz$. Measurements were also taken with the AC probe current turned off and its corresponding leads removed during the switching event itself, and the resulting switching behavior was unchanged. A range of AC probe frequencies were also tested, and aside from an increase or decrease in noise there was no measurable difference in the resulting behavior. Both of these tests can be found in this chapter's appendix.

Low field magnetization measurements were performed using a Quantum Design MPMS-3 system with a maximum applied magnetic field of 7 T. AC heat capacity was measured using a Quantum Design PPMS system.

High-resolution wide-angle x-ray powder diffraction measurements were performed on the beamline 28-ID-1 at the National Synchrotron Light source II at Brookhaven National Laboratory. The raw data were collected by the incident beam with a wavelength of 0.1668 Åand a Perkin-Elmer area detector, and transformed to diffraction data. The Rietveld refinement was carried on by GSAS-II [125]. Single-crystal neutron diffraction experiment was performed on BT-7 at the NIST center for neutron research.

6.8   Appendix I: Additional Measurements

This section provides a number of additional and unabridged measurements.

Strain

Uniaxial strain measurements were performed by mounting a device on a picma chip actuator. The device was about $3.5\mu m$ thick with pulse bars about $5\mu m$ wide, and was mounted on Stycast. All measurements were performed at 2K. From top to bottom in Fig. 6.5, the switching was conducted on the device with: no voltage (strain) applied, 40V applied at 2K, 40V applied during cooldown, and no voltage applied following the previous measurements. No difference is seen when strain is applied solely at 2K, but a sign flip is observed at about $50kA/\text{cm}^2$ when the device is cooled with 40V applied to the piezo, highlighted in blue. The
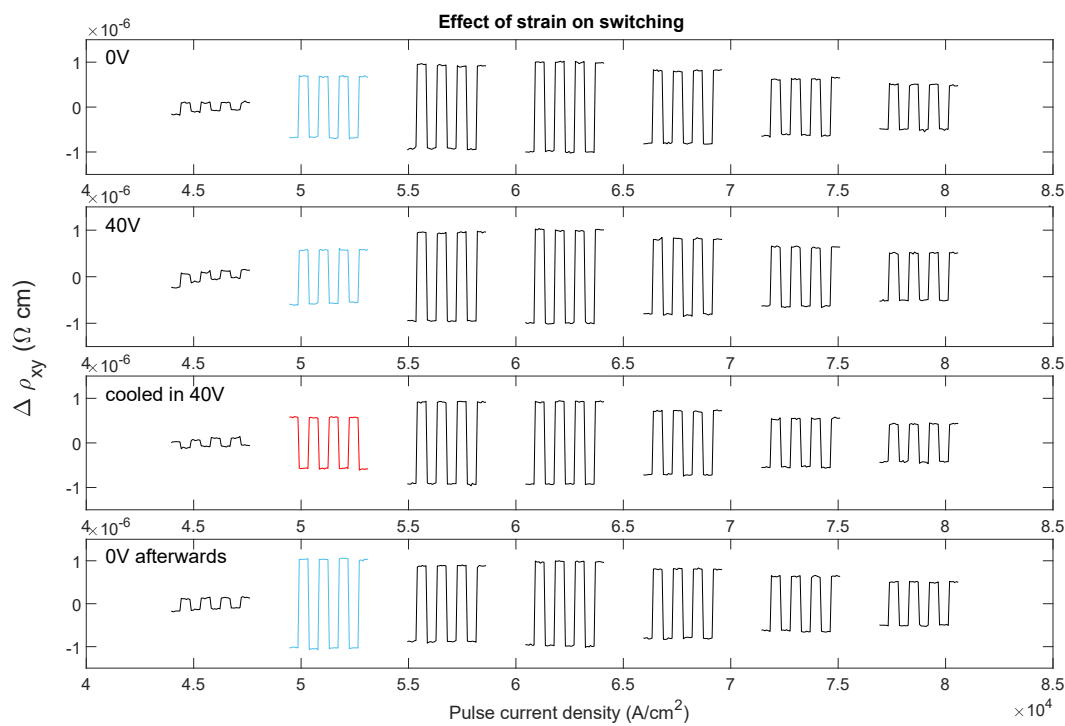
Figure 6.5: Local switching as a function of pulse current density measured for a device with and without applied strain.

amplitude of the switching is also slightly suppressed for that preparation.

Non-local measurements in $Fe_{0.33}NbS_2$

Non-local measurements were performed on a sample of $Fe_{0.33}NbS_2$. While a weak reversible switching signal is observed in the local channel, the nonlocal channel sees jumps that do not move back and forth between stable resistance states.

PXRD

High-resolution synchrotron powder x-ray diffraction measurements were taken on samples of $Fe_{0.31}NbS_2$ and $Fe_{0.35}NbS_2$ at room and low temperature, as shown in Figs. 6.7, 6.8, 6.9, and 6.10. Rietveld refinements were performed to determine the lattice paramters in each of these cases.
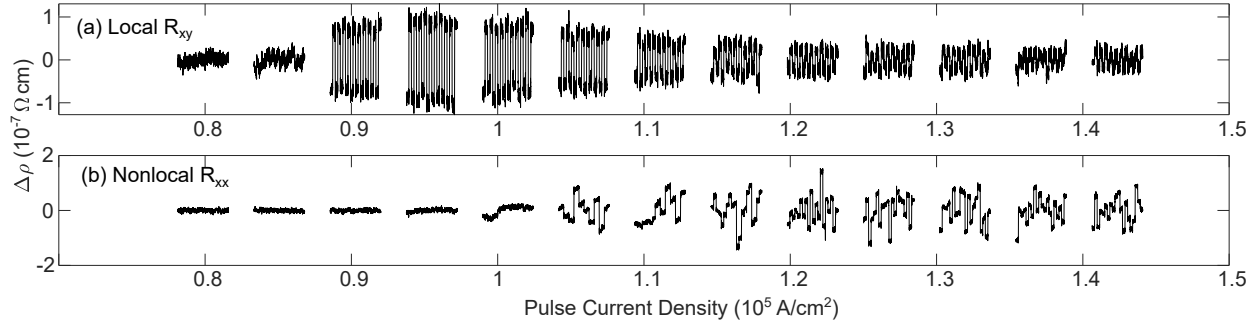
Figure 6.6: (a) Local switching measurement as a function of pulse current density observed with a device of $Fe_{0.33}NbS_2$. (b) Non-local longitudinal resistivity changes observed in the same device during the same switching events.

Full temperature dependence

Current density dependence was measured every $5K$ between 5 and $40K$ for local and non-local contacts. The responses in the non-local contacts are shown in 6.11, and 6.12. The responses in the local contacts are shown in Chapter 4, Figure 4.4.

Switching with lead detachment

Measurements were performed wherein the AC probe current was turned off and its leads were detached during the switch events. The leads were reattached and the probe current turned back on in order to measure the resistance between switching events. This is shown in Figs. 6.13 and 6.14. The non-local switching behavior persists, and its character does not change from that seen when the AC probe current is always on.

Probe current frequency dependence

The non-local switching behavior has no discernible dependence on the frequency of the AC probe current. See Fig. 6.15.

Schematic

A schematic view of the proposed mechanism for resistance switching is shown in Fig.6.16. Following a horizontal current pulse in a stripe-dominated sample, the domain with principal axis parallel to the current pulse is disfavored, resulting in a combination of the other two domain orientations, while the domain with principal axis perpendicular to the pulse is favored following a vertical current pulse. In a zigzag-dominated sample as well, current pulses
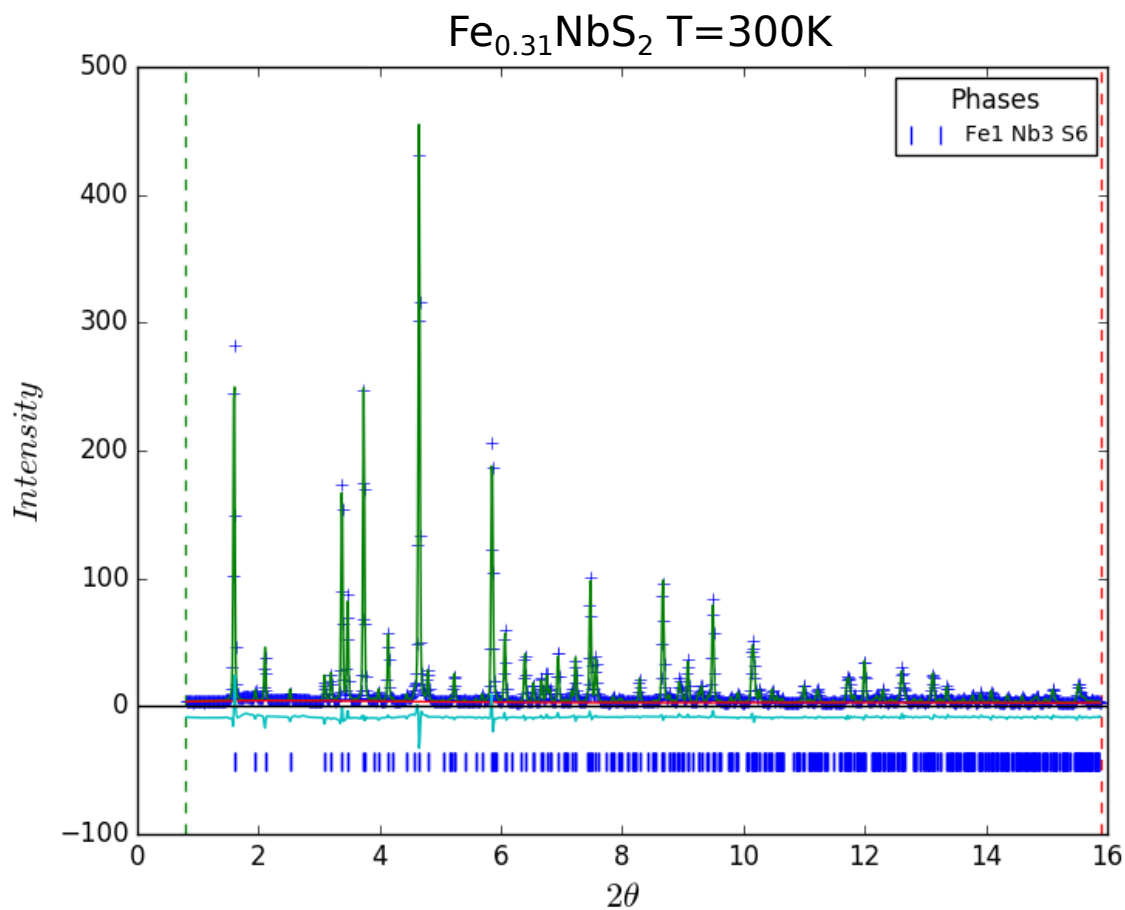
Figure 6.7: Rietveld refinement of high-resolution synchrotron powder XRD measurements on $Fe_{0.31}NbS_2$ at $300K$. Calculated lattice parameters are a = 5.662078 +/- 0.000137 Å, c = 11.964578 +/- 0.000302 Å. The cross markers are data with the fit shown by the green curve, and the difference between the fit and data is shown in cyan. Vertical lines denote structural peak positions.
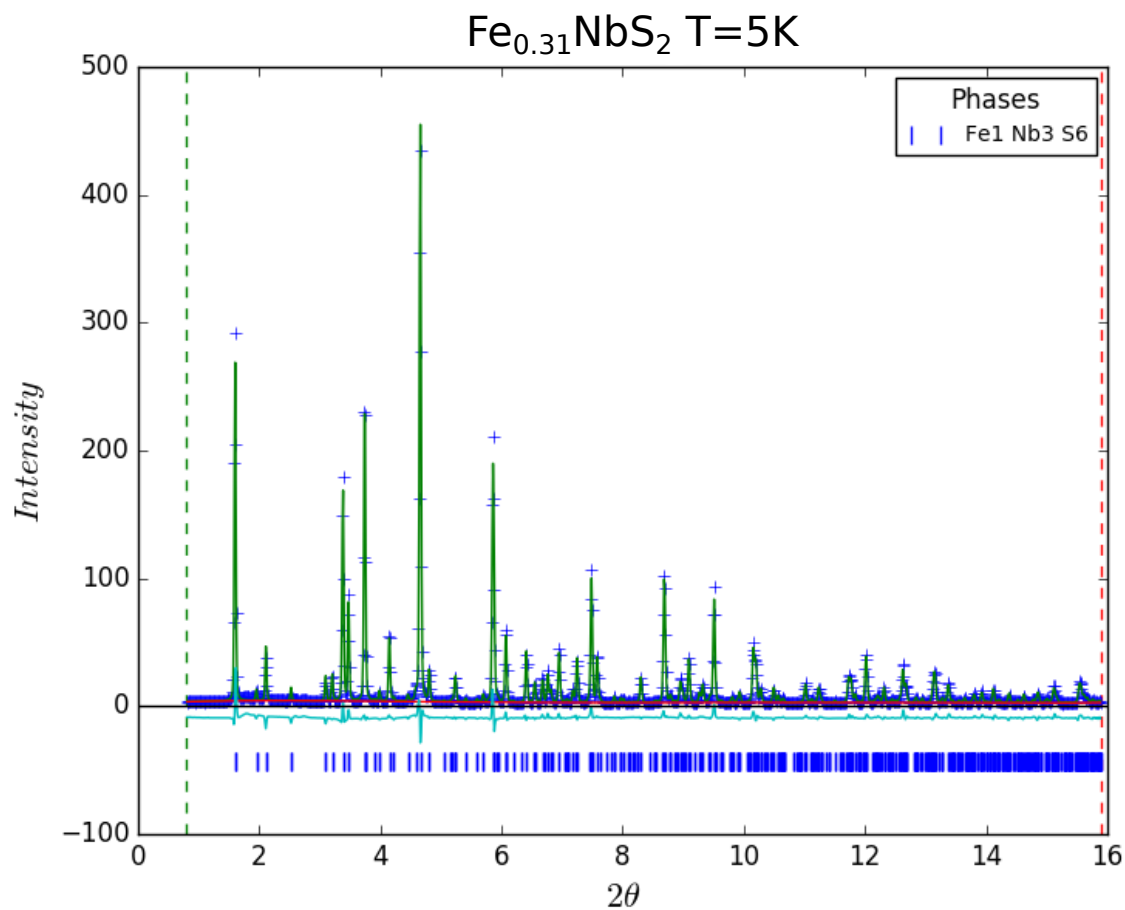
Figure 6.8: Rietveld refinement of high-resolution synchrotron powder XRD measurements on $Fe_{0.31}NbS_2$ at $5K$. Calculated lattice parameters are a= 5.654858 +/- 0.000182 Å, c=11.935061 +/- 0.000401 Å. The cross markers are data with the fit shown by the green curve, and the difference between the fit and data is shown in cyan. Vertical lines denote structural peak positions.
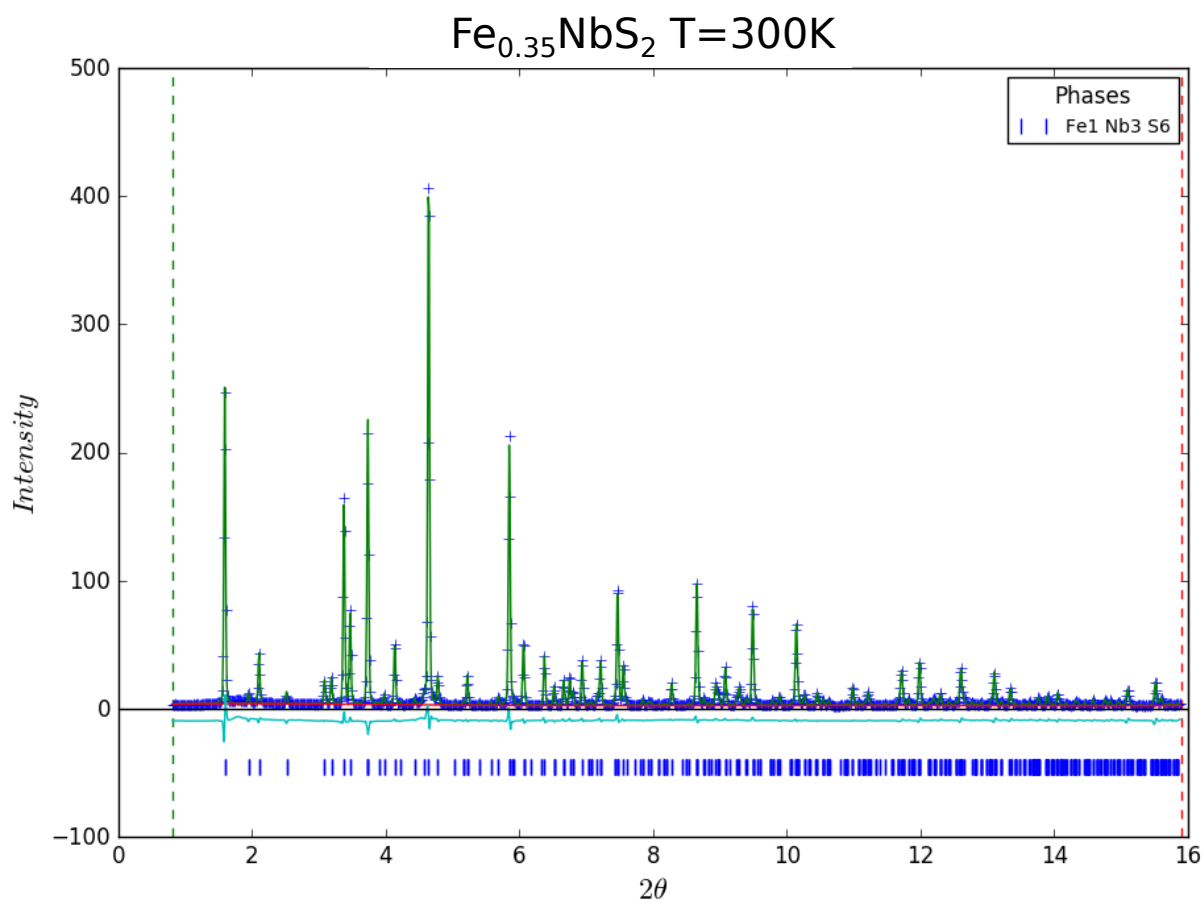
Figure 6.9: Rietveld refinement of high-resolution synchrotron powder XRD measurements on $Fe_{0.35}NbS_2$ at $300K$. Calculated lattice parameters are a=5.660797 +/- 0.000115 Å, c = 11.994610 +/-0.000260 Å. The cross markers are data with the fit shown by the green curve, and the difference between the fit and data is shown in cyan. Vertical lines denote structural peak positions.
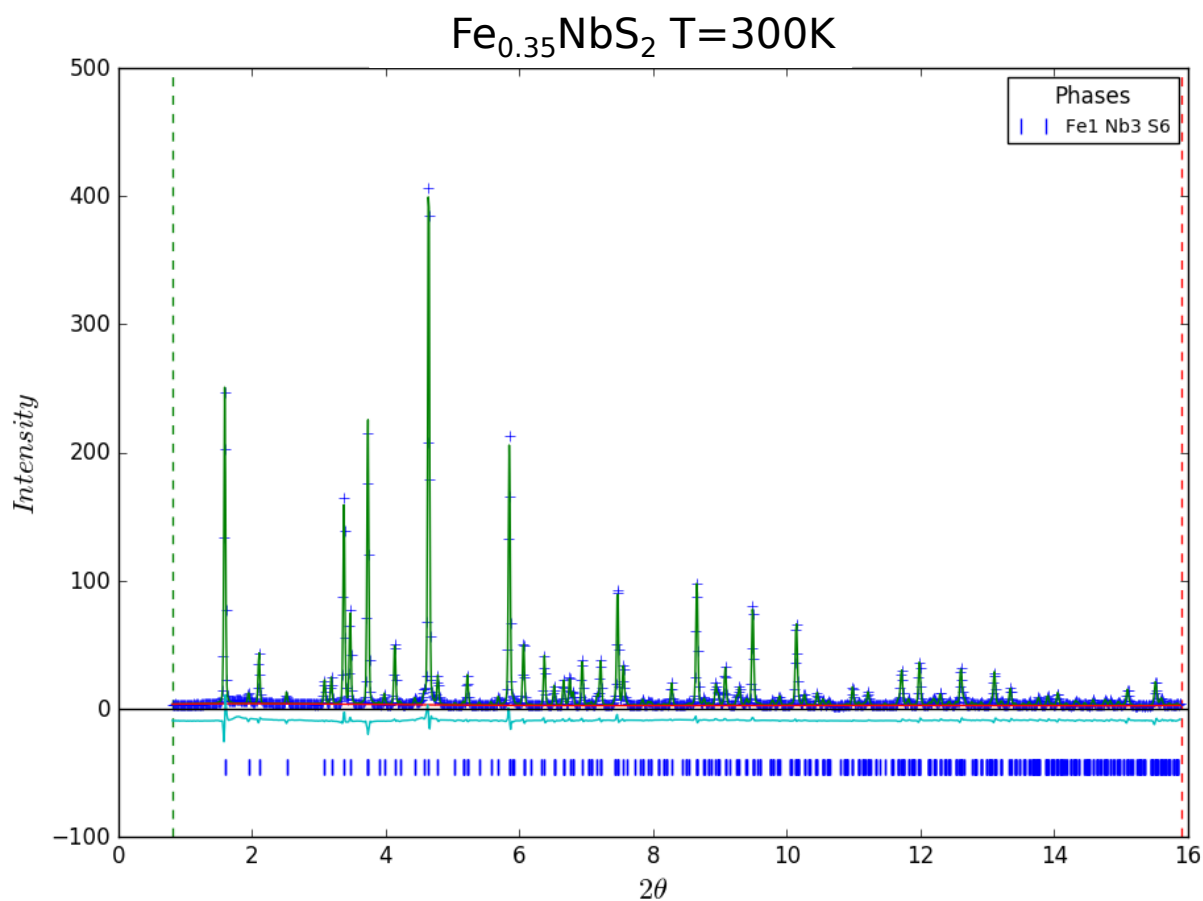
Figure 6.10: Rietveld refinement of high-resolution synchrotron powder XRD measurements on $Fe_{0.35}NbS_2$ at $10K$. Calculated lattice parameters are a=5.654070 +/- 0.000153 Å, c = 11.968898 +/-0.000296 Å. The cross markers are data with the fit shown by the green curve, and the difference between the fit and data is shown in cyan. Vertical lines denote structural peak positions.
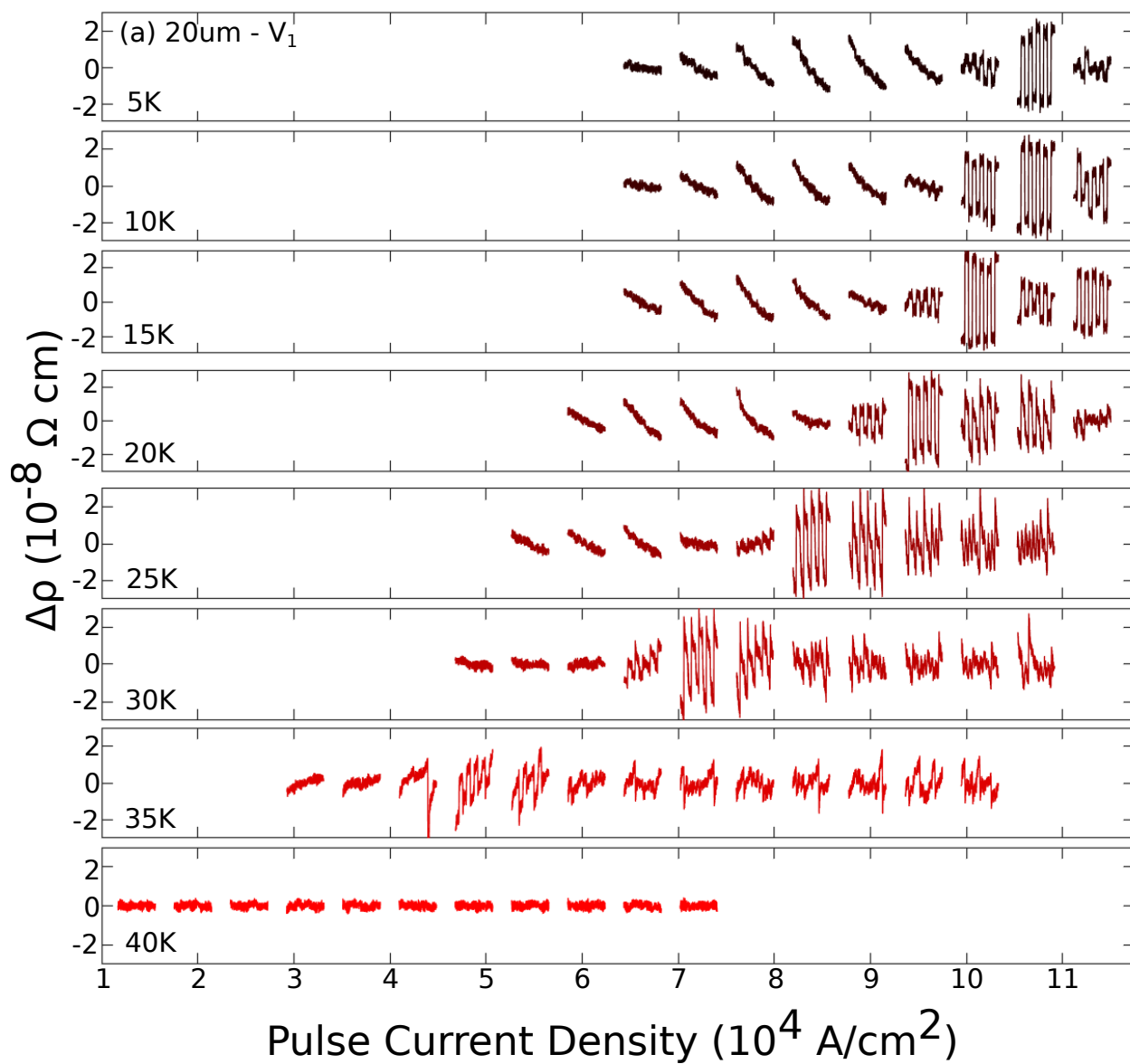
Figure 6.11: non-local ($20\mu m$ from the center of the device) switching measurement as a function of pulse current density, shown at temperatures from $5K$ to $40K$.
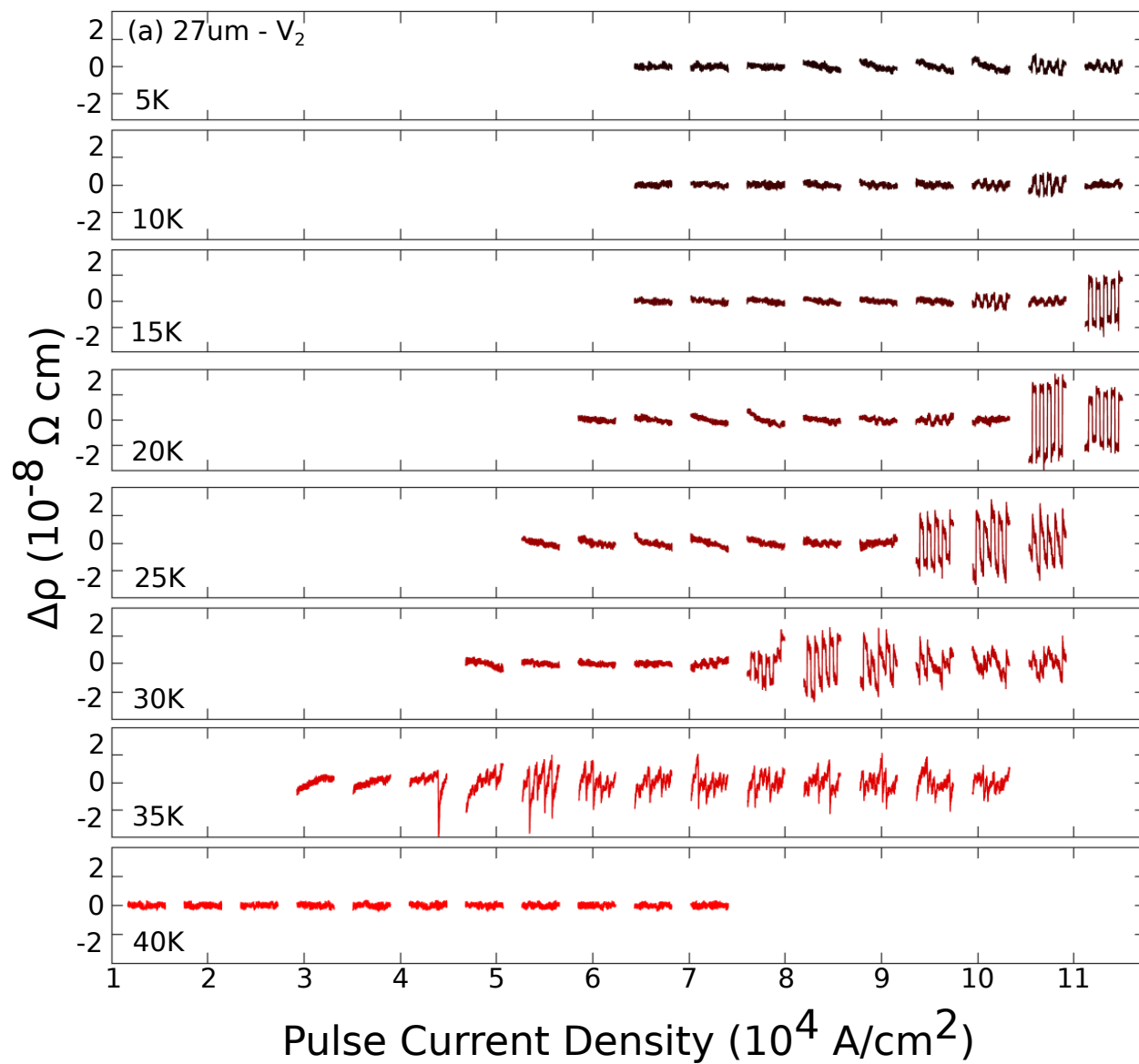
Figure 6.12: non-local ($27\mu m$ from the center of the device) switching measurement as a function of pulse current density, shown at temperatures from $5K$ to $40K$.
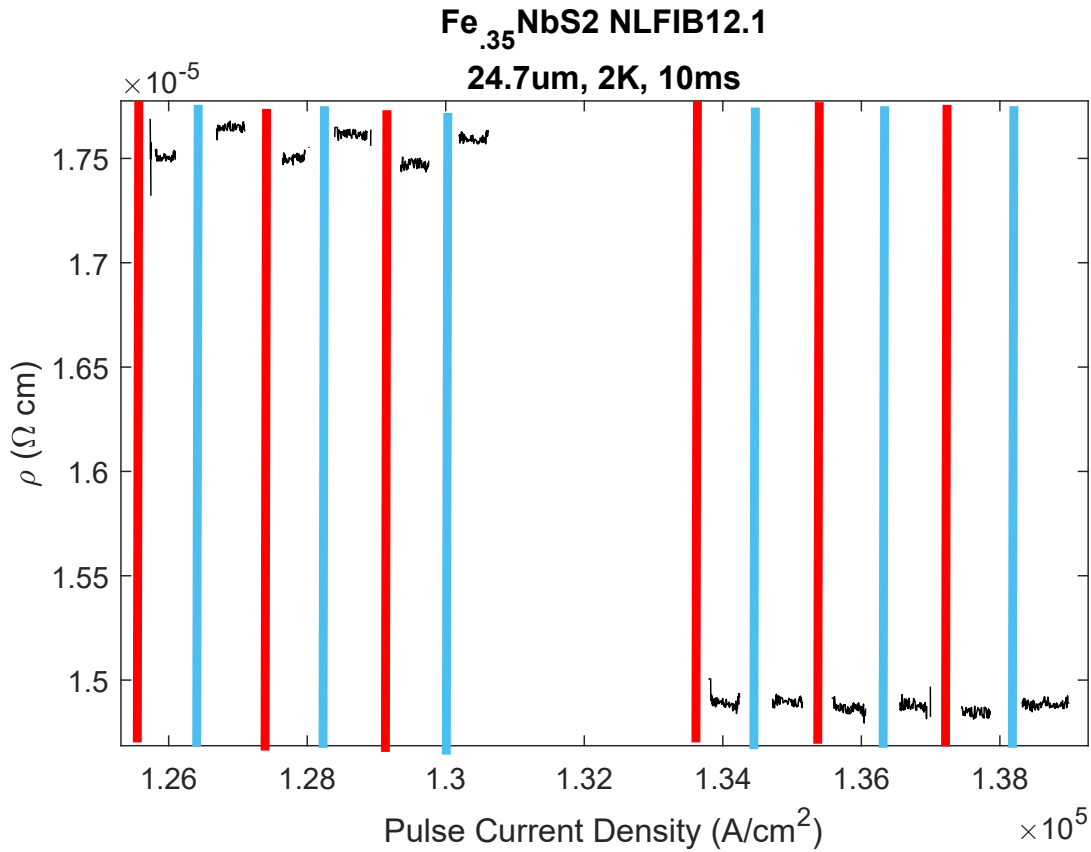
Figure 6.13: Switching measured $25\mu m$ from the center of a device at a current density that results in switching (left) and that does not result in switching (right), with the AC probe current turned off and its leads detatched during the switching events themselves. Vertical lines indicate switching events, and readouts from the lockins while the leads were detached have been omitted.

favor domains whose principal axes are not parallel to the pulse. The domain configurations in panels (c) and (e) have opposite conductivity anisotropies, as do those in panels (d) and (f) [126], so that (g) when stripe and zig-zag orders coexist, there will be competing switching responses, as shown schematically in (h). Note the similarity between the black curve in (h) and the observed signal in Fig. 6.4, with a small intitial response with an opposite sign flip to the main response, and a decreasing response after an initial peak.

More devices

There is some variation in switching response between devices, as their dimensions, exact concentrations, geometries, and mounting conditions vary slightly. See Figs. 6.17 and 6.18
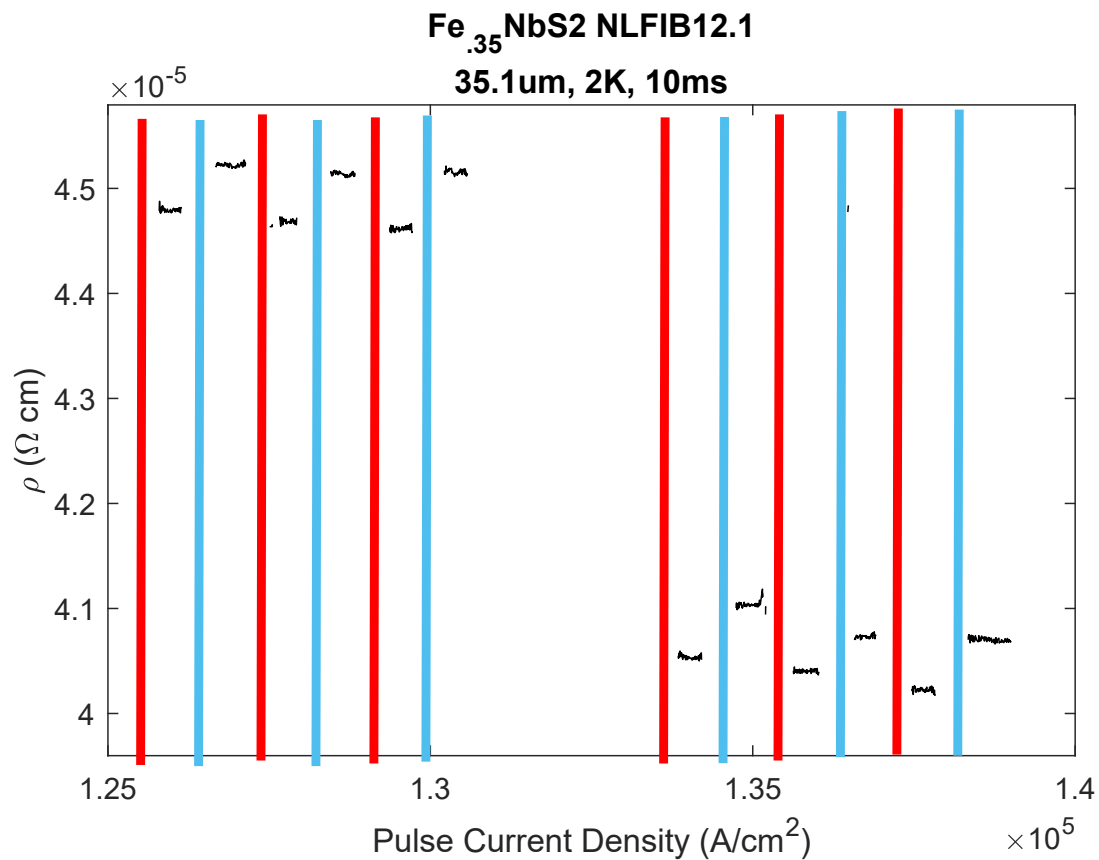
Figure 6.14: Switching measured $35\mu m$ from the center of a device at two different current densities that result in switching (left and right), with the AC probe current turned off and its leads detatched during the switching events themselves. Vertical lines indicate switching events, and readouts from the lockins while the leads were detached have been omitted.

for examples.
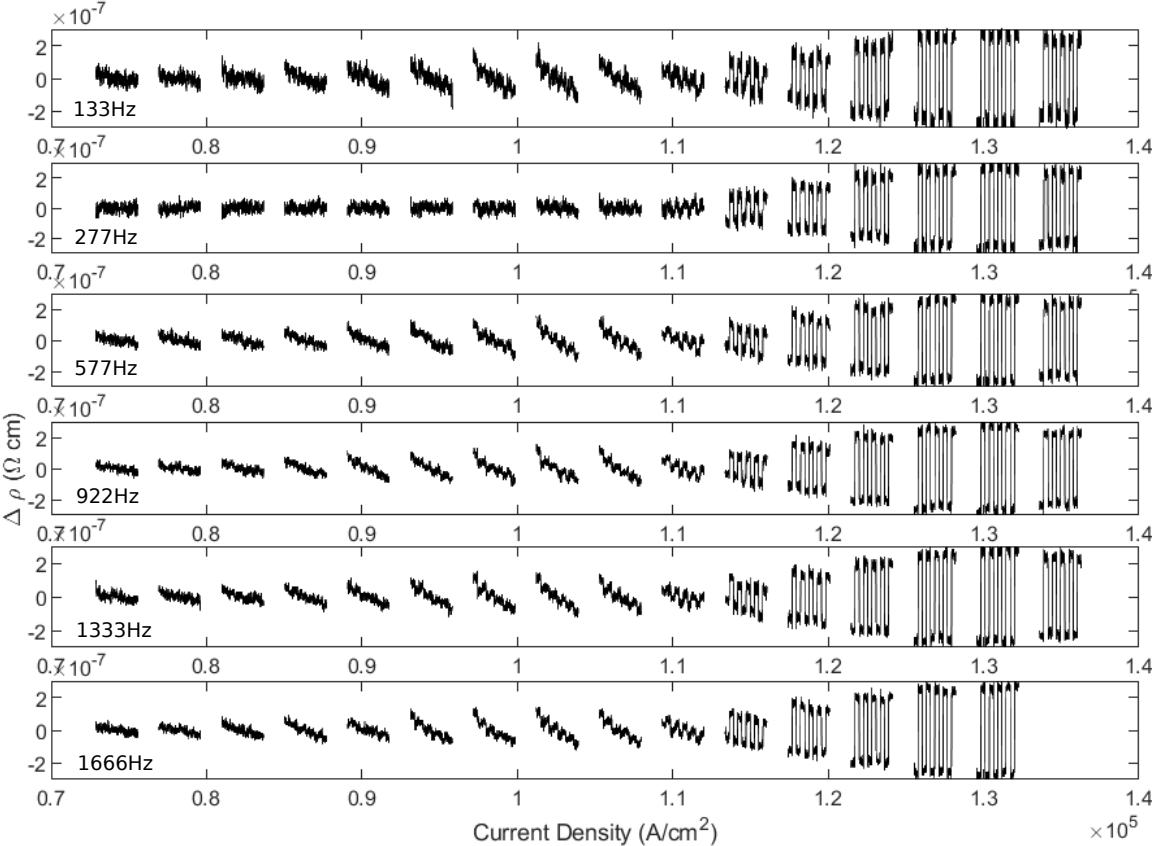
Figure 6.15: Switching measured $35\mu m$ from the center of a device at a current density that result in switching, with AC probe frequencies ranging from $133Hz$ to $1666Hz$. The noise changes from measurement to measurement, but the switching behavior notably does not.
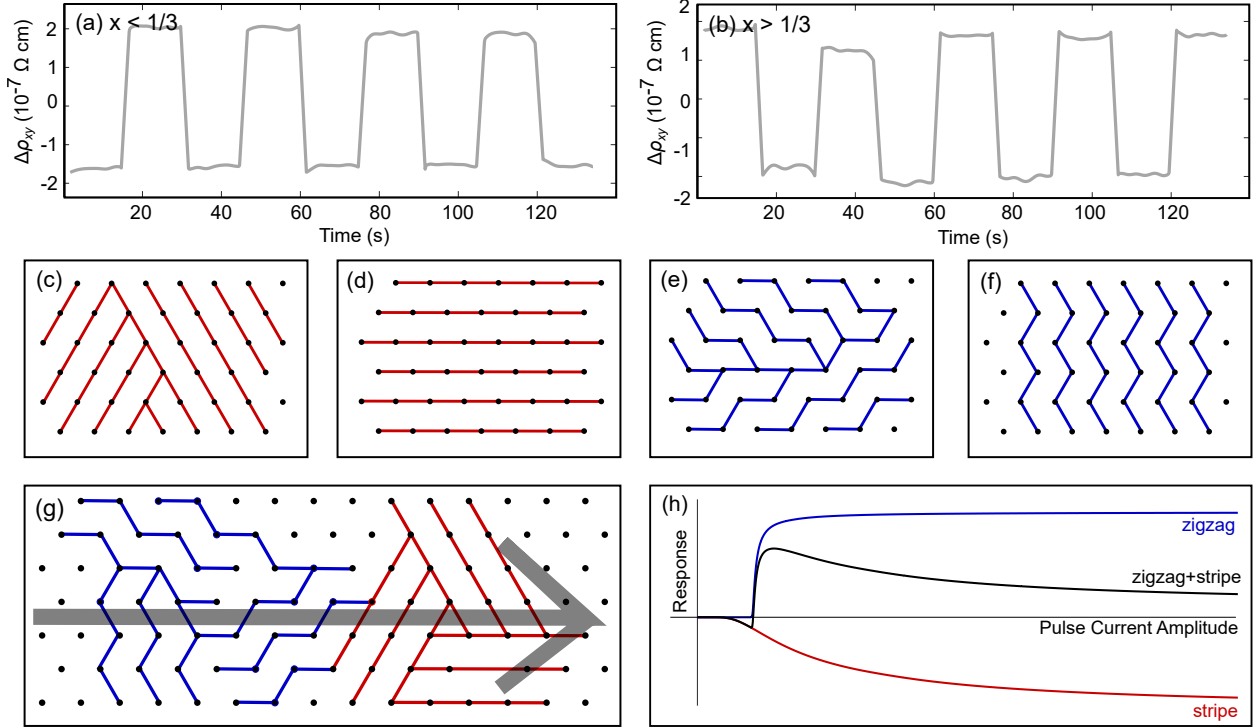
Figure 6.16: (a) Transverse resistance switching response in Fe_xNbS_2 with $x < 1/3$. Data were taken at $2K$, with pulse current amplitudes of approximately $15 \times 10^4 A/cm^2$, in the regime where switching has moved beyond the initial anomalous region as seen around $8.5 \times 10^4 A/cm^2$ in Fig.6.3A. In both cases, the first pulse and then every other subsequent pulse was normal to a crystal facet. (b) Transverse resistance switching response in Fe_xNbS_2 with $x > 1/3$. With identical device geometries, a pulse which brought $x < 1/3$ to a low resistance state brings $x > 1/3$ to a high resistance state, and vice versa. (c-f) Illustration of stripe and zigzag domains. Circles are iron atoms in one plane. Lines drawn between iron atoms indicate their spins are aligned. (c) Domain configuration preferred following a horizontal pulse in a stripe-dominated sample. (d) Domain configuration preferred following a vertical pulse in a stripe-dominated sample. (e) Domain configuration preferred following horizontal pulse in a zigzag-dominated sample. (f) Domain ocnfiguration preferred following vertical pulse in a zigzag-dominated sample. (h) Proposed combination of zigzag and stripe responses in zigzag-dominated sample. Note the similarity between the black curve and the observed signal in Fig. 6.4, with a small intitial response with an opposite sign flip to the main response, and a decreasing response after an initial peak.
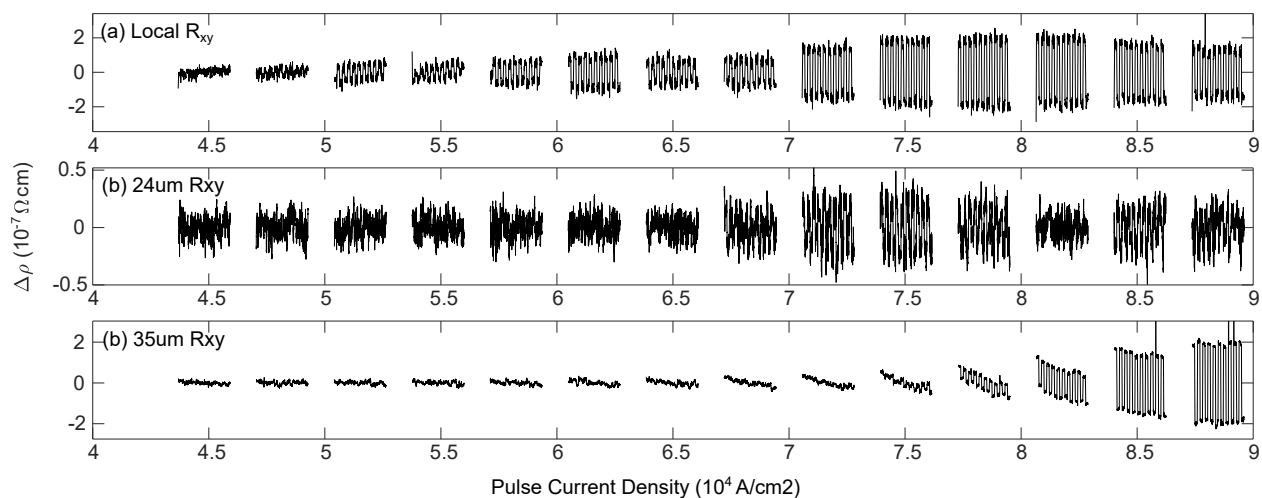
Figure 6.17: Switching response in a device with a different current density dependence than those shown in the main text. (a) Local response is nonmonotonic, showing a change in sign as a function of pulse current density. (b) $24\mu m$ from the center of the device, the non-local response is small but shows a change in sign as well. The first switching responses have an opposite sign to the first local switching responses. (c) $35\mu m$ from the center of the device, the non-local response is comparable to the maximum local response. Compared to the initial onset of switching in the local portion of the device, the response seen here is larger and has an opposite sign.
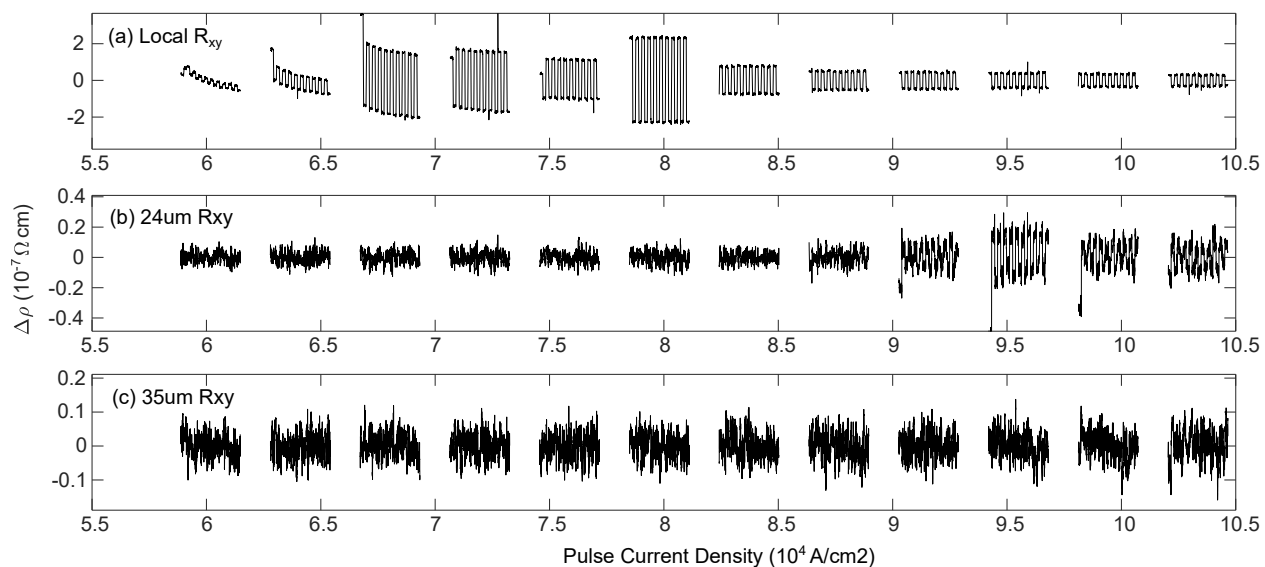
Figure 6.18: Switching response in a device with a different current density dependence than those shown in the main text. (a) Local response is nonmonotonic, showing two peaks followed by the decreasing amplitude characteristic of most devices. The presence of two peaks is suggestive of inhomogeneous iron content or a twist in the stack of layers. (b) $24\mu m$ from the center of the device, the non-local response is small but has a sign opposite that of the local response. (c) $35\mu m$ from the center of the device, a non-local response is not observed, presumably because the measurement did not extend to high enough current densities.

Chapter 7

Related Materials

"I would like to think that all of my successes in life are really just the fruit of my failures."
– Yvie Oddly

7.1   Introduction

As discussed in Chapter 1, Fe_xNbS_2 is just one of a large class of materials known as intercalated TMDs. Pulling from this broader class – and from the class of parent compounds, TMDs – can be a powerful tool for better understanding the properties of Fe_xNbS_2 by determining what changes lead to their loss or retention. Further, when it comes to switching behaviors, this broader class is a natural set of candidates for achieving larger amplitudes, enhanced stability, and most importantly higher temperatures. To these ends, two materials closely related to Fe_xNbS_2 are discussed here.

7.2   Cobalt-intercalated niobium disulfide

Introduction and Background

$Co_{1/3}NbS_2$ is structurally identical to $Fe_{1/3}NbS_2$, except for the inclusion of cobalt, rather than iron, atoms. The cobalt compound has a lower ordering temperature of $25K$ rather than $40K$, and is believed to have an easy-plane rather than easy-axis character. It is, however, an antiferromagnet, like the iron compound, and similarly can be stably grown at a range of intercalation concentrations.

At this time, there is debate in the field concerning the ground state of cobalt-intercalated niobium disulfide. While neutron scattering measurements suggest that it has a collinear in-plane order, the presence of an anomalous Hall effect - which some argue is topological in nature - points to a more complicated spin texture [127, 128].

A recent study found that the character and presence of the anomalous Hall effect depends strongly on the intercalation concentration of this material, with the AHE disappearing for
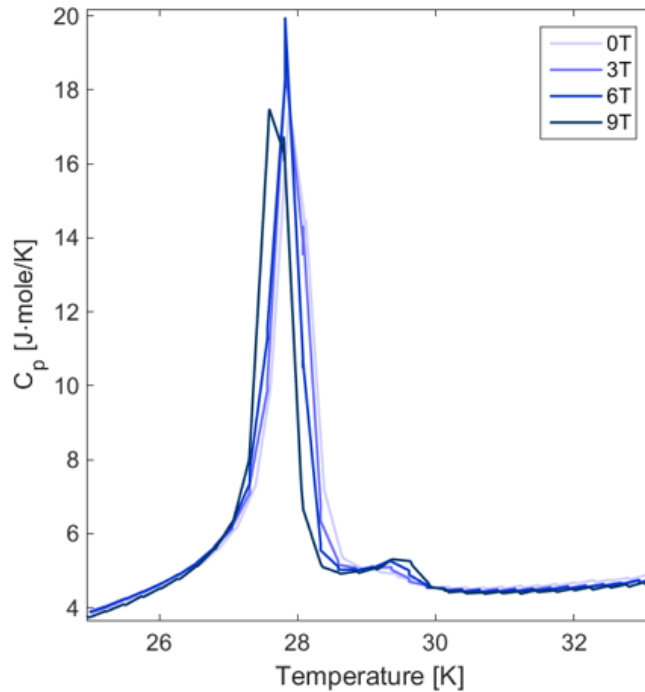
Figure 7.1: Heat capacity of $Co_{1/3}NbS_2$ as a function of temperature, measured under 0T, 3T, 6T, and 9T of applied magnetic field.

Co_xNbS_2 with $x > 1/3$ [129].

The disagreement over the ground state in this material, along with the disappearance with varying intercalation of the argument for one of those ground states, suggests the possibility of a similar sort of competition of orders to that seen in Fe_xNbS_2. Supporting this, the heat capacity of Co_xNbS_2 displays two peaks at zero-field, with the higher-field peak much smaller than the lower-field peak, as shown in Figure 7.1. This had not been previously observed, and is strongly reminiscent of the heat capacity of Fe_xNbS_2. In particular, this double-peak feature was found in the iron-intercalated system to be connected to competing orders with strengths that vary with iron content. This is especially interesting because competing orders in Co_xNbS_2 could explain seemingly conflicting findings in this system.

In order to interrogate the possibility of multiple antiferromagnetic orders in Co_xNbS_2 and how the coexistence of those orders might connect to the same in Fe_xNbS_2, high field measurements were conducted on the system as described in the following section.

High-field measurements

Magnetization as a function of applied magnetic field was measured at various temperatures on a stack of co-aligned $Co_{1/3}NbS_2$ crystals at the pulsed field facility in Los Alamos. The

results are summarized in Figure 7.2. $Co_{1/3}NbS_2$ lacks the plateaus and dramatic steps of $Fe_{1/3}NbS_2$, as should be expected given it lacks its sister compound's c-axis collinearity, but it does seem to retain some small step-like transitions at high applied magnetic fields. Unlike in $Fe_{1/3}NbS_2$, no steps are discernible at lower fields, at least in the pulsed magnetization measurements.

Electronic transport was also measured in high pulsed magnetic fields. The magnetic field was along the c-axis of the sample, while the probe current and measurement contacts were all arranged within the plane. Both longitudinal and transverse resistance were measured. Particular attention was paid to the temperature range in which the Anomalous Hall Effect has been observed in different samples of Co_xNbS_2, from about 16K to 30K [129]. While the zero-field hysteresis that has been observed before (in measurements up to 10T) wasn't observable in these measurements, possibly due to the noise around zero field and small size of those expected hysteresis loops, hysteretic transitions were observed at higher fields; shown in Figure 7.3 is a transition around 18.7T at 24K.

Figure 7.4 shows the locations of features identified in magentization and transport measurements. The transport data used to identify these points is found in Figure 7.3 and 7.8. There is largely agreement between the two measurements, although the edges of the transport hysteresis loops are at times difficult to precisely identify.

Conclusions regarding Co_xNbS_2

While evidence of coexisting phases in Co_xNbS_2 is not apparent from the high field data, there does seem to be a high-field phase that was not previously expected. This supports a microscopic picture of the interaction strengths in Co_xNbS_2 that is more similar to Fe_xNbS_2 than would perhaps be expected from the general variety of magnetic behaviors in this series of materials. More study is needed to identify or rule out multiple low-field transitions, as is seen in Fe_xNbS_2, and to determine the nature of the high-field phase observed here.

7.3   Tantalum disulfide

Introduction and Background

TaS_2 is a TMD which has been studied for, among other things, its memristive abilities. These abilities are based on the dramatically different resistances of the different phases of TaS_2, as shown in Figure 7.5 and involve moving between these phases via optical and electric stimuli [130–136]. The phases that TaS_2 hosts are three charge density wave (CDW) phases – a commensurate CDW, a nearly commensurate CDW, and an incommensurate CDW. These entail a distortion in of the tantalum atoms from an otherwise triangular lattice into stars of David. In the commensurate CDW phase, these fully tile the lattice. In the nearly commensurate phase, they tile hexagonal areas of the lattice, with starless regions between the hexagonal areas. When warming from the commensurate CDW, there is an intermediate
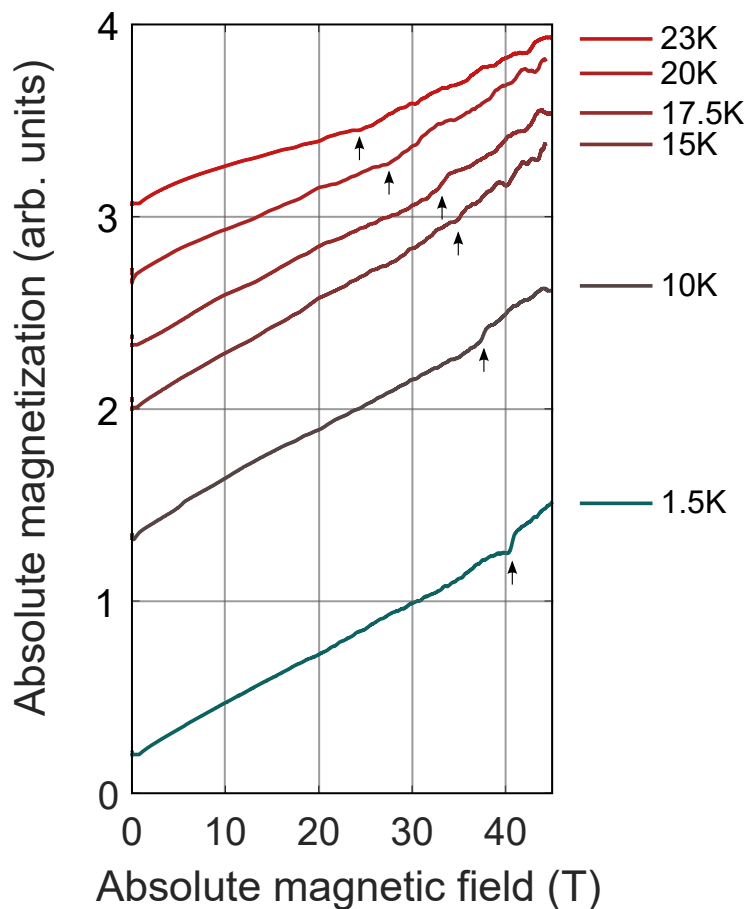
Figure 7.2: Magnetization as a function of applied magnetic field of $Co_{1/3}NbS_2$, taken at 24K. Additionally temperatures are included in the Appendix, Figure 7.8. Magnetization and applied field are both along the c-axis. Curves are offset for visibility, and labeled with their respective temperatures. Arrows mark jumps that may be associated with a phase transition. 15K, 17.5K, and 20K were taken with the field pointing in the opposite direction to that of the other temperatures; magnetization and field are presented as their absolute value. The pulsed field measurement includes both a rising portion (from 0 field to the maximum field) and a falling portion (from the maximum field back to 0 field), of which the faster rising portion is less noisy for these measurements, whose raw signal is proportional to the time derivative of the magnetization. Presented here are those rising portions.
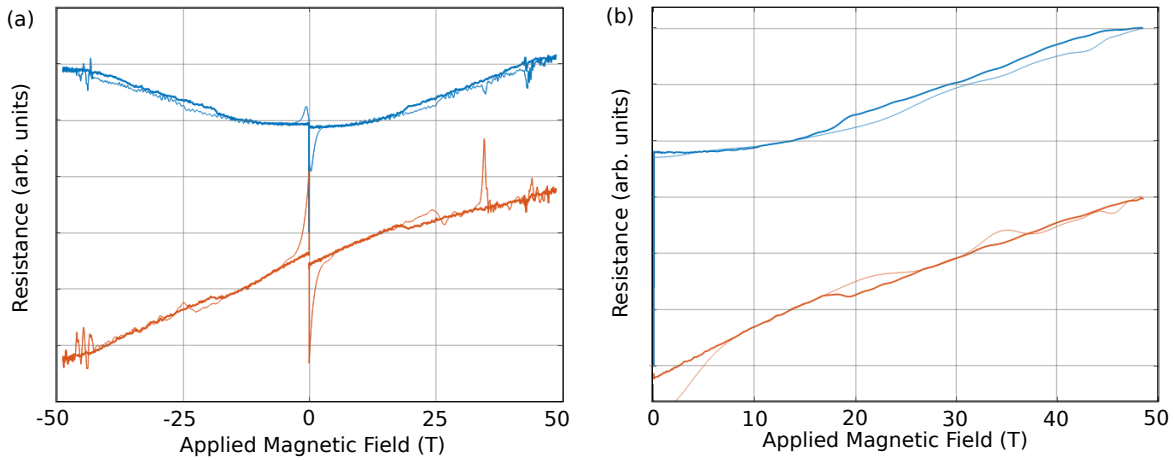
Figure 7.3: Resistance (top curve) and transverse resistance (bottom curve) of $Co_{1/3}NbS_2$, measured in high field. The pulsed field measurement includes both an rising portion (from 0 field to the maximum field) and a falling portion (from the maximum field back to 0 field), of which the slower falling portion is less noisy for these lock-in measurements. Presented here are both portions, with the faster rising portion indicated with a thinner line. (a) Raw data, collected for both positive and negative applied fields. (b) The data in (a), with the resistance symmetrized in field and the transverse resistance antisymmetrized in field. The curves are additionally smoothed in this plot to better highlight the step-like features, which are also visible in the raw data.

nearly-commensurate triclinic CDW phase, in which the stars form a stripe pattern. The incommensurate CDW phase involves a distortion of the lattice which is sufficient to make the material, which is metallic between 543K and 600K, an insulator [137].

Notably, the manipulations that cause movement between these phases include the application of an in-plane electric current [133]. Presented here are data suggesting that TaS_2 can further be manipulated nematically through the application of electric current in different directions within the plane, changing the anisotropy of the conductivity rather than just its magnitude.

Switching Response

The device geometry is shown in Figure 7.6 (a) and (b). The same pulse application protocol is used as that described in Chapter 4: a brief current pulse is applied along the bar marked A, 30 seconds pass, a brief current pulse is applied along the bar marked B, 30 seconds pass, and this process is repeated 9 times. To measure the switching response, an AC probe current is run along one of the pulse bars, and the longitudinal resistance is measured with a lock-in amplifier. The device geometry differs slightly from that described in Chapter 4.
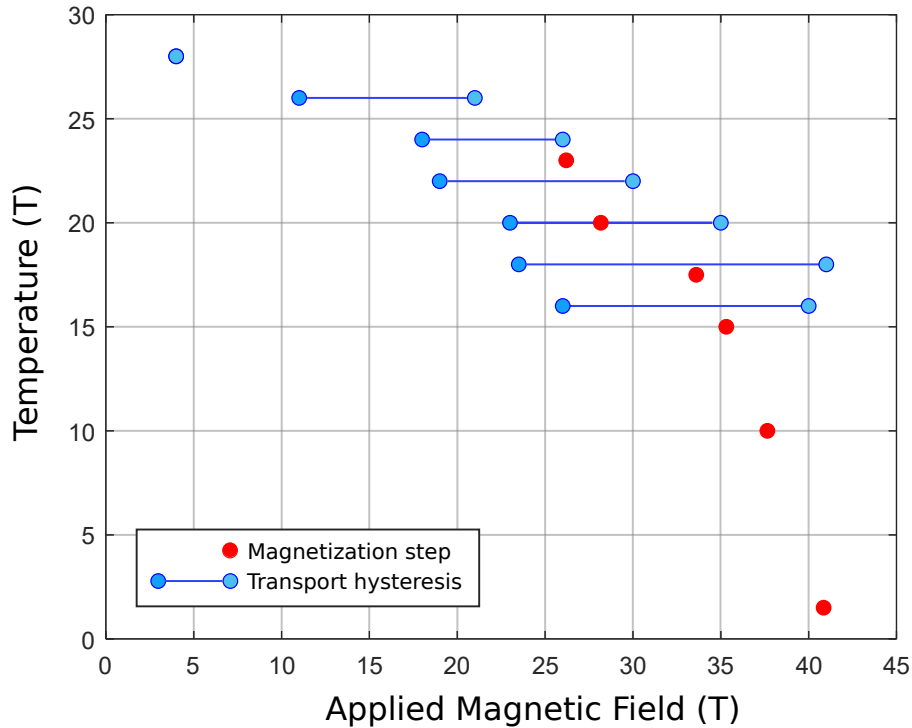
Figure 7.4: Locations of features in high field measurements of $Co_{1/3}NbS_2$. Indicated are steps in magnetization measurements, and edges of hysteresis loops in transport measurements, where they are discernible.

The measurement contacts meet the pulse bar on either side of where the pulse bars cross each other, and gold is left intact on top of the device at this spot. This is to ensure that the resistance through the active area of the device is measured as fully as possible, and to avoid, for example, spurious effects of inhomogeneity of the cross-section of the pulse bars. The results can be seen in Figure 7.6 (c) and (d), with each corresponding to the setup to its left. An A pulse leads to lower resistance in the direction of the A pulse, and higher resistance in the direction of the B pulse, and vice versa. This suggests that the directional switching response is truly due to a rotation of the conductivity tensor, rather than a uniform raising and lowering of the conductivity.

Figure 7.7 shows the pulse current and history dependence of the switching response in TaS_2. First, it should be noted that the directional switching response seems to grow monotonically and saturate, unlike the nonmonotonic response observed in Fe_xNbS_2 and described in Chapter 4. Second, the switching response decreases in amplitude with shorter pulse durations. And third, the directional switching never brings the system higher than its original (commensurate CDW) resistance, and occurs on a background of non-directional switching, whereby: starting in the commensurate CDW state, the application of low density pulses
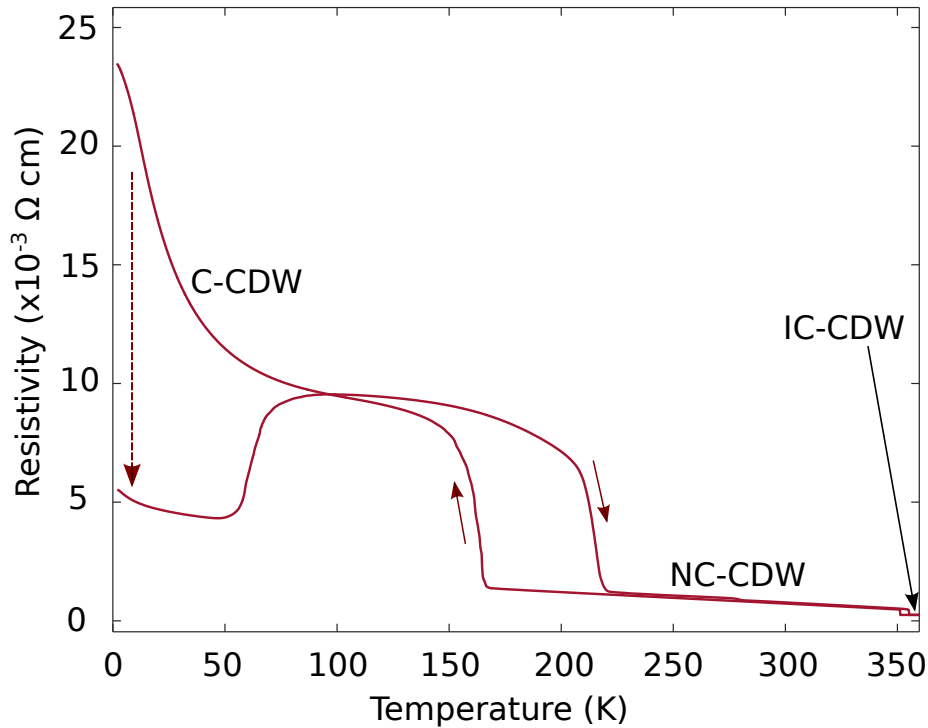
Figure 7.5: Resistivity as a function of temperature of a TaS_2 device. The curve on cooldown is characteristic of the resistance of $1T\text{-}TaS_2$, with a transition from incommensurate charge density wave (IC-CDW) to nearly commensurate charge density wave (NC-CDW) at about 350K, and another transition from NC-CDW to commensurate charge density wave (C-CDW) at 165K. After cooldown and before warmup, switching measurements (described in this section) were conducted on the device, bringing it to a lower resistance state. On warmup, the resistance rises and then falls, transitioning to the NC-CDW state at 218K and the IC-CDW at 355K.

does not move the resistance while the application of high density pulses lowers it, and starting from a lowered-resistance state, the application of low density pulses raises the resistance while the application of high density pulses again lowers it.

Conclusions regarding TaS_2

The data presented here suggest that the application of an in-plane current alters the electronic structure of TaS_2 in a way that goes beyond simply moving between phases, establishing a previously-unobserved in-plane anisotropy to the conductivity of this material. While this response bears some similarities to that in $FeNbS_2$, it importantly does not have the nonmonotonic behavior with increasing pulse current density seen in that system, suggesting that the mechanism at play is coupling to one order parameter, or at least to one anisotropic

order parameter, as would naively be expected. The directional switching does not seem to strengthen the commensurate CDW, based on it not raising the resistance over its initial value. Additionally, the amplitude of the directional switching grows as the background resistance indicates the system is being brought closer to the nearly commensurate CDW state. These facts suggest that the nearly commensurate CDW is the order parameter that is being manipulated in an anisotropic way via perpendicular current pulses. It is possible that this is done by changing the arrangement of the hexagonal star of David clusters, or by creating and directing the stripes of the triclinic CDW. The true microscopic picture is unclear at this point, and is worth further study.

7.4   Appendix I: Additional Data

This section provides additional data that was not included in the above sections.
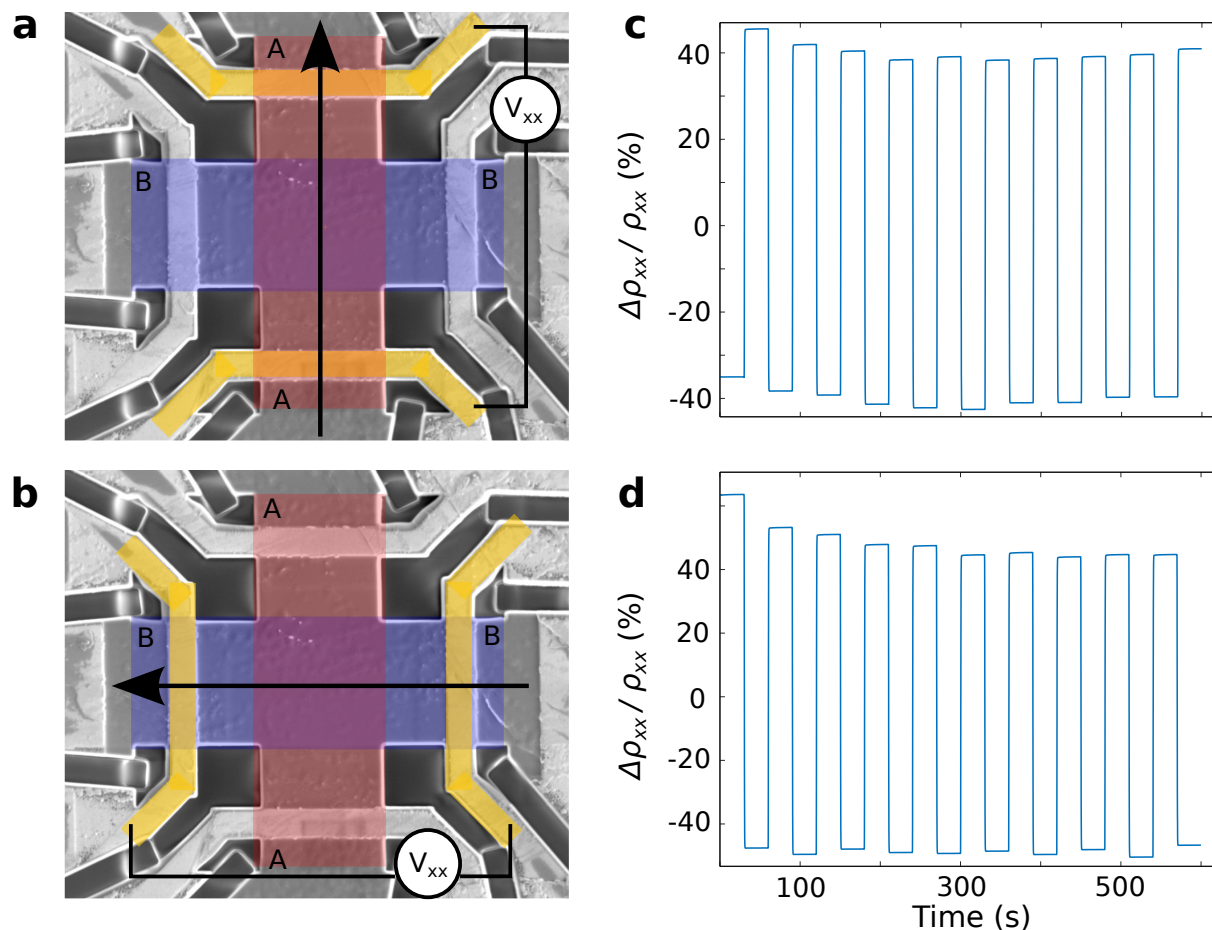
Figure 7.6: Switching response of TaS$_2$. (a, b) Diagrams of the switching measurement are overlaid on an SEM image of the device. The A and B pulse bars are labeled as such and highlighted in red and blue, respectively. The AC probe current direction is indicated with an arrow. The measurement contacts are highlighted in yellow, and labeled to show that voltage is measured between them. (a) The probe current and voltage measurement are both along the A pulse bar. (b) The probe current and voltage measurement are both along the B pulse bar. (c, d) The switching response to a series of 20 pulses, alternating between A and B and starting with A. The response is presented as the difference between the resistivity and the average resistivity, normalized by the average resistivity. The measurements were both taken with 10mA, 10ms pulses at 2K. (c) The response corresponding to the setup shown in (a), with the probe current and measurement along the A bar. (d) The response corresponding to the setup shown in (b), with the probe current and measurement along the B bar.
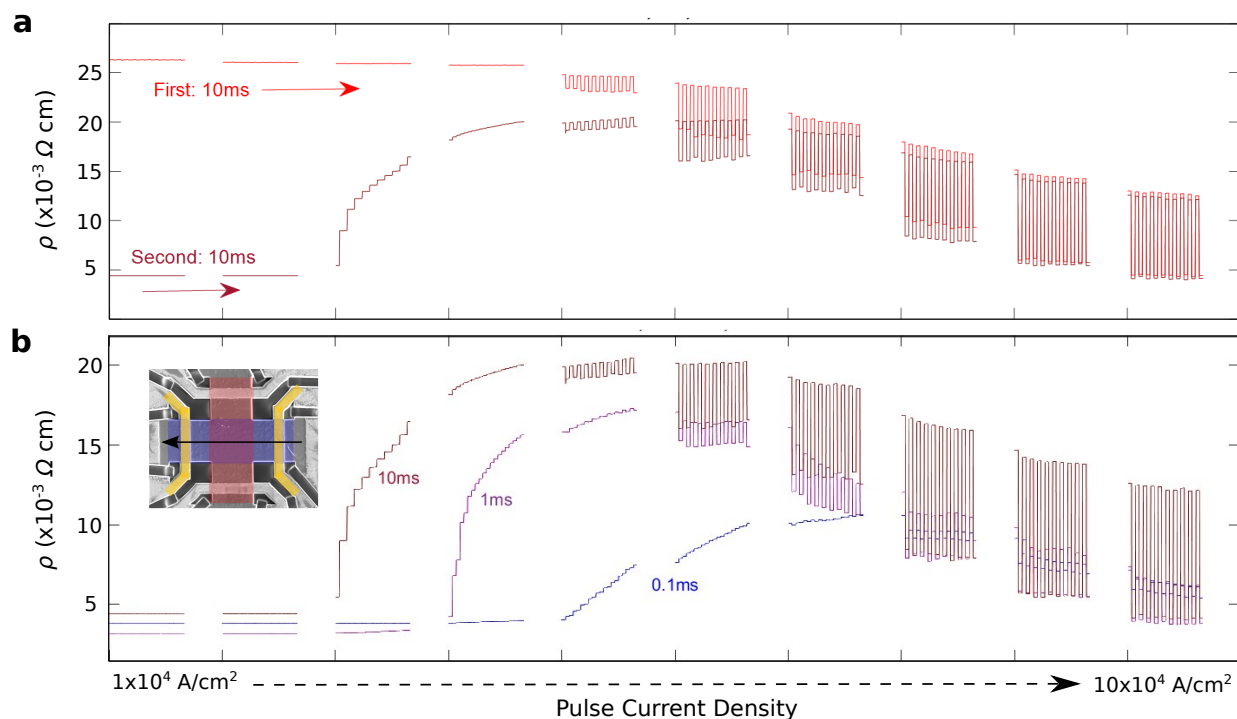
Figure 7.7: Pulse current and history dependence of switching response in TaS$_2$. Both plots show the switching response at 2K with no subtraction of the background resistance. (a) Pulse trains were applied with increasing current density, starting around $1 \times 10^4 A/cm^2$ and ending around $10 \times 10^4 A/cm^2$, and all pulses had a duration of 10ms. This was done first directly after cooling from room temperature (labeled 'First: 10ms'), and then repeated without changing the temperature (labeled 'Second: 10ms'). (b) Pulse trains were again applied with increasing current density, starting around $1 \times 10^4 A/cm^2$ and ending around $10 \times 10^4 A/cm^2$. This was done for three different pulse durations (labeled on the plot according to their duration: 10ms, 1ms, and 0.1ms). Each set of measurements was taken after switching pulses had already brought the device to a low resistance state, as can be seen by the starting resistivities around $4 \times 10^{-3}\Omega cm$. Inset: diagram of the measurement geometry used for the data presented in both (a) and (b) of this figure.
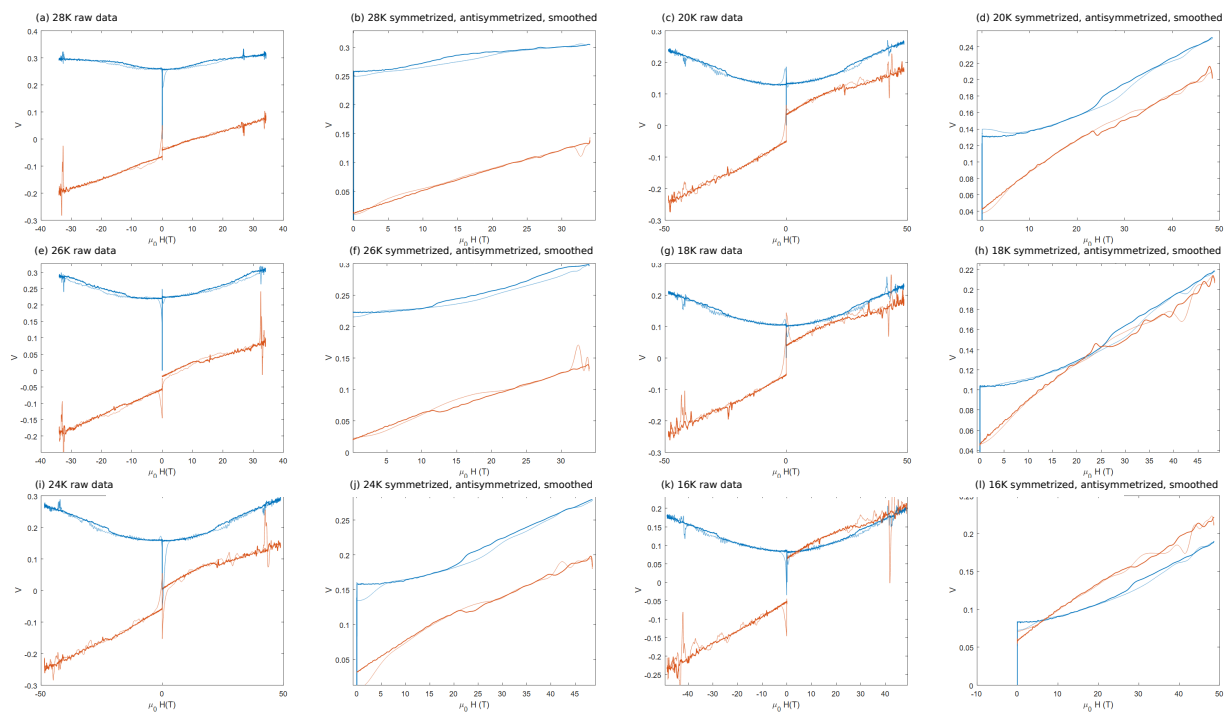
Figure 7.8: Full dataset of high field transport measurements on Co_xNbS_2. Identification of the edges of the hysteresis loops in these measurements was used to generate Figure 7.4.

Chapter 8

Conclusions and Outlook

"Do we have to put quotes in our thesises?"

– Yuanqi Lyu

This work has explored the relationship between frustration, disorder, and strain, primarily in iron-intercalated niobium disulfide. A significant portion of this exploration has been both motivated by and enabled by the peculiar response that this system has to electrical stimulus. Further work is currently being conducted to test and expand upon the conclusions presented here via scanning measurements on switching devices. Beyond this, there are two major branches of further inquiry that present themselves at this juncture.

First, how might the properties of Fe_xNbS_2 – both its switching ability and its coexisting phases and their strong strain dependence – translate to related systems? Some preliminary work has been done on Co_xNbS_2 and on TaS_2, which is briefly summarized in Chapter 7. More work is needed to conclusively explore the strain-dependence and possibility of coexisting orders in Co_xNbS_2, and the switching behavior of TaS_2. Beyond that, there is a huge space of intercalated TMDs to explore. This exploration has the potential both to uncover fundamental drivers of the unusual behaviors and properties observed in Fe_xNbS_2, and to bring the switching functionality to room temperature. Especially promising in this is intercalated WSe_2, although its growth has proven to be particularly challenging, as discussed in Chapter 2.

Second, how might switching measurements serve as an aide in studying the underlying properties of materials more generally? Different switching signs in Fe_xNbS_2 hinted at different dominant orders, and nonlocal responses to switching stimuli supported the existence of strong magnetoelastic coupling. Nonlocal devices were fabricated but nonlocal responses were not seen, on the other hand, in TaS_2, which does show a local switching response. In a non-TMD layered AFM system with broken inversion symmetry, local switching devices were fabricated but switching was not observed. Moving forward, as switching behaviors are characterized and studied for more materials, this measurement can perhaps be used not just towards the end of a potential application, but also more explicitly as an additional

means of probing order and its causes – especially in systems which are otherwise difficult to probe, as has been the case with the c-axis antiferromagnet Fe_xNbS_2.

Bibliography

[1]   S. Haley, "Half-magnetization plateau and the origin of threefold symmetry break-
        ing in an electrically switchable triangular antiferromagnet," *Phys. Rev. Res*, vol. 2,
        p. 043020.

[2]   S. C. Haley, E. Maniv, T. Cookmeyer, S. Torres-Londono, M. Aravinth, J. Moore,
        and J. G. Analytis, "Long-range, non-local switching of spin textures in a frustrated
        antiferromagnet," 2021.

[3]   *See Supplemental Material for (A) details of the spin-wave calculuation and (B)
        unabridged magnetization measurements and other experimental details.*

[4]   S. Parkin and R. Friend, "3d transition-metal intercalates of the niobium and tantalum
        dichalcogenides. I. Magnetic properties," *Philosophical Magazine B*, vol. 41, no. 1,
        pp. 65–93, 1980.

[5]   S. Blundell, *Magnetism in Condensed Matter*. Oxford University Press, 2001.

[6]   D. Ralph and M. Stiles, "Spin transfer torques," *Journal of Magnetism and Magnetic
        Materials*, vol. 320, no. 7, pp. 1190–1216, 2008.

[7]   J. Železný, H. Gao, A. Manchon, F. Freimuth, Y. Mokrousov, J. Zemen, J. Mašek,
        J. Sinova, and T. Jungwirth, "Spin-orbit torques in locally and globally noncentrosym-
        metric crystals: Antiferromagnets and ferromagnets," *Phys. Rev. B*, vol. 95, p. 014403,
        Jan 2017.

[8]   N. L. Nair, E. Maniv, C. John, S. Doyle, J. Orenstein, and J. G. Analytis, "Electri-
        cal switching in a magnetically intercalated transition metal dichalcogenide," *Nature
        Materials*, pp. 1–5, Nov. 2019.

[9]   I. Fina, X. Marti, D. Yi, J. Liu, J. H. Chu, C. Rayan-Serrao, S. Suresha, A. B. Shick,
        J. Železný, T. Jungwirth, J. Fontcuberta, and R. Ramesh, "Anisotropic magnetoresis-
        tance in an antiferromagnetic semiconductor," *Nature Communications*, vol. 5, p. 4671,
        Sept. 2014. Number: 1 Publisher: Nature Publishing Group.

[10] R. H. Friend, A. R. Beal, and A. D. Yoffe, "Electrical and magnetic properties of some first row transition metal intercalates of niobium disulphide," *The Philosophical Magazine: A Journal of Theoretical Experimental and Applied Physics*, vol. 35, pp. 1269–1287, May 1977.

[11] S. Parkin and R. Friend, "3d transition-metal intercalates of the niobium and tantalum dichalcogenides. II. Transport properties," *Philosophical Magazine B*, vol. 41, no. 1, pp. 95–112, 1980.

[12] N. Sirica, P. Vilmercati, F. Bondino, I. Pis, S. Nappini, S.-K. Mo, A. V. Fedorov, P. K. Das, I. Vobornik, J. Fujii, L. Li, D. Sapkota, D. S. Parker, D. G. Mandrus, and N. Mannella, "The nature of ferromagnetism in the chiral helimagnet Cr1/3NbS2," *Communications Physics*, vol. 3, pp. 1–8, Apr. 2020. Number: 1 Publisher: Nature Publishing Group.

[13] A. Y. Barkov, R. F. Martin, Y. P. Men'shikov, Y. E. Savchenko, Y. Thibault, and K. V. O. Laajoki, "Edgarite, FeNb3S6, first natural niobium-rich sulfide from the Khibina alkaline complex, Russian Far North: evidence for chalcophile behavior of Nb in a fenite," *Contributions to Mineralogy and Petrology*, vol. 138, pp. 229–236, Mar. 2000.

[14] P. Kumar, R. Skomski, and R. Pushpa, "Magnetically Ordered Transition-Metal-Intercalated WSe2," *ACS Omega*, vol. 2, pp. 7985–7990, Nov. 2017. Publisher: American Chemical Society.

[15] J. Kools, "Exchange-biased spin-valves for magnetic storage," *IEEE Trans. Magn*, vol. 32, p. 3165–3184.

[16] X. He, "Robust isothermal electric control of exchange bias at room temperature," *Nat. Mater*, vol. 9, p. 579–585.

[17] W. Meiklejohn and C. Bean, "New magnetic anisotropy," *Phys. Rev*, vol. 102, p. 1413–1414.

[18] H. Ohldag, "Correlation between exchange bias and pinned interfacial spins," *Phys. Rev. Lett*, vol. 91, p. 017203.

[19] I. Schuller, R. Morales, X. Batlle, U. Nowak, and G. Güntherodt, "Role of the antiferromagnetic bulk spins in exchange bias," *J. Magn. Magn. Mater*, vol. 416, p. 2–9.

[20] M. Kiwi, "Exchange bias theory," *J. Magn. Magn. Mater*, vol. 234, p. 584–595.

[21] P. Miltényi, "Diluted antiferromagnets in exchange bias: proof of the domain state model," *Phys. Rev. Lett*, vol. 84, p. 4224–4227.

[22] M. Ali, "Exchange bias using a spin glass," *Nat. Mater*, vol. 6, p. 70–75.

[23] S. Giri, M. Patra, and S. Majumdar, "Exchange bias effect in alloys and compounds," *J. Phys. Condens. Matter*, vol. 23, p. 073201.

[24] L. Barnsley, E. Gray, and C. Webb, "Asymmetric reversal in aged high concentration cumn alloy," *J. Phys. Condens. Matter*, vol. 25, p. 086003.

[25] M. Hudl, R. Mathieu, and P. Nordblad, "Tunable exchange bias in dilute magnetic alloys—chiral spin glasses," *Sci. Rep*, vol. 6, p. 19964.

[26] K. Fischer and J. Hertz, *Spin Glasses (Cambridge Studies in Magnetism*, vol. 1. Cambridge Univ. Press.

[27] J. Mydosh, *Spin Glasses: An Experimental Introduction.* CRC Press.

[28] S. Nagata, P. Keesom, and H. Harrison, "Low-dc-field susceptibility of cumn spin glass," *Phys. Rev. B*, vol. 19, p. 1633–1638.

[29] K. Binder and A. Young, "Spin glasses: experimental facts, theoretical concepts, and open questions," *Rev. Mod. Phys*, vol. 58, p. 801–976.

[30] C. Dekker, A. Arts, H. Wijn, A. Duyneveldt, and J. Mydosh, "Activated dynamics in a two-dimensional ising spin glass: Rb 2cu1xcoxf4," *Phys. Rev. B*, vol. 40, p. 11243–11251.

[31] G. Parisi, "Order parameter for spin glasses," *Phys. Rev. Lett*, vol. 50, p. 1946–1948.

[32] B. Van Laar, H. M. Rietveld, and D. J. W. Ijdo, "Magnetic and crystallographic structures of MexNbS2 and MexTaS2," *Journal of Solid State Chemistry*, vol. 3, pp. 154–160, May 1971.

[33] Y. Suzuki, T., Ikeda, S., Richardson, J.W., Yamaguchi, "Magnetic Structure of $Fe_{1/3}NbS_2$," in *Proceedings of the Fifth International Symposium on Advanced Nuclear Energy Research*, pp. 343–346, 1993.

[34] N. Doi and Y. Tazuke, "Spin glass phases in 2h-fexnbs2," *J. Phys. Soc. Jpn*, vol. 60, p. 3980–3981.

[35] Y. Yamamura, "Heat capacity and phase transition of fexnbs2 at low temperature," *J. Alloys Compd*, vol. 383, p. 338–341.

[36] T. Tsuji, Y. Yamamura, H. Watanabe, K. Saito, and M. Sorai, "Heat capacity of intercalated layered materials fexnbs2 at low temperature," *J. Therm. Anal. Calorim*, vol. 57, p. 839–846.

[37] S. Parkin and R. Friend, "3d transition-metal intercalates of the niobium and tantalum dichalcogenides," *II. Transport properties. Phil. Mag. B*, vol. 41, p. 95–112.

[38] A. Little, "Three-state nematicity in the triangular lattice antiferromagnet fe 1/3nbs2," *Nat. Mater*, vol. 19, p. 1062–1067.

[39] J. Nogués and I. Schuller, "Exchange bias," *J. Magn. Magn. Mater*, vol. 192, p. 203–232.

[40] N. Büttgen, P. Kuhns, A. Prokofiev, A. Reyes, and L. Svistov, "High-field nmr of the quasi-one-dimensional antiferromagnet licuvo 4," *Phys. Rev. B*, vol. 85, p. 214421.

[41] A. Malozemoff, "Random-field model of exchange anisotropy at rough ferromagnetic-antiferromagnetic interfaces," *Phys. Rev. B*, vol. 35, p. 3679–3682.

[42] P. Wong, "Coexistence of spin-glass and antiferromagnetic orders in the ising system fe 0.55mg0.45cl2," *Phys. Rev. Lett*, vol. 55, p. 2043–2046.

[43] S. Chillal, "Microscopic coexistence of antiferromagnetic and spin-glass states," *Phys. Rev. B*, vol. 87, p. 220403.

[44] W. Kleemann, V. Shvartsman, P. Borisov, and A. Kania, "Coexistence of antiferro-magnetic and spin cluster glass order in the magnetoelectric relaxor multiferroic pbfe 0.5nb0.5o3," *Phys. Rev. Lett*, vol. 105, p. 257202.

[45] Z. Fu, "Coexistence of magnetic order and spin-glass-like phase in the pyrochlore an-tiferromagnet na 3co(co3) 2cl," *Phys. Rev. B*, vol. 87, p. 214406.

[46] in *Spin Glasses and Random Fields (Directions in Condensed Matter Physics* (A. Young, ed.), vol. 12, World Scientific.

[47] S. Fishman and A. Aharony, "Random field effects in disordered anisotropic antiferro-magnets," *J. Phys. C*, vol. 12, L729.

[48] J. Cardy, "Random-field effects in site-disordered ising antiferromagnets," *Phys. Rev. B*, vol. 29, p. 505–507.

[49] A. Malozemoff, "Mechanisms of exchange anisotropy," *J. Appl. Phys*, vol. 63, p. 3874–3879.

[50] H. Narita, H. Ikuta, H. Hinode, T. Uchida, T. Ohtani, and M. Wakihara, "Preparation and Physical Properties of Fe_xTaS_2 $(0.15 \leq x \leq 0.50)$ Compounds," *Journal of Solid State Chemistry*, vol. 108, no. 1, pp. 148–151, 1994.

[51] R. Chamberlin, G. Mozurkewich, and R. Orbach, "Time decay of the remanent mag-netization in spin-glasses," *Physical review letters*, vol. 52, no. 10, p. 867, 1984.

[52] G. DeFotis and K. Dell, "Thermoremanent-magnetization relaxation in the insulating spin glass $Co_{1-x}MnxCl_2 \cdot 2H_2O$," *Physical Review B*, vol. 50, no. 14, p. 9937, 1994.

[53] P. Nordblad, P. Svedlindh, L. Lundgren, and L. Sandlund, "Time decay of the remanent magnetization in a $CuMn$ spin glass," *Physical Review B*, vol. 33, no. 1, p. 645, 1986.

[54] E. Vincent, "Ageing, rejuvenation and memory: the example of spin-glasses," in *Ageing and the glass transition*, pp. 7–60, Springer, 2007.

[55] A. H. Morrish, "The Physical Principles of Magnetism, John Wiley& Sons," *New York*, 1965.

[56] B. Cullity, "Introduction to Magnetic Materials, Addison," 1972.

[57] L. Klein, "Comment on "Exchange bias-like phenomenon in $SrRuO_3$" [Appl. Phys. Lett. 88, 102502 (2006)]," *Applied physics letters*, vol. 89, no. 3, p. 102502, 2006.

[58] L. Pi, S. Zhang, S. Tan, and Y. Zhang, "Exchange bias-like phenomenon in $SrRuO_3$," *Applied physics letters*, vol. 88, no. 10, p. 102502, 2006.

[59] J. Geshev, "Comment on:"exchange bias and vertical shift in cofe2o4 nanoparticles"[j. magn. magn. mater. 313 (2007) 266]," *Journal of Magnetism and Magnetic Materials*, vol. 320, no. 3-4, pp. 600–602, 2008.

[60] J. Geshev, "Comment on 'Particle size dependent exchange bias and cluster-glass states in $LaMn_{0.7}Fe_{0.3}O_3$'," *Journal of Physics: Condensed Matter*, vol. 21, no. 7, p. 078001, 2009.

[61] W. H. Meiklejohn and C. P. Bean, "New magnetic anisotropy," *Physical review*, vol. 102, no. 5, p. 1413, 1956.

[62] "new magnetic anisotropy,"

[63] W. Meiklejohn, "Exchange anisotropy—a review," *Journal of Applied Physics*, vol. 33, no. 3, pp. 1328–1335, 1962.

[64] A. Berkowitz and K. Takano, "Exchange anisotropy—a review," *Journal of Magnetism and Magnetic materials*, vol. 200, no. 1-3, pp. 552–570, 1999.

[65] S. Mankovsky, S. Polesya, H. Ebert, and W. Bensch, "Electronic and magnetic properties of 2 h- nbs 2 intercalated by 3 d transition metals," *Physical Review B*, vol. 94, no. 18, p. 184430, 2016.

[66] A. K. Nayak, M. Nicklas, S. Chadov, P. Khuntia, C. Shekhar, A. Kalache, M. Baenitz, Y. Skourski, V. K. Guduru, A. Puri, *et al.*, "Design of compensated ferrimagnetic Heusler alloys for giant tunable exchange bias," *Nature materials*, vol. 14, no. 7, p. 679, 2015.

[67] M. Hudl, R. Mathieu, and P. Nordblad, "Tunable exchange bias in dilute magnetic alloys – chiral spin glasses," *Scientific Reports*, vol. 6, p. 19964, apr 2016.

[68] N. L. Nair, E. Maniv, C. John, S. Doyle, J. Orenstein, and J. G. Analytis, "Electrical switching in a magnetically intercalated transition metal dichalcogenide," *Nature Materials*, vol. 19, pp. 153–157, Feb. 2020.

[69] J. Železný, H. Gao, K. Výborný, J. Zemen, J. Mašek, A. Manchon, J. Wunderlich, J. Sinova, and T. Jungwirth, "Relativistic N\'eel-Order Fields Induced by Electrical Current in Antiferromagnets," *Physical Review Letters*, vol. 113, p. 157201, Oct. 2014.

[70] P. Wadley, B. Howells, J. Železný, C. Andrews, V. Hills, R. P. Campion, V. Novák, K. Olejník, F. Maccherozzi, S. S. Dhesi, S. Y. Martin, T. Wagner, J. Wunderlich, F. Freimuth, Y. Mokrousov, J. Kuneš, J. S. Chauhan, M. J. Grzybowski, A. W. Rushforth, K. W. Edmonds, B. L. Gallagher, and T. Jungwirth, "Electrical switching of an antiferromagnet," *Science*, vol. 351, pp. 587–590, Feb. 2016.

[71] S. Bodnar, L. Šmejkal, I. Turek, T. Jungwirth, O. Gomonay, J. Sinova, A. Sapozhnik, H.-J. Elmers, M. Kläui, and M. Jourdan, "Writing and reading antiferromagnetic mn2au by néel spin-orbit torques and large anisotropic magnetoresistance," *Nature Communications*, 2018.

[72] E. Maniv, N. L. Nair, S. C. Haley, S. Doyle, C. John, S. Cabrini, A. Maniv, S. K. Ramakrishna, Y.-L. Tang, P. Ercius, R. Ramesh, Y. Tserkovnyak, A. P. Reyes, and J. G. Analytis, "Antiferromagnetic switching driven by the collective dynamics of a coexisting spin glass," *Science Advances*, vol. 7, Jan. 2021.

[73] D. C. Johnston, "Influence of uniaxial single-ion anisotropy on the magnetic and thermal properties of heisenberg antiferromagnets within unified molecular field theory," *Phys. Rev. B*, vol. 95, p. 094421, Mar 2017.

[74] O. Gorochov, A. L. Blanc-soreau, J. Rouxel, P. Imbert, and G. Jehanno, "Transport properties, magnetic susceptibility and mössbauer spectroscopy of fe0.25nbs2 and fe0.33nbs2," *Philosophical Magazine B*, vol. 43, no. 4, pp. 621–634, 1981.

[75] F. Hulliger and E. Pobitschka, "On the magnetic behavior of new 2hnbs2-type derivatives," *Journal of Solid State Chemistry*, vol. 1, no. 2, pp. 117 – 119, 1970.

[76] B. V. Laar, H. Rietveld, and D. Ijdo, "Magnetic and crystallographic structures of mexnbs2 and mextas2," *Journal of Solid State Chemistry*, vol. 3, no. 2, pp. 154 – 160, 1971.

[77] K. Anzenhofer, J. Van Den Berg, P. Cossee, and J. Helle, "The crystal structure and magnetic susceptibilities of mnnb3s6, fenb3s6, conb3s6 and ninb3s6," *Journal of Physics and Chemistry of Solids*, vol. 31, no. 5, pp. 1057–1067, 1970.

[78] N. Doi and Y. Tazuke, "Spin glass phases in 2h-fexnbs2," *Journal of the Physical Society of Japan*, vol. 60, no. 11, pp. 3980–3981, 1991.

[79] R. H. Friend, A. R. Beal, and A. D. Yoffe, "Electrical and magnetic properties of some first row transition metal intercalates of niobium disulphide," *The Philosophical Magazine: A Journal of Theoretical Experimental and Applied Physics*, vol. 35, no. 5, pp. 1269–1287, 1977.

[80] P. Sengupta, C. D. Batista, R. D. McDonald, S. Cox, J. Singleton, L. Huang, T. P. Papageorgiou, O. Ignatchik, T. Herrmannsdörfer, J. L. Manson, J. A. Schlueter, K. A. Funk, and J. Wosnitza, "Nonmonotonic field dependence of the N\'eel temperature in the quasi-two-dimensional magnet $[\text{Cu}({\text{HF}}_{2})}{(\text{pyz})}_{2}]{\text{BF}}_{4}$," *Physical Review B*, vol. 79, p. 060409, Feb. 2009.

[81] T. Ono, H. Tanaka, H. Aruga Katori, F. Ishikawa, H. Mitamura, and T. Goto, "Magnetization plateau in the frustrated quantum spin system cs_2cubr_4," *Phys. Rev. B*, vol. 67, p. 104431, Mar 2003.

[82] M. Ye and A. V. Chubukov, "Half-magnetization plateau in a heisenberg antiferromagnet on a triangular lattice," *Physical Review B*, vol. 96, no. 14, p. 140406, 2017.

[83] M. Ye and A. V. Chubukov, "Quantum phase transitions in the heisenberg $J_1 - J_2$ triangular antiferromagnet in a magnetic field," *Phys. Rev. B*, vol. 95, p. 014425, Jan 2017.

[84] L. Seabra and N. Shannon, "Competition between supersolid phases and magnetization plateaus in the frustrated easy-axis antiferromagnet on a triangular lattice," *Physical Review B*, vol. 83, no. 13, p. 134412, 2011.

[85] A. Wiedenmann, L. Regnault, P. Burlet, J. Rossat-Mignod, O. Koundé, and D. Billerey, "A neutron scattering investigation of the magnetic phase diagram of fei2," *Journal of Magnetism and Magnetic Materials*, vol. 74, no. 1, pp. 7 – 21, 1988.

[86] A. I. Coldea, L. Seabra, A. McCollam, A. Carrington, L. Malone, A. F. Bangura, D. Vignolles, P. G. van Rhee, R. D. McDonald, T. Sörgel, M. Jansen, N. Shannon, and R. Coldea, "Cascade of field-induced magnetic transitions in a frustrated antiferromagnetic metal," *Physical Review B*, vol. 90, p. 020401, July 2014.

[87] J. P. Perdew, K. Burke, and M. Ernzerhof, "Generalized gradient approximation made simple," *Physical Review Letters*, vol. 77, p. 3865, 10 1996.

[88] J. P. Perdew and W. Yue, "Accurate and simple density functional for the electronic exchange energy: Generalized gradient approximation," *Physical Review B*, vol. 33, no. 12, pp. 8800–8802, 1986.

[89] I. Yang, S. Y. Savrasov, and G. Kotliar, "Importance of correlation effects on magnetic anisotropy in Fe and Ni," *Physical Review Letters*, vol. 87, no. 21, pp. 216405–1–216405–4, 2001.

[90] E. Bousquet and N. Spaldin, "J dependence in the LSDA+U treatment of noncollinear magnets," *Physical Review B - Condensed Matter and Materials Physics*, vol. 82, no. 22, pp. 1–4, 2010.

[91] C. Lee, J. Hong, W. J. Son, E. Kan, J. H. Shim, and M. H. Whangbo, "Magnetic structure of (C5H12N)CuBr3: Origin of the uniform Heisenberg chain behavior and the magnetic anisotropy of the Cu2+ (S = 1/2) ions," *RSC Advances*, vol. 6, no. 27, pp. 22722–22727, 2016.

[92] C. Loschen, J. Carrasco, K. M. Neyman, and F. Illas, "First-principles LDA+U and GGA+U study of cerium oxides: Dependence on the effective U parameter," *Physical Review B - Condensed Matter and Materials Physics*, vol. 75, no. 3, pp. 1–8, 2007.

[93] R. L. Martin and F. Illas, "Antiferromagnetic exchange interactions from hybrid density functional theory," *Physical Review Letters*, vol. 79, no. 8, pp. 1539–1542, 1997.

[94] T. Linneweber, J. Bünemann, U. Löw, F. Gebhard, and F. Anders, "Exchange couplings for Mn ions in CdTe: Validity of spin models for dilute magnetic II-VI semiconductors," *Physical Review B*, vol. 95, no. 4, pp. 1–10, 2017.

[95] M. Singh, J. Callaway, and C. Wang, "Calculation of g and g for iron and nickel," *Physical Review B*, vol. 14, no. 3, p. 1214, 1976.

[96] S. Mankovsky, S. Polesya, H. Ebert, and W. Bensch, "Electronic and magnetic properties of $2H\ensuremath{-}{\mathrm{NbS}}_{2}$ intercalated by $3d$ transition metals," *Physical Review B*, vol. 94, p. 184430, Nov. 2016.

[97] T. Jungwirth, J. Sinova, A. Manchon, X. Marti, J. Wunderlich, and C. Felser, "The multiple directions of antiferromagnetic spintronics," *Nature Physics*, vol. 14, pp. 200–203, Mar. 2018. Number: 3 Publisher: Nature Publishing Group.

[98] S. Wu, Z. Xu, S. C. Haley, S. F. Weber, A. Acharya, E. Maniv, Y. Qiu, A. A. Aczel, J. B. Neaton, J. G. Analytis, and R. J. Birgeneau, "Highly tunable magnetic phases in transition metal dichalcogenide $fe_{1/3+\delta}nbs_2$," *Physical Review X*, 2021.

[99] H. Ochoa, R. Zarzuela, and Y. Tserkovnyak, "Spin hydrodynamics in amorphous magnets," *Phys. Rev. B*, vol. 98, p. 054424, Aug 2018.

[100] A. Little, C. Lee, C. John, S. Doyle, E. Maniv, N. L. Nair, W. Chen, D. Rees, J. W. Venderbos, R. M. Fernandes, *et al.*, "Three-state nematicity in the triangular lattice antiferromagnet fe 1/3 nbs 2," *Nature materials*, vol. 19, no. 10, pp. 1062–1067, 2020.

[101] R. Lebrun, A. Ross, O. Gomonay, V. Baltz, U. Ebels, A.-L. Barra, A. Qaiumzadeh, A. Brataas, J. Sinova, and M. Kläui, "Long-distance spin-transport across the Morin phase transition up to room temperature in ultra-low damping single crystals of the antiferromagnet -Fe 2 O 3," *Nature Communications*, vol. 11, p. 6332, Dec. 2020.

[102] J. Han, P. Zhang, Z. Bi, Y. Fan, T. S. Safi, J. Xiang, J. Finley, L. Fu, R. Cheng, and L. Liu, "Birefringence-like spin transport via linearly polarized antiferromagnetic magnons," *Nature Nanotechnology*, vol. 15, p. 563–568, 2020.

[103] W. Yuan, Q. Zhu, T. Su, Y. Yao, W. Xing, Y. Chen, Y. Ma, X. Lin, J. Shi, R. Shindou, X. Xie, and W. Han, "Experimental signatures of spin superfluid ground state in canted antiferromagnet cr2o3 via nonlocal spin transport," *Science Advances*, vol. 4, no. 4, 2018.

[104] R. Lebrun, A. Ross, S. Bender, A. Qaiumzadeh, L. Baldrati, J. Cramer, A. Brataas, R. Duine, and M. Klaui, "Tunable long-distance spin transport in a crystalline antiferromagnetic iron oxide," *Nature*, vol. 561, pp. 222–225, 2018.

[105] S. C. Haley, S. F. Weber, T. Cookmeyer, D. E. Parker, E. Maniv, N. Maksimovic, C. John, S. Doyle, A. Maniv, S. K. Ramakrishna, A. P. Reyes, J. Singleton, J. E. Moore, J. B. Neaton, and J. G. Analytis, "Half-magnetization plateau and the origin of threefold symmetry breaking in an electrically switchable triangular antiferromagnet," *Phys. Rev. Research*, vol. 2, p. 043020, Oct 2020.

[106] E. Maniv, R. A. Murphy, S. C. Haley, S. Doyle, C. John, A. Maniv, S. K. Ramakrishna, Y.-L. Tang, P. Ercius, R. Ramesh, A. P. Reyes, J. R. Long, and J. G. Analytis, "Exchange bias due to coupling between coexisting antiferromagnetic and spin-glass orders," *Nature Physics*, pp. 1–6, Jan. 2021.

[107] A. Little, C. Lee, C. John, S. Doyle, E. Maniv, N. L. Nair, W. Chen, D. Rees, J. W. Venderbos, R. M. Fernandes, *et al.*, "Three-state nematicity in the triangular lattice antiferromagnet $Fe_{1/3}NbS_2$," *Nature Materials*, pp. 1–6, 2020.

[108] H. Gomonay and V. M. Loktev, "Magnetostriction and magnetoelastic domains in antiferromagnets," *Journal of Physics: Condensed Matter*, vol. 14, no. 15, p. 3959, 2002.

[109] E. Gomonay and V. Loktev, "Magnetostriction and domain structure in antiferromagnets," *Journal of magnetism and magnetic materials*, vol. 242, pp. 1418–1420, 2002.

[110] H. V. Gomonay and V. M. Loktev, "Shape-induced phenomena in finite-size antiferromagnets," *Phys. Rev. B*, vol. 75, p. 174439, May 2007.

[111] J. Eshelby, "The continuum theory of lattice defects," *Solid state physics*, vol. 3, pp. 79–144, 1956.

[112] C. Kittel and J. Galt, "Ferromagnetic domain theory," *Solid state physics*, vol. 3, pp. 437–564, 1956.

[113] V. Kalita and A. Lozenko, "On the magnetoelastic nature of the anisotropic domains in easy-plane crystals of iron-group dihalides," *Low Temperature Physics*, vol. 27, no. 5, pp. 358–361, 2001.

[114] V. Kalita, A. Lozenko, S. Ryabchenko, and P. Trotsenko, "Magnetoelasticity and domain structure in antiferromagnetic crystals of the iron-group dihalides," *Low temperature physics*, vol. 31, no. 8, pp. 794–806, 2005.

[115] V. Kalita and A. Lozenko, "Magnetostriction during field transformation of the domain structure of an easy-plane antiferromagnet in the case of a magnetoelastic mechanism for the multidomain state," *Low Temperature Physics*, vol. 27, no. 8, pp. 645–649, 2001.

[116] Y.-Y. Li, "Domain walls in antiferromagnets and the weak ferromagnetism of α-fe$_2$o$_3$," *Phys. Rev.*, vol. 101, pp. 1450–1454, Mar 1956.

[117] S. A. Siddiqui, J. Sklenar, K. Kang, M. J. Gilbert, A. Schleife, N. Mason, and A. Hoffman, "Metallic antiferromagnets," *Journal of Applied Physics*, vol. 128, p. 040904, 2020.

[118] R. Acharyya, H. Y. T. Nguyen, W. P. Pratt, and J. Bass, "A study of spin–flipping in sputtered IrMn using Py-based exchange-biased spin-valves," *Journal of Applied Physics*, vol. 109, p. 07C503, Apr. 2011. Publisher: American Institute of Physics.

[119] P. Merodio, A. Ghosh, C. Lemonias, E. Gautier, U. Ebels, M. Chshiev, H. Béa, V. Baltz, and W. E. Bailey, "Penetration depth and absorption mechanisms of spin currents in Ir20Mn80 and Fe50Mn50 polycrystalline films by ferromagnetic resonance and spin pumping," *Applied Physics Letters*, vol. 104, p. 032406, Jan. 2014. Publisher: American Institute of Physics.

[120] M. Arana, M. Gamino, E. F. Silva, V. M. T. S. Barthem, D. Givord, A. Azevedo, and S. M. Rezende, "Spin to charge current conversion by the inverse spin Hall effect in the metallic antiferromagnet $\mathrm{M}{\mathrm{n}}_{2}\mathrm{Au}$ at room temperature," *Physical Review B*, vol. 98, p. 144431, Oct. 2018. Publisher: American Physical Society.

[121] W. Zhang, M. B. Jungfleisch, W. Jiang, J. E. Pearson, A. Hoffmann, F. Freimuth, and Y. Mokrousov, "Spin Hall Effects in Metallic Antiferromagnets," *Physical Review Letters*, vol. 113, p. 196602, Nov. 2014. Publisher: American Physical Society.

[122] V. Baltz, A. Manchon, M. Tsoi, T. Moriyama, T. Ono, and Y. Tserkovnyak, "Antiferromagnetic spintronics," *Rev. Mod. Phys.*, vol. 90, p. 015005, Feb 2018.

[123] P. Wadley, B. Howells, J. Železný, C. Andrews, V. Hills, R. P. Campion, V. Novák, K. Olejník, F. Maccherozzi, S. S. Dhesi, S. Y. Martin, T. Wagner, J. Wunderlich,

F. Freimuth, Y. Mokrousov, J. Kuneš, J. S. Chauhan, M. J. Grzybowski, A. W. Rush-forth, K. W. Edmonds, B. L. Gallagher, and T. Jungwirth, "Electrical switching of an antiferromagnet," *Science*, vol. 351, no. 6273, pp. 587–590, 2016.

[124] J. Železný, H. Gao, K. Výborný, J. Zemen, J. Mašek, A. Manchon, J. Wunderlich, J. Sinova, and T. Jungwirth, "Relativistic néel-order fields induced by electrical current in antiferromagnets," *Physical Review Letters*, 2014.

[125] B. Toby and R. Von Dreele, "GSAS-II: the genesis of a modern open-source all purpose crystallography software package," *Journal of Applied Crystallography*, vol. 46, no. 2, pp. 544–549, 2013.

[126] S. F. Weber and J. B. Neaton, "Origins of anisotropic transport in the electrically switchable antiferromagnet $fe_{1/3}nbs_2$," *Phys. Rev. B*, vol. 103, p. 214439, Jun 2021.

[127] G. Tenasini, E. Martino, N. Ubrig, N. J. Ghimire, H. Berger, O. Zaharko, F. Wu, J. F. Mitchell, I. Martin, L. Forró, and A. F. Morpurgo, "Giant anomalous hall effect in quasi-two-dimensional layered antiferromagnet $co_{1/3}nbs_2$," *Phys. Rev. Research*, vol. 2, p. 023051, Apr 2020.

[128] S. S. P. Parkin, E. A. Marseglia, and P. J. Brown, "Magnetic structure of co1/3nbs2 and co1/3tas2," *Journal of Physics C: Solid State Physics*, vol. 16, p. 2765, may 1983.

[129] S. Mangelsen, P. Zimmer, C. Näther, S. Mankovsky, S. Polesya, H. Ebert, and W. Bensch, "Interplay of sample composition and anomalous hall effect in co_xNbs_2," *Phys. Rev. B*, vol. 103, p. 184408, May 2021.

[130] S. Hellmann, M. Beye, C. Sohrt, T. Rohwer, F. Sorgenfrei, H. Redlin, M. Kalläne, M. Marczynski-Bühlow, F. Hennies, M. Bauer, *et al.*, "Ultrafast melting of a charge-density wave in the mott insulator $1t\text{-}tas_2$," *Physical Review Letters*, vol. 105, no. 18, p. 187401, 2010.

[131] L. Stojchevska, I. Vaskivskyi, T. Mertelj, P. Kusar, D. Svetin, S. Brazovskii, and D. Mihailovic, "Ultrafast switching to a stable hidden quantum state in an electronic crystal," *Science*, vol. 344, no. 6180, pp. 177–180, 2014.

[132] M. Yoshida, Y. Zhang, J. Ye, R. Suzuki, Y. Imai, S. Kimura, A. Fujiwara, and Y. Iwasa, "Controlling charge-density-wave states in nano-thick crystals of $1t\text{-}tas_2$," *Scientific reports*, vol. 4, no. 1, pp. 1–5, 2014.

[133] M. Yoshida, R. Suzuki, Y. Zhang, M. Nakano, and Y. Iwasa, "Memristive phase switching in two-dimensional $1t\text{-}tas_2$ crystals," *Science advances*, vol. 1, no. 9, p. e1500606, 2015.

[134] Y. Yu, F. Yang, X. F. Lu, Y. J. Yan, Y.-H. Cho, L. Ma, X. Niu, S. Kim, Y.-W. Son, D. Feng, *et al.*, "Gate-tunable phase transitions in thin flakes of 1t-tas$_2$," *Nature nanotechnology*, vol. 10, no. 3, pp. 270–276, 2015.

[135] I. Vaskivskyi, I. Mihailovic, S. Brazovskii, J. Gospodaric, T. Mertelj, D. Svetin, P. Sutar, and D. Mihailovic, "Fast electronic resistance switching involving hidden charge density wave states," *Nature communications*, vol. 7, no. 1, pp. 1–6, 2016.

[136] D. Svetin, I. Vaskivskyi, S. Brazovskii, and D. Mihailovic, "Three-dimensional resistivity and switching between correlated electronic states in 1t-tas$_2$," *Scientific reports*, vol. 7, no. 1, pp. 1–10, 2017.

[137] W. Wang, D. Dietzel, and A. Schirmeisen, "Lattice Discontinuities of 1T-TaS2 across First Order Charge Density Wave Phase Transitions," *Scientific Reports*, vol. 9, p. 7066, May 2019. Number: 1 Publisher: Nature Publishing Group.